Dissertation

Adhesive Strength Evaluation Method Focusing on the Intensity of Singular Stress Field to Minimize Bend Effect for Single Lap Joint

Rong LI /14595102

Kyushu Institute of Technology

2017

Dissertation

Adhesive Strength Evaluation Method Focusing on the Intensity of Singular Stress Field to Minimize Bend Effect for Single Lap Joint

By

Rong LI

(Student Number:14595102)

Supervisor: Prof. Nao-Aki NODA

Department of Mechanical Engineering

Kyushu Institute of Technology

2017

Abstract

Adhesively bonded joints are economical, practical and easy to make; thus they have been widely used in a variety of industries. The testing method for the adhesive strength of lap joint is standardized by Japanese Industrial Standards (JIS). However, the debonding strength is affected by the specimen dimension and difficult to be applied to other geometries. Compared with double lap joint, single lap joint can be used conveniently. However, the experimental results show that the strength of double lap joint is nearly twice larger than the one of single lap joint. Therefore, it is necessary to find a suitable evaluation method for lap joint testing. The single lap joint testing should be done under pure shear loading, but pure shear testing is difficult to be realized in the experiment. Due to the bend deformation of single lap joint during testing, the peeling force is applied to the adhesive region. Then the intensity of singular stress field (ISSF) at the interface corner is affected by the peeling force due to the deformation. This research concentrated on the adhesive strength evaluation method to minimize the ISSF for single lap joint. This thesis is composed of total 7 chapters and organized as follows.

Chapter 1 gives the introduction of the applications of adhesive bonded structures in numerous industrial sectors, such as integrated circuit (IC) technology, automobile industry and aircraft industry. The application and importance of adhesively bonded structure were investigated. Then the research purpose of this thesis is introduced, focusing on the evaluation method to minimize the ISSF for single lap joint. In order to clarify this research clearly, the studies of the research on the singularity in the adhesively bonded joints are reviewed in chapter 2. It is found that there are no results about the convenient evaluation method to minimize the ISSF for single lap joint.

Since the ISSF of butt joint can be obtained conveniently by using the analysis method presented in previous studies, the debonding strength of butt joint is investigated in chapter 3. First, a homogeneous and flawless elastic adhesive layer is assumed to evaluate the butt joint strength for carbon steel/epoxy resin, aluminum/araldite, and brass/solder. It is found that the adhesive strength is always expressed as the critical ISSF. Next, a small fictitious interface edge crack is assumed at the adhesive layer to consider the singular stress field including crack. Then the debonding strength is also found to be controlled by the critical ISSF of the fictitious crack. A suitable dimension of the fictitious crack is discussed to predict the strength for adhesive joints accurately and conveniently.

In chapter 4, a convenient analysis method for the ISSF of lap joint is proposed. Since the singular stress field of lap joint is complex than butt joint, the method in chapter 3 cannot be applied to the lap joint analysis directly. The same FEM mesh pattern is applied to unknown problems and reference problems. Then, it is found that the ISSF is obtained accurately by focusing on the FEM stress at the adhesive corner. Although the singular stress is controlled by two factors for lap joints, it can be expressed almost in the same way as butt joint even if the adhesive geometries are widely changed. Therefore, the ISSF of lap joints as well as butt joints can be obtained conveniently by using the analysis method presented in this chapter. The usefulness of the present solution is verified by comparing with the results of the conventional method.

In chapter 5, the debonding criterion of single lap joint is investigated in terms of the critical ISSF $K_{\sigma c}$ by using the analysis method presented in chapter 4. In this chapter, the value of $K_{\sigma c}$ is investigated based on the experimental results. The results

show that the adhesive strength can be evaluated as $K_{\sigma c}$=const when the debonding fracture occurs (except for the specimen with very short adhesive length).

Chapter 6 shows the adhesive strength evaluation method to minimize bend effect for single lap joint. Here, the evaluation method is investigated in terms of the ISSF appearing at the interface corner. The results show that the ISSF decreases with increasing the adherend thickness. The minimum ISSF can be obtained when the adherend thickness t_1 is large enough, and the deformation angle at the interface corner is smallest when adherend thickness t_1 is large enough. In addition, the equivalent conditions of strength for single lap joint and double lap joint are investigated in terms of the ISSF. It is found that the strength of single lap joint with t_1=7mm is nearly equal to that of double lap joint with t_1=1.5mm (JIS) since the ISSFs of single lap joint and double lap joint are nearly the same. For the same reason, the strength of single lap joint is nearly equal to that of double lap joint when $t_1 \geq 25$mm.

In the last chapter of this thesis, chapter 7, main conclusions of this study are summarized.

Table of Contents

List of Figures

List of Tables

Nomenclature

FEM	finite element method
ISSF	intensity of singular stress field
RWCIM	reciprocal work contour integral method
SIF	stress intensity factor
a	length of the edge interface crack of butt joint
C_I, C_{II}	constants for mode I, mode II defined as $C_I = F_I\left(\frac{a}{W}\right)^{1-\lambda}, C_{II} = F_{II}\left(\frac{a}{W}\right)^{1-\lambda}$
C_σ, C_τ	constants defined as $C_\sigma = K_{\sigma,\lambda_2}/K_{\sigma,\lambda_1}$, $C_\tau = K_{\tau,\lambda_2}/K_{\tau,\lambda_1}$ for lap joint
E	Young's modulus
F_σ	dimensionless corner SIF
F_I, F_{II}	dimensionless interface SIFs for mode I, mode II
F_{I,λ_1}	dimensionless notch SIF for mode I
G	shear modulus
h	adhesive thickness of butt joint
K_σ	corner SIF of butt joint
$K_{\sigma,\lambda_1}, K_{\sigma,\lambda_2}$	ISSF of lap joint
$K_{\sigma c}$	critical value of corner SIF of butt joint / critical value of ISSF of lap joint
K_I, K_{II}	interface SIFs for mode I, mode II
K_{IC}	critical value of SIF for mode I
K_{I,λ_1}	notch SIF for mode I

K_{IC,λ_1} critical value of notch SIF for mode I

L fixed boundary length of lap joint

l_1 adherend length of lap joint

l_2 adherend length of lap joint $l_2 = l_1 - l_{ad} - d$

l_{ad} adhesive length of lap joint

M bending moment applied

T, S tensile and shear stresses applied to the reference problem

W width of the bonded strip of butt joint/ plate width of lap joint

P_{af} experimental fracture load of the adhesive joints

r radial distance away from the singular point/crack tip

t depth of notch of butt joint

t_1 adherend thickness of lap joint

t_{ad} adhesive thickness of lap joint

$f_{ij}(\theta)$ angle functions expressing singular stress field

α , β Dundurs' material composite parameters

γ notch opening angle (degrees)

ε bi-elastic constant

θ angle from the interface corner

θ_{ol}, θ_{or} deformation angles at the interface corner O of single lap joint

θ_C deformation angle at the interface corner C of single lap joint

λ singular index

σ_c	adhesive tensile strength
σ_y, τ_{xy}	tension and shear stress component near the crack tip
$\sigma_y^{\infty}, \tau_{xy}^{\infty}$	tension and shear stress at infinity
$\sigma_{yo}^{FEM*}, \tau_{xyo}^{FEM*}$	finite element stresses at the crack tip of the reference problem
$\sigma_{yo}^{FEM}, \tau_{xyo}^{FEM}$	finite element stresses at the crack tip of the given unknown problem
ν	Poisson's ratio

Chapter 1 Introduction

1.1 Research background

Adhesively bonded joints are economical, practical and easy to make; thus they have been widely used in a variety of industries. Recent years, due to the remarkable influences on the lightweight of vehicle, adhesively bonded joint in structural components is widely adopted in automobile industry[1-3]. And the application in automobile industry leads to the benefits in reduced emissions, fuel economy and driving safety [1]. Fig.1.1 shows the schematic of the adhesively bonded steel sheets at the automobile door [2].

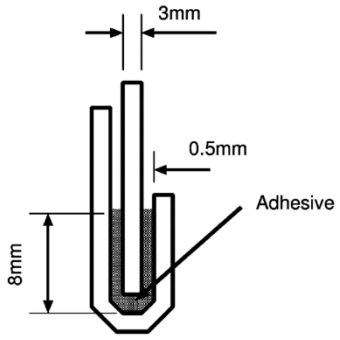

Fig.1.1 The adhesively bonded steel sheets at the automobile door

Adhesively bonded joint also played an important role in the aircraft and aerospace industry[4,5]. The main reason for the success of adhesive bonding is they offer a low-weight, fatigue-resistant, and aerodynamically sound method of assembly. In addition, due to the excellent ratio of strength and weight for adhesive and the use of polymeric composites and lightweight metals, the application of adhesive bonded technology provides extremely lightweight designs. In the aircraft and aerospace industry, structural adhesively bonded joints are always used for wing skins, attaching stringers to fuselage. Fig 1.2 shows the mainly adhesive bonded structures used in the

modern aircraft (Courtesy Boeing Company) [4]. In this figure, the black part means the bonded area in aircraft.

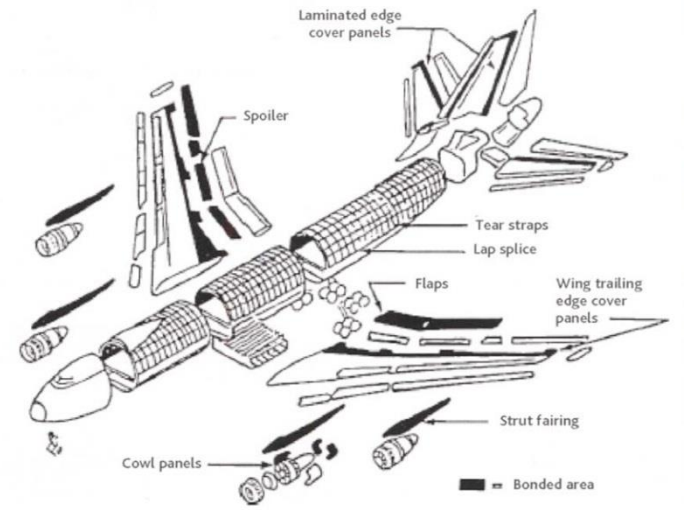

Fig.1.2 Bonded areas on modern aircraft.

However, it has been reported that the singular stress field usually exists at the interface corner [6], and it is the reason why fatigue cracks are normally observed from the edge corner. For example, for the integrated circuit (IC) package [7-11] as shown in Fig.1.3, when a plastic IC package is in the thermal environment or subjected to mechanical loading, the interfacial debonding often occurs [7-10]. The acoustic image of the debonding beneath the silicon chip obtained under the PVDC-contact is shown in Fig.1.4 [11]. The fractures of adhesive joints are characterized mainly by the critical intensity of singular stress field (ISSF) with the order of stress singularity. However, the singular stress field for dissimilar materials bonded interface varies depending on the geometry and material combinations. Take the IC package in Fig. 1.3 as an example, although the material combinations at points A-E are the same, the singular fields at points A-E are different, therefore the critical ISSFs are different. Thus, the debonding evaluation has become more and more an important issue in the design of adhesive structures.

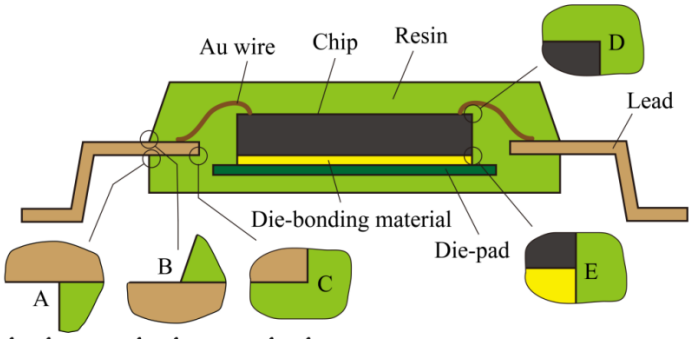

Fig.1.3 An example of IC package

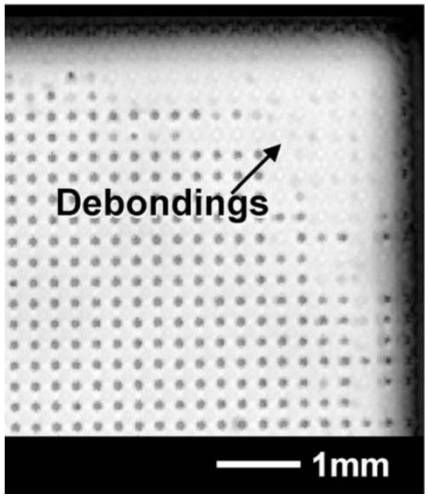

Fig.1.4 Acoustic image of the debonding beneath the silicon chip obtained under the PVDC-contact.

Among adhesively bonded joints, single lap joint is the most commonly used and studied by the researchers due to its simplicity. And single lap joint is the most representative configuration of adhesive joints used in the industries. There are many testing methods and standards for evaluating lap joint strengths [12-14]. Fig.1.5 shows the dimensions of the single lap joint specimen in [12]. However, it is found that the debonding strength is affected by the specimen dimension and difficult to be applied to other geometries. Compared with double lap joint, single lap joint can be used conveniently. However, the experimental results [15] show that the adhesive strength of double lap joint is nearly twice larger than the one of single lap joint. Therefore, it is

necessary to find a suitable evaluation method for single lap joint testing. The single lap joint testing should be done under pure shear loading, but pure shear testing is difficult to be realized in the experiment. Due to the bend deformation of single lap joint during testing, the peeling force is applied to the adhesive region. Then the ISSF at the interface corner is affected by the peeling force due to the deformation. Therefore, it is necessary to find a suitable evaluation method to minimize the bend effect for single lap joint.

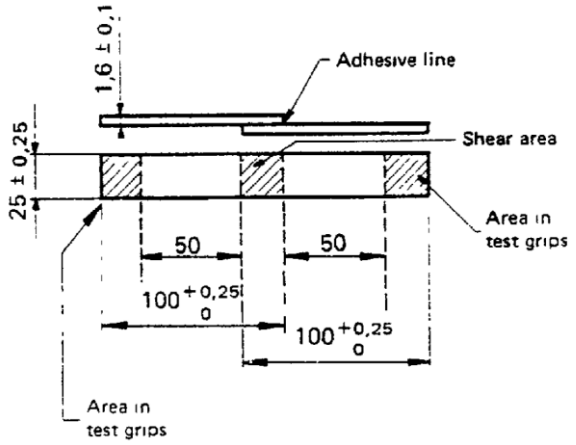

Fig.1.5 Dimensions of single lap joint specimen in british standard

1.2 Research purposes

Debonding strength of adhesively bonded joint has been subject of intensive research for many years and several concepts have been developed in an attempt to evaluate the strength of adhesive joint. However, it is found that there are still no results about the convenient evaluation method to minimize the bend effect for single lap joint. Therefore, in this study, the evaluation method to minimize the bend effect will be investigated in terms of ISSF.

Due to the mathematical difficulties, few analytical methods are available for interfacial debonding, and a more practical and rational method is required. Since the

ISSF of butt joint can be obtained conveniently by using the analysis method presented in previous studies, the debonding strength of butt joint will be investigated in terms of critical ISSF. The singular stress fields including and excluding crack will be considered.

Even though the convenient analysis method of butt joint was already presented, it cannot be applied to the lap joint analysis directly since the singular stress field of lap joint is complex than butt joint. Therefore, in this research, first, a convenient analysis method for the ISSF of lap joint will be considered. The single lap joint will be used as an example to investigate the analysis method for lap joint. Then, the debonding fracture criterion for the single lap joint will be examined in terms of the critical ISSF by using this convenient analysis method. The value of critical ISSF will be investigated based on the experimental results.

Finally, by using the analysis method presented in this paper, the adhesive strength evaluation method to minimize bend effect for single lap joint will be considered in terms of the ISSF appearing at the interface corner. In addition, since the adhesive strength of double lap joint is nearly twice larger than the one of single lap joint, the equivalent conditions of strength for single lap joint and double lap joint will be investigated in terms of the ISSF.

1.3 Overview of chapters

In this study, the adhesive strength evaluation method to minimize the bend effect for single lap joint is investigated in terms of ISSF. This thesis is composed of total 7 chapters and organized as follows.

Chapter 1 gives the introduction of the applications of adhesive bonded structures

in numerous industrial sectors, such as integrated circuit (IC) technology, automobile industry and aircraft industry. The application and importance of adhesively bonded structure were investigated. Then the research purpose of this thesis is introduced, focusing on the evaluation method to minimize the ISSF for single lap joint. In order to verify this research clearly, the studies of the research on the singularity in the adhesively bonded joints are reviewed in chapter 2. It is found that there are no results about the convenient evaluation method to minimize the ISSF for single lap joint.

Since the ISSF of butt joint can be obtained conveniently by using the analysis method presented in previous studies, the debonding strength of butt joint is investigated in chapter 3. First, a homogeneous and flawless elastic adhesive layer is assumed to evaluate the butt joint strength for carbon steel/epoxy resin, aluminum/araldite, and brass/solder. It is found that the adhesive strength is always expressed as the critical ISSF. Next, a small fictitious interface edge crack is assumed at the adhesive layer to consider the singular stress field including crack. Then the debonding strength is also found to be controlled by the critical ISSF of the fictitious crack. A suitable dimension of the fictitious crack is discussed to predict the strength for adhesive joints accurately and conveniently.

In chapter 4, a convenient analysis method for the ISSF of lap joint is proposed. Since the singular stress field of lap joint is complex than butt joint, the method in chapter 3 cannot be applied to the lap joint analysis directly. The same FEM mesh pattern is applied to unknown problems and reference problems. Then, it is found that the ISSF is obtained accurately by focusing on the FEM stress at the adhesive corner. Although the singular stress is controlled by two factors for lap joints, it can be expressed almost in the same way as butt joint even if the adhesive geometries are

widely changed. Therefore, the ISSF of lap joints as well as butt joints can be obtained conveniently by using the analysis method presented in this chapter. The usefulness of the present solution is verified by comparing with the results of the conventional method.

In chapter 5, the debonding criterion of single lap joint is investigated in terms of the critical ISSF $K_{\sigma c}$ by using the analysis method presented in chapter 4. In this chapter, the value of $K_{\sigma c}$ is investigated based on the experimental results. The results show that the adhesive strength can be evaluated as $K_{\sigma c}$=const when the debonding fracture occurs (except for the specimen with very short adhesive length).

Chapter 6 shows the adhesive strength evaluation method to minimize bend effect for single lap joint. Here, the evaluation method is investigated in terms of the ISSF appearing at the interface corner. The results show that the ISSF decreases with increasing the adherend thickness. The minimum ISSF can be obtained when the adherend thickness t_1 is large enough, and the deformation angle at the interface corner is smallest when adherend thickness t_1 is large enough. In addition, the equivalent conditions of strength for single lap joint and double lap joint are investigated in terms of the ISSF. It is found that the strength of single lap joint with t_1=7mm is nearly equal to that of double lap joint with t_1=1.5mm (JIS) since the ISSFs of single lap joint and double lap joint are nearly the same. For the same reason, the strength of single lap joint is nearly equal to that of double lap joint when $t_1 \geq 25$mm.

In the last chapter of this thesis, chapter 7, main conclusions of this study are summarized.

1.4 References

[1] Hu P, Han X, Li L, Shao Q, Li WD. Effect of temperature on shear strength of adhesively bonded joints for automobile industry. ICAMMP 2011; 418-420: 1259-65.

[2] Alessandra F.Santos, Hélio Wiebeck, Roberto M.Souza, Cl áudio G. Schön. Instrumented indentation testing of an epoxy adhesive used in automobile body assembling. Polym Test 2008; 27: 632-637.

[3] Barnes TA, Pashby IR. Joining techniques for aluminium spaceframes used in automobiles: Part II — adhesive bonding and mechanical fasteners. J Mater Process Tech 2000; 99(1-3): 72-79.

[4] Edward M. Petrie. Adhesives for the assembly of aircraft structures and components: Decades of performance improvement, with the new applications of the horizon. Met Finish 2008; 106(2): 26-31.

[5] Encinas N, Oakley BR, Belcher MA, Blohowiak KY, Dillingham RG, Abenojar J, Martínez MA. Surface modification of aircraft used composites for adhesive bonding. Int J Adhes Adhes 2014; 50:157-163.

[6] Yuuki R. Mechanics of interface. 1st ed. Baifuukann, Tokyo; 1992 [in Japanese].

[7] Yasuda M. Hitachi Technical Report 40. 2003. p. 7–12.

[8] Shibutani T. Evaluation of crack initiation at interfacial edge on the basis of fracture mechanics concept and application to electronics devices (Tutorial Series: Foundations for reliability analysis). J Jpn Inst Electron Packag 2004;7 (7):639–44 [in Japanese].

[9] Hattori T, Sakata S, Hatsuda T, Murakami G. A stress singularity parameter approach for evaluating adhesive strength. JSME Int J Ser 1 Solid Mech Strength Mater 1988;31(4):718–23 [in Japanese].

[10] Shiratori M. Problems of joints in packaging of electronic devices. Trans Jpn Soc Mech Eng A 1994;60(577):1905–12 [in Japanese].

[11] Tohmyoh H, Saka M, Akaogi T. Selection of a solid layer for high-resolution acoustic imaging of IC packaging defects under dry-contact conditions. Mech Mater 2009; 41: 1172-1178.

[12] BS EN 1465:1995, "Adhesives-determination of tensile lap-shear strength of rigidto-rigid bonded assemblies".

[13] ASTM D 1002-1, "Standard test method for apparent shear strength of single-lap-joint adhesively bonded metal specimens by tension loading (metal-to-metal)", ASTM Stand, 1-5.

[14] JIS K6850:1999, Adhesives-Determination of tensile lap-shear strength of rigid-to-rigid bonded assemblies.

[15] Ikegami K, Kyogoku H, Kawagoe H, Sugibayashi T, Nono K, Fujii T, Motoie K, Yoshida F. Benchmark tests for synthetic evaluation of adhesive-joint strength(1st report, Experimental results of butt, single-lap, double-lap joints and DCB test). Trans Jpn Soc Mech Eng 1997; 63(608): 174-181.

Chapter 2 Literature review on the adhesively bonded joints

2.1 Research on singular stress field at interface corner

Since the singular stress fields usually exist at the interface corner for adhesively bonded joints[1,2], the interfacial debonding often occurs under thermal and mechanical loading[3]. So far, many studies have been made to evaluate the singularity at the interface corner. The determination method for the elastic singular stress filed around re-entrant corners in isotropic materials was first developed by Williams[4]. Then, this method was applied in the analysis of bi-material wedges [5-12] and multi-material wedges [13,14]. The studies reported that the order of the stress singularity (1-λ) at the corner changes depending on the wedge geometry and material combination. Dundurs [15,16] proposed the elastic mismatch parameters α, β to express the singularity of the material combination. Bogy[7,17-18] investigated the stress singularity at the interface corner in elastic bi-material planes. It is reported that the stresses at the interface corner approached infinity. This phenomenon can be used to explain the initiate failures from the interface corner in adhesive bonded joints. Since the eigenequation of λ is determined from the two traction free edges ($\theta = -\theta_1, \theta = \theta_2$) and an interface ($\theta = 0$) as shown in Fig. 2.1, the boundary conditions for traction free edges and interface are given in Eq.(2.1)[19,20].

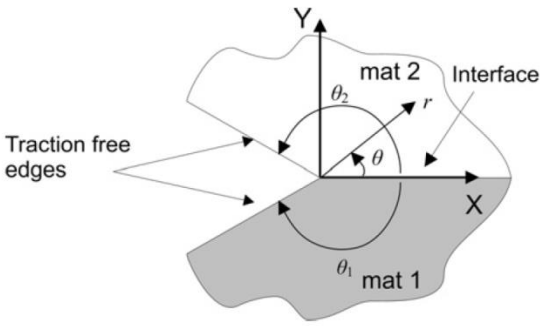

Fig.2.1 Interface corner for adhesively bonded joint

$$\begin{aligned}
&\theta=\theta_1:\ \sigma_{\theta\theta1}(r,-\theta_1)=0,\tau_{r\theta1}(r,-\theta_1)=0\\
&\theta=\theta_2:\ \sigma_{\theta\theta2}(r,\theta_2)=0,\tau_{r\theta2}(r,\theta_2)=0\\
&\theta=0:\ \sigma^1_{\theta\theta1}(r,0)=\sigma^2_{\theta\theta1}(r,0),\tau_{r\theta1}(r,\theta)=\tau_{r\theta2}(r,\theta),\\
&\qquad u_{\theta1}(r,0)=u_{\theta2}(r,0),v_{r1}(r,0)=v_{r2}(r,0)
\end{aligned} \tag{2.1}$$

For the design of engineering, it is necessary to understand the existence of singularity at the interface corner. However, the research on the singular stress field around the interface corner is still limited [11,12], the evaluation parameters and the strength evaluation method have not been established.

2.2 Research on adhesive strength

A number of studies on debonding strength have been made so far. Naito investigated the geometrical effect of adhesive thickness on the tensile strength for butt joint [21]. It is known that the adhesive strength σ_c increases with decreasing adhesive thickness. The previous studies suggested this is because more defects and cavities are included in the thick adhesive layer [22]. The experimental studies also suggested that the residual strain of adhesive layer may affect the results [23-25]. Suzuki [26-28], Reedy [29-34], Qian and Akisanya [35] , Mintzas and Nowell [20] discussed the effects of the material properties of adhesive, adherend, adhesive thickness and cure

temperature on the experimental adhesive strength of butt joint. Fig.2.2(a) shows the shapes and dimensions of the butt joint in [26-28]. It is found that the adhesive strength changes depending on the material properties, adhesive thickness and cure temperatures. In addition, the adhesive strength of scarf joint is also considered in [26-28,35,36]. Fig. 2.2(b) shows the specimen for scarf joint in [26-28]. Here, butt joint is a special case in scarf joint (scarf angle θ=90 deg). The results show that the adhesive strength of scarf joint is larger than that of butt joint, and the adhesive strength of scarf joint decreases with increasing scarf angle. However, compared with butt joint, scarf joint has some obvious disadvantages. For example, the difficult machining of the surfaces, high associated costs and requirement of specialized workers. This might be why, even though the butt joint strength is smaller than scarf joint strength, the butt joint is still widely used.

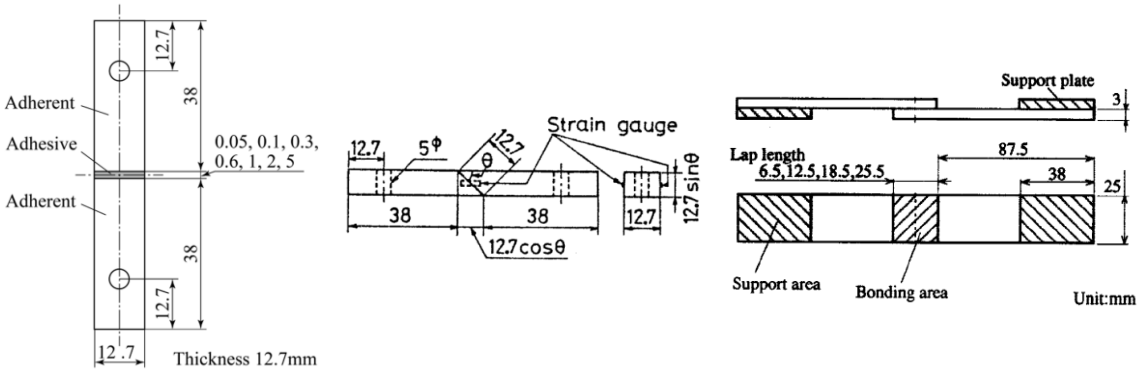

(a) Butt joint (b) Scarf joint (c) Single lap joint

Fig.2.2 Experimental specimen for adhesively bonded joints

For the three adhesively bonded joints: butt joint, scarf joint and lap joint, although the stress singularity order at interface corner for lap joint is maximal, the lap joint specimens have higher reliability than butt joint and scarf joint[36]. Amijima[37] investigated the effect of adherend properties and specimen geometry on adhesive strength of single lap joint. The test results reveal that the Young's modulus and yield

strength strongly affect the observed strength of single lap joint, and the deformations of the single lap joints subjected to the tensile shear load were also shown in this paper. Arai[38] found that both the initiation and fracture stresses decreased with increasing lap length of the single lap joint in Fig.2.2(c). The reason for this phenomenon is the increasing bending moment at both ends of the bonded overlap. The thick specimens with different adhesive lengths and adhesive thicknesses were manufactured and tested by Park [39]. The results show that the failure loads of adhesive joints of different adhesive lengths increased with the adhesive length, but the adhesive strengths decreased. However, there are still no results about the convenient evaluation method to minimize the bend effect for single lap joint.

2.3 Research on evaluation method for adhesive strength in terms of ISSF

It is known that the ISSF can be used to evaluate the strength of adhesive joint. Before the 1970s, all the studies concentrated on the order of the singular index. Started from 1970s, the researches started to study the calculate method of intensities by considering the stress around the tip and displacement fields[40-47]. Then, the researchers found that it is possible to evaluate the fracture of specimens containing monolithic [48-50] and bi-material wedges[51,52] by using the critical value of stress intensity factor (SIF). The values of the critical SIF for butt joint with different material combinations, specimen geometries, mechanical and thermal loadings have been obtained[28-34]. Penado studied the possible singular regions in single lap joint with isotropic [53] and anisotropic adherends[54]. Mintzas and Nowell [20] investigated the critical SIF for adhesively bonded joints by using William's eigenfunction expansion method in combination with a path independent contour integral method[40-45]. Fig.

2.3 shows the contour integral path in the bi-material wedge used in [20]. However, since the contour integral method requires the complex and difficult calculations such as matrix operation and numerical integration, it is difficult to be widely used and may bring low practicality.

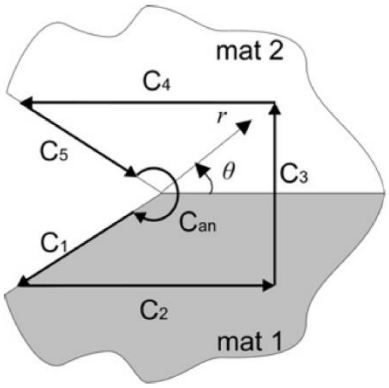

Fig.2. 3 Contour integral path in the bi-material wedge

Recently, the conveniently calculating method for ISSF of butt joint has been proposed [55-62]. The ISSF for butt joints can be obtained conveniently from the ratio of stresses at the interface corner because of only one real root of λ and the exact reference solution has been investigated[63,64]. The same FEM mesh pattern is applied to unknown problems and reference problems. Nisitani [65] proposed a convenient method (crack tip stress method) to calculate the interface stress intensity factor of a crack in homogenous material by using the FEM stress values at a crack tip. Then, this method was extended to calculate the interface stress intensity factor of interface crack problem in dissimilar materials[66,67]. Based on the proportional method, Zhang[55] found that the ISSF in Fig.2.4 (a) decreases with decreasing the adhesive thickness. The solutions for small edge interface crack in Fig.2.4(b) [56-58] and clarified material combinations effects [58-62] were also shown. It was found that the change rate of the ISSF depended on the combinations of adhesive and adherend thickness, the normalized

ISSF for the edge interface crack are not always finite depending upon Dunders' parameters.

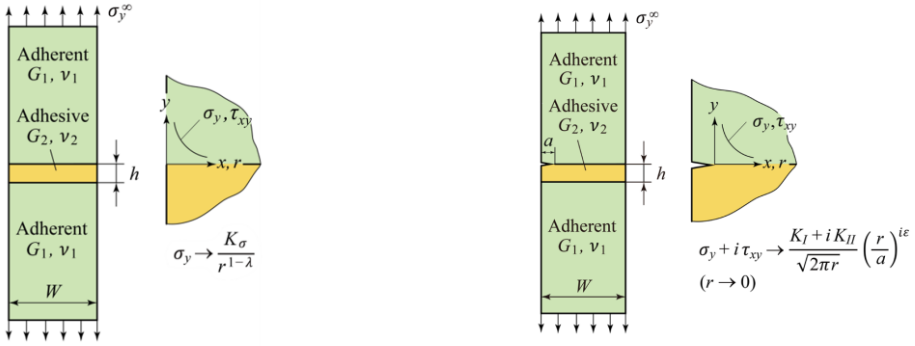

(a) Perfectly-bonded model (b) Fictitious crack model

Fig.2. 4 Analysis models for butt joint

However, since the lap joint has two real roots in most of material combination (see Fig.2.5), the singular stress field of lap joint is complex than butt joint. Therefore, the conveniently analysis method for butt joint cannot be applied to the lap joint analysis directly. Thus, the suitable and conveniently analysis method for lap joint is expected.

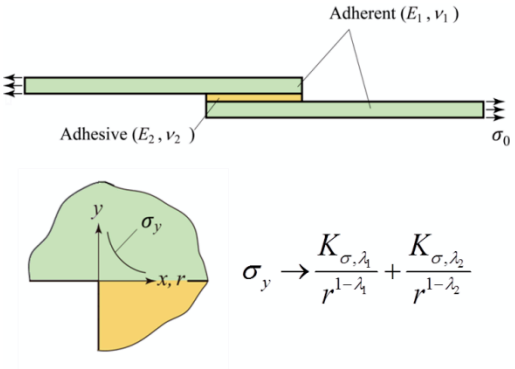

Fig.2.5 ISSF of single lap joint

2.4 References

[1] Yuuki R. Mechanics of interface. Baifuukann, Tokyo, 1993, 283p [in Japanese].

[2] Treifi M, Oyadiji SO. Evaluation of mode Ⅲ stress intensity factors for bi-material notched bodies using the fractal-like finite element method. Comput Struct 2013; 129: 99-110.

[3] Hattori T, Sakata S, Hatsuda T, Murakami G. A stress singularity parameter approach for evaluating adhesive strength. JSME Int J Ser 1 Solid Mech Strength Mater 1988; 31(4):718–23.

[4] Williams ML. Stress singularities resulting from various boundary conditions in angular corners of plates in extension. J Appl Mech 1952;56:526-8.

[5] Dempsey JP, Sinclair GB. On the singular behavior at the vertex of a bi-material wedge. J Elast 1981; 11: 317-27.

[6] Hein VL, Erdogan F. Stress singularties in a two-material wedge. Int J Fract 1971;7:317-30.

[7] Kuo MC, Bogy DB. Plane solutions for the displacement and traction-displacement problems for anisotropic elastic wedges. J Appl Mech 1974;41:197-202.

[8] Ting TCT, Chou SC. Edge singularities in anisotropic composites. Int J Solids Struct 1981;17:1057-68.

[9] Wu Z, Liu Y. Analytical solution for the singular stress distribution due to V-notch in an orthotropic plate material. Engng Fract Mech 2008;75:2367-84.

[10] Bogy DB. Edge bonded dissimilar orthogonal elastic wedges under normal and shear loadings. J Appl Mech 1966;35: 146-54.

[11] Hattori T, Sakata S, Hatsuda T, Murakami G. A stress singularity parameters approach for evaluating adhesive strength. Trans Jpn Soc Mech Eng A 1988; 54(499): 597-603 [in Japanese].

[12] Hattori T. A stress-singularity-parameter approach for evaluating adhesive strength of single-lap joints. Trans Jpn Soc Mech Eng A 1990; 56(523): 618-623.

[13] Theocaris PS. The order of singularity at a multi-wedge corner of a composite plate. Int J Engng Sci 1974;12:107-20.

[14] Carpinteri A, Paggi M. Analytical study of the singularities arising at multi-material interfaces in 2D linear elastic problems. Engng Fract Mech 2007; 74:59-74.

[15] Dundurs J. Discussion of edge bonded dissimilar orthogonal elastic wedges under normal and shear loading. J Appl Mech 1969; 36: 650-652.

[16] Dundurs J. Effect of elastic constants on stress in a composite under plane deformations. J Compos Mater 1967; 1: 310.

[17] Bogy DB. Edge-bonded dissimilar orthogonal elastic wedges under normal and shear loading. Trans ASME J Appl Mech 1968;35(3):460–6.

[18] Bogy DB. Two edge-bonded elastic wedges of different materials and wedge angles under surface tractions. Trans ASME J Appl Mech 1971;38(2):377–86.

[19] Chen DH, Nisitani H. Singular stress field in two-bonded wedges. Trans Jpn Soc Mech Eng A 1992;58(547): 457-464.

[20] Mintzas A, Nowell D. Validation of an Hcr-based fracture initiation criterion for adhesively bonded joints. Eng Fract Mech 2012;80: 13-27.

[21] Naito K, Onta M, Kogo Y. The effect of adhesive thickness on tensile and shear strength of polyimide adhesive. Int J Adhes Adhes 2012;36:77–85.

[22] Ikegami K, Kyogoku H, Kawagoe H, Sugibayashi T, Nono K, Fujii T, Motoie K, Yoshida F. Benchmark tests for synthetic evaluation of adhesive-joint strength (1st report, Experimental results of butt, single-lap, double-lap joints and DCB test). Trans Jpn Soc Mech Eng A 1997; 63(608): 174-181 [in Japanese].

[23] Yamato T, Shirahama M, Hara S. Effect of adhesive thickness on the strength of chlorinated rubber adhesive. J Soc Rubber Sci Technol 1957;30(11):842–7 [in Japanese].

[24] Yokoyama T, Nakai K, Ikeda T. Effect of specimen geometry on tensile properties of structual adhesive butt joints. In: JSME annual meeting; 2006. p. 861–2 [in Japanese].

[25] Akinmade A O, Nicholson J W. Effect of adhesive layer thickness on the bond strength of a zinc polycarboxylate dental cement. Biomaterials 1995; 16(2):149-54.

[26] Suzuki Y. Adhesive tensile strengths of scarf and butt joints of steel plates (1st Report, Relation between mechanical properties of adhesives and fracture criteria of joints). Bull JSME. 1984; 27(233): 2372-2379.

[27] Suzuki Y. Adhesive tensile strengths of scarf and butt joints of steel plates (2nd Report, Relation between mechanical properties of adhesives and fracture criteria of joints). Bull JSME. 1985; 27(233): 2372-2379.

[28] Suzuki Y. Adhesive tensile strengths of scarf and butt joints of steel plates (Relation between adhesive layer thicknesses and adhesive strengths of joints). JSME Int J. 1987; 30(265): 1042-1051.

[29] Reedy Jr ED, Guess TR. Interface corner failure analysis of joint strength: Effect of adherend stiffness. Int J of Fract 1997; 88: 305-314.

[30] Reedy Jr ED, Guess TR. Comparison of butt tensile strength data with interface corner stress intensity factor prediction. Int J Solids Struct 1993;30(21):2929-36.

[31] Reedy Jr ED, Guess TR. Additional interface corner toughness data for an adhesively-bonded butt joint. Int J of Fract 1999;98:L3-8.

[32] Reedy Jr ED. Intensity of the stress singularity at the interface corner between a bonded elastic and rigid layer. Engineering Fracture Mechanics 1990;36(4): 575-83.

[33] Reedy Jr ED, Guess TR. Interface corner stress states: plasticity effects. Int J of Fract 1996;81:269-82.

[34] Reedy Jr ED. Connection between interface corner and interfacial fracture analyses of an adhesively-bonded butt joint. Int J Solids Struct 2000;37:2429-42.

[35] QIAN Z, Akisanya A.R. An experimental investigation of failure initiation in bonded joints. Acta mater. 1998; 46(14): 4895-4904.

[36] Afendi M, Abdul Majid MS, Daud R, Abdul Rahman A, Teramoto T. Strength prediction and reliability of brittle epoxy adhesively bonded dissimilar joint. Int J Adhes Adhes 2013;45:21-31.

[37] Amijima S, Fujii T, Ebata S. On the strength of single lap adhesive bonded joints (Effect of adherend properties and joint geometry on joint strength). J Adhes Soc of Jpn 1988; 24(8): 292-299 [in Japanese].

[38] Arai M, Kobayashi H. Adhesively bonded lap joints: Fracture mechanisms and strength evaluation. Trans Jpn Soc Mech Eng A 1998; 64(619): 618-623.

[39] Park JH, Choi JH, Kweon JH. Evaluating the strengths of thick aluminum -to-aluminum joints with different adhesive lengths and thicknesses, Compos Struct 2010; 92: 2226-2235.

[40] Stern M, Soni ML. On the computation of stress intensities at fixed-free corners. Int J Solids Struct 1976;12:331-7.

[41] Sinclair GB, Okajima M, Griffin JH. Path independent integrals for computing stress intensity factors at sharp notches in elastic plates. Int J Numer Methods Engng 1984;20:999-1008.

[42] Carpenter W, Byers C. A path independent integral for computing stress intensities for V-notched cracks in a bi-material. Int J Fract 1987;35:245-68.

[43] Qian ZQ, Akisanya AR. Wedge corner stress behavior of bonded dissimilar materials. Theor Appl Fract Mech 1999;32: 209-22.

[44] Labossiere PEW, Dunn ML. Stress intensities at interface corners in anisotropic biomaterials. Engng Fract Mech 1999;62:555-76.

[45] Im S, Kim KS. An application of two-state M-integral for computing the intensity of the singular near-tip field for a generic wedge. J Mech Phys Solids 2000;48: 129-51.

[46] Munz D, Yang YY. Stresses near the edge of bonded dissimilar materials described by two stress intensity factors. Int J Fract 1993;60:169-77.

[47] Carpinteri A, Paggi M, Pugno N. Numerical evaluation of generalized stress-intensity factors in multi-layered composites. Int J Solids Struct 2006;43:627-41.

[48] Dunn ML, Suwito W, Cunningham S. Fracture initiation at sharp notches: correlation using critical stress intensities. Int J Solids Struct 1999;34:3873-83.

[49] Carpinteri A. Stress-singularity and generalized fracture toughness at the vertex of re-entrant corners. Engng Fract Mech 1987;26:143-55.

[50] Seweryn A. Brittle fracture criterion for structures with sharp notches. Engng Fract Mech 1994;47:673-81.

[51] Labossiere PEW, Dunn ML. Fracture initiation at three-dimensional biomaterial interface corners. J Mech Phys Solids 2001;49:609-34.

[52] Labossiere PEW, Dunn ML, Cunningham SJ. Application of biomaterial interface corner failure mechanics to silicon/glass anodic bonds. J Mech Phys Solids 2002;50:405-33.

[53] Penado FE. Analysis of singular regions in bonded joints. Int J Fract 2000;105:1-25.

[54] Penado FE. Singular intensity factors at biomaterial anisotropic interfaces. Compos

Struct 2001;52:323-33.

[55] Zhang Y, Noda NA, Takaishi K, Lan X. Effect of adhesive thickness on the intensity of singular stress at the adhesive dissimilar joint. J Solid Mech Mater Eng 2010;4(10):1467–79.

[56] Noda NA, Zhang Y, Lan X, Takase Y, Oda K. Stress intensity factors of an interface crack in a bonded plate under uni-axial tension. J Solid Mech Mater Eng 2010;4(7):974–87.

[57] Lan X, Noda NA, Michinaka K, Zhang Y. The effect of material combinations and relative crack size on the stress intensity factors at the crack tip of a bi-material bonded strip. Eng Fract Mech 2011;78(14):2572–84.

[58] Noda NA, Lan X. Stress intensity factors for an edge interface crack in a bonded semi-infinite plate for arbitrary material combination. Int J Solids Struct 2012;49(10):1241–51.

[59] Zhang Y, Noda NA, Takaishi K, Lan X. Stress intensity factors of a central interface crack in a bonded finite plate and periodic interface cracks under arbitrary material combinations. Eng Fract Mech 2011;78(6):1218–32.

[60] Zhang Y. Intensity of singular stress field at the end of interface under arbitrary material combination. Japan: Kyushu Institute of Technology; 2011 Ph.D. dissertation.

[61] Zhang Y, Noda NA, Wu PZ, Duan ML. A mesh-independent technique to evaluate stress singularities in adhesive joints. Int J Adhes Adhes 2015;57:105– 17 the corrigendum of authorship is published in Int J Adhes Adhes 60, 2015.

[62] Noda NA, Oda K. Interaction effect of stress intensity factors for any number of collinear interface cracks. Int J Fract 1997;84:117–28.

[63] Chen DH, Nisitani H. Intensity of singular stress field near the interface edge point of a bonded strip. Trans Jpn Soc Mech Eng A 1993;59:2682-6.

[64] Noda NA, Shirao R, Li J, Sugimoto JS. Intensity of singular stress fields causing interfacial debonding at the end of a fiber under pullout force and transverse tension. Int J Solids Struct 2007;44:4472–91.

[65] Nisitani H, Kawamura T, Fujisaki W, Fukuda T. Determination of highly accurate values of stress intensity factor or stress concentration factor of plate specimen by FEM. Trans Jpn Soc Mech Eng A 1999;65(629);26-31.

[66] Nisitani H, Teranisi T, Kukuyama F. Stress intensity factor analysis of a bimaterial plate based on the crack tip stress method. Trans Jpn Soc Mech Eng 2003;69:1203-8[in Japanese].

[67] Oda K, Kamisugi K, Noda NA. Analysis of stress intensity factor for interface cracks based on proportional method. Trans Jpn Soc Mech Eng A 2009;75 (752):476–82 [in Japanese].

Chapter 3 Debonding strength evaluation for butt joint in terms of the intensity of singular stress at the interface corner with and without fictitious crack

3.1 Introduction

Adhesively bonded joints are economical, practical and easy to make; thus they have been widely used in a variety of industries [1-9], such as integrated circuit (IC) technology. With the development of IC technology, the size of IC chip has been enlarged, and the package has been made thinner and smaller. It has been reported that when a plastic IC package is in the thermal environment or subjected to mechanical loading, the interfacial debonding often occurs [10-13]. So the debonding evaluation has become more and more an important issue in the design of IC packages. However, due to the mathematical difficulties, few analytical methods are available for interfacial debonding, and a more practical and rational method is required.

A number of studies on debonding strength have been made so far [14-16]. Naito investigated the geometrical effect of adhesive thickness on the tensile and shear strength for butt and single lap joints [5]. It is known that the adhesive strength σ_c increases with decreasing the adhesive thickness [2-5]. The previous studies suggested this is because more defects and cavities are included in the thick adhesive layer [17]. The experimental studies also suggested that the residual strain of adhesive layer may affect the results [18-21]. Suzuki discussed the experimental adhesive strength in Fig.2.1 (a) when S35C JIS medium carbon steel plates are bonded by epoxy resin [22]. In this study, the specimens are very carefully prepared to exclude the defect and

residual strain. Therefore in this paper, first, we consider Suzuki's results because the defect and residual strain may be excluded in the experiment.

Recently the authors have found that the intensity of the singular stress in Fig.2.1 (b) decreases with decreasing the adhesive thickness [23]. The authors have also shown the solution for small edge interface crack [24-26] and clarified material combinations effects [26-30]. In this study, therefore, debonding criterion will be considered in terms of the intensities of the singular stress based on the solutions. Therefore, two models are considered: one is the perfectly-bonded model as shown in Fig.3.1 (b), and the other is fictitious crack model as shown in Fig.3.1(c). Then the critical debonding conditions will be discussed.

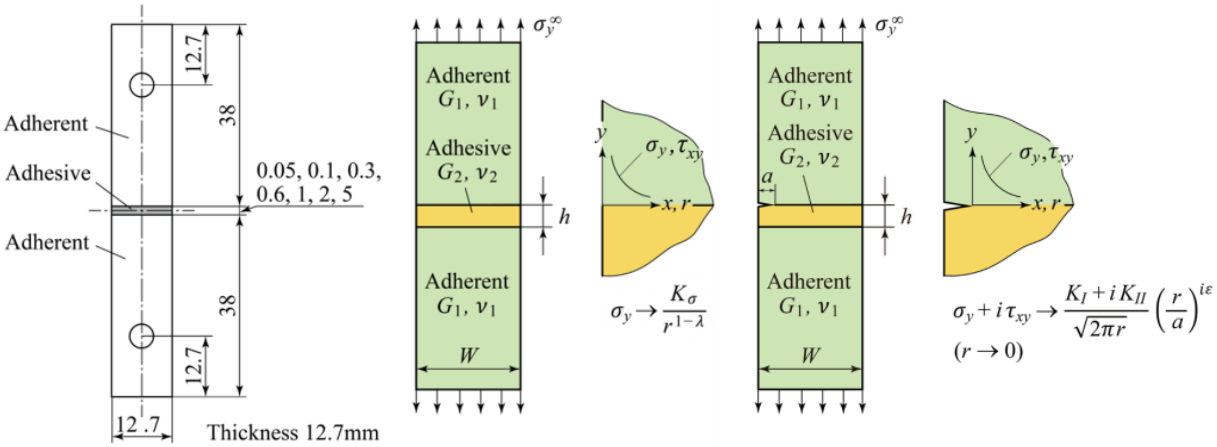

(a) (b) (c)

Fig.3.1 Experimental specimen and two kinds of models used in this study. (a) Experimental specimen, (b) Perfectly-bonded model, (c) Fictitious crack model.

Generally speaking, there are two types of approaches to explain the adhesive strength:

(1) Effect of dimension of adhesive layer is mainly considered assuming homogeneous adhesive layer without focusing on defects and residual strain.

(2) Effect of non-homogeneity such as defect and residual strain in the adhesive layer

is mainly considered without focusing on the geometrical effects.

One may think the most useful approach would certainly account for both geometry and defects. However, for example, in standard fracture mechanics approach, a cracked homogeneous elastic body is usually considered without considering any other defects. In this sense, in this study, to evaluate the adhesive strength simply and conveniently, we will focus on the intensity of singular stress based on the approach (1) without considering other defects and residual strain. Then, if something cannot be explained, approach (2) should be considered in the future, the authors think.

3.2 Debonding strength evaluation in terms of the intensity of singular stress field at the interface corner without crack

3.2.1 Convenient analysis method for the corner stress intensity factor

Here, we consider Fig. 3.2 to explain the outline of the method of analysis for the corner stress intensity factor. The details are indicated in [23, 28, 29]. For the adhesive joint as shown in Fig. 3.2, it is known that the interface stress σ_y has singularity in the form $\sigma_y \propto 1/r^{1-\lambda}$ when $\alpha(\alpha-2\beta)>0$. Here, α, β denote the Dundurs' material composite parameters defined in Eq. (3.1).

$$\alpha=\frac{G_1(\kappa_2+1)-G_2(\kappa_1+1)}{G_1(\kappa_2+1)+G_2(\kappa_1+1)},\ \beta=\frac{G_1(\kappa_2-1)-G_2(\kappa_1-1)}{G_1(\kappa_2+1)+G_2(\kappa_1+1)},\ \kappa_j=\begin{cases}\dfrac{3-\nu_j}{1+\nu_j} & (\text{plane stress})\\ 3-4\nu_j & (\text{plane strain})\end{cases}\quad (j=1,2) \tag{3.1}$$

The notation λ in Table 3.1 denotes the singular index, and the values of λ can be determined from Eq. (3.2) [31, 32].

$$\left[\sin^2\left(\frac{\pi}{2}\lambda\right)-\lambda^2\right]^2\beta^2+2\lambda^2\left[\sin^2\left(\frac{\pi}{2}\lambda\right)-\lambda^2\right]\alpha\beta+\lambda^2\left(\lambda^2-1\right)\alpha^2+\frac{\sin^2(\pi\lambda)}{4}=0 \tag{3.2}$$

When the singularity exists near the interface corner, the minimum root λ in Eq.

(3.2) should be in the range $0 \le \mathrm{Re}(\lambda) \le 1$. The corner stress intensity factor K_σ at the adhesive dissimilar joint is defined as

$$K_\sigma = \lim_{r \to 0} \left[r^{1-\lambda} \times \sigma_y^{real}(r) \right]. \tag{3.3}$$

The dimensionless of dimensionless corner stress intensity factor F_σ is defined by the following equation [23].

$$F_\sigma = \frac{K_\sigma}{\sigma_y^\infty (W)^{1-\lambda}} = \frac{\lim_{r \to 0} \left[r^{1-\lambda} \times \sigma_y^{real}(r) \right]}{\sigma_y^\infty (W)^{1-\lambda}} \tag{3.4}$$

Table 3.2 shows the stress σ_y^{FEM} obtained by applying the finite element method (FEM) when $h/W = 0.001$ and $h/W \ge 1$ since the reference problem for $h/W \ge 1$ has the exact solution [33]. It is seen that σ_y^{FEM} varies depending on the finite element mesh size due to the singularity of the real stress σ_y^{real}.

$$K_\sigma \ne \lim_{r \to 0} \left[r^{1-\lambda} \times \sigma_y^{FEM}(r) \right] \tag{3.5}$$

Therefore, we consider the ratio $\sigma_y^{FEM} / \sigma_{y*}^{FEM}$ since the error is controlled by the mesh size. It should be noted that the ratio of the stress is independent of the mesh size.

As shown in Eq. (3.6), the ratio of corner stress intensity factor K_σ^* / K_σ is controlled by the ratio of stress $\lim_{r \to 0} [\sigma_y^*(r) / \sigma_y(r)]$. Here, an asterisk (*) means the values of the reference problem.

$$\frac{K_\sigma^*}{K_\sigma} = \frac{\sigma_y^{\infty *} (W)^{1-\lambda} F_\sigma^*}{\sigma_y^\infty (W)^{1-\lambda} F_\sigma} = \frac{F_\sigma^*}{F_\sigma} = \lim_{r \to 0} \frac{\left[r^{1-\lambda} \times \sigma_y^{FEM\,*}(r) \right]}{\left[r^{1-\lambda} \times \sigma_y^{FEM}(r) \right]} \tag{3.6}$$

To obtain the corner stress intensity factor from the ratio, a reference problem as shown in Fig.3.2 will be used because the exact corner stress intensity factor has been investigated. The authors think this method shown above is convenient to analyze the corner stress intensity factors.

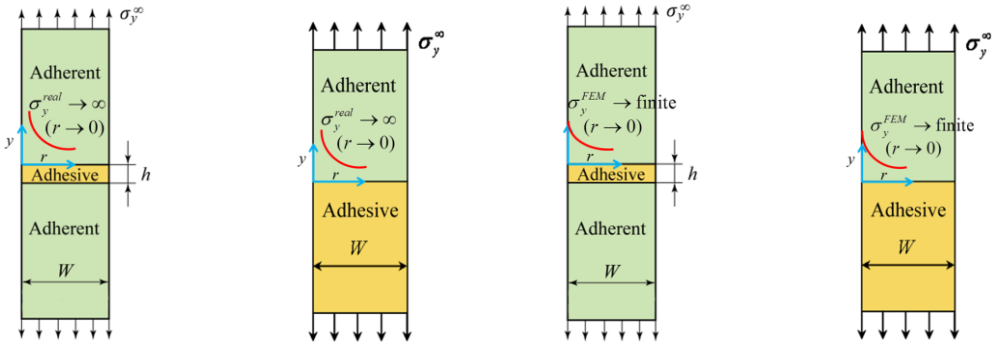

Fig.3.2 Real stress σ_y^{real} for (a) $h/W=0.001$, (b) $h/W\geq 1$ and FEM stress σ_y^{FEM} for (c) $h/W=0.001$, (d) $h/W\geq 1$.

Table 3.1 Material properties of adherent and adhesives.

	Combination		Young's modulus E [GPa]	Poisson's ratio ν	ε	α	β	λ
A	Adherent	Medium carbon steel S35C	210	0.30	-0.0641	0.969	0.199	0.685
	Adhesive	Epoxy resin A	3.14	0.37				
B	Adherent	Medium carbon steel S35C	210	0.30	-0.0607	0.978	0.188	0.674
	Adhesive	Epoxy resin B	2.16	0.38				

Table 3.2 Stress distributions for bonded strip under tension shown in Fig. 3.2 obtained by different mesh size when $h/W=0.001$.

Smallest mesh size $e_{\min}=1/3^8$ around the edge			Smallest mesh size $e_{\min}=1/3^4$ around the edge		
r/W	$\sigma_y^{FEM}\big\vert_{h/W=0.001}$	$\sigma_y^{FEM}\big\vert_{h/W=0.001}/\sigma_{y*}^{FEM}$	r/W	$\sigma_y^{FEM}\big\vert_{h/W=0.001}$	$\sigma_y^{FEM}\big\vert_{h/W=0.001}/\sigma_{y*}^{FEM}$
0	1.414	0.525	0	1.072	0.524
1/6561000	1.177	0.525	1/81000	0.889	0.522
2/6561000	1.138	0.525	2/81000	0.859	0.522
3/6561000	1.109	0.525	3/81000	0.838	0.522
4/6561000	1.088	0.525	4/81000	0.824	0.523
5/6561000	1.071	0.525	5/81000	0.813	0.525

3.2.2 Adhesive strength expressed as a constant corner stress intensity factor $K_{\sigma c}$

In this study, the adhesively bonded specimens used by Suzuki [22] in Fig. 3.1 are analyzed where the adherents S35C are bonded with adhesive epoxy resin. In this experiment, the authors prepared for the specimen very carefully to exclude the defect and residual strain. The adhesive was treated with vacuum degassing, and then kept at room temperature for 50-60 days. The Young's modulus of the epoxy adhesive may depend on the constituents of the particle size, material, grain form, dispersant and hardening condition. The difference between epoxy adhesive A, B may be depending on these factors but they are not described in detail. Here, in order to evaluate the adhesive strength conveniently, we consider the average elastic properties of epoxy including fillers. The elastic parameters of the adherent and adhesives are tabulated in Table 3.1. In this study, the experimental strength value σ_c is the maximum value of average axial stress obtained by dividing the tensile load by the area of the specimen cross section normal to the load. The load-strain relations are all linear up to the breaking point, which shows that brittle fracture occurred [22]. The fracture was initiated in the vicinity of the adherent surface of either one of the corners of the adhesion plane [22].

The experimental tensile adhesive strength shown in Fig. 3.1 (a) are tabulated in Table 3.3 with different thicknesses of adhesive layer ($h = 0.05$, 0.1, 0.3, 0.6, 1.0, 2.0, 5.0 [mm]). As shown in Table 3.3, with decreasing adhesive thickness, the bond strength increases gradually. The previous studies suggested that since the residual strain and defect are included in adhesive layer, the strength may decrease when adhesive thickness is thin enough [18, 34]. In this research, in order to explain the results of Table

3.3 conveniently, we assume the adhesive layer as a homogeneous material assuming no defect and residual strain.

Table 3.3 The experimentally obtained adhesive strength in Fig. 3.1(a) expressed by $\sigma_y^{\infty} = \sigma_c$.

h [mm]	h/W	Medium carbon steel S35C, Epoxy resin A						Medium carbon steel S35C, Epoxy resin B			
		Measured values [MPa]					Average ± SD [MPa]	Measured values [MPa]			Average ± SD [MPa]
0.05	0.00394	47.7	50.0	58.4	63.5	66.5	57.2 ± 7.34	72.8	77.6	79.9	76.8 ± 2.96
0.1	0.00787	44.3	49.8	52.0	57.0	63.5	53.3 ± 6.52	70.2	71.5	72.6	71.4 ± 0.981
0.3	0.0236	28.6	30.8	32.5	34.2	36.5	32.5 ± 2.72	45.5	50.9	52.6	49.7 ± 3.03
0.6	0.0472	21.9	24.8	25.2	28.2	29.6	25.9 ± 2.71	39.6	40.0	43.9	41.2 ± 1.94
1.0	0.0787	21.5	21.5	21.9	23.5	24.4	22.6 ± 1.18	21.1	26.5	28.4	25.3 ± 3.09
2.0	0.157	14.8	18.1	18.2	19.9	20.9	18.4 ± 2.08	18.1	19.7	21.3	19.7 ± 1.31
5.0	0.394	11.4	11.4	13.6	15.0	15.6	13.4 ± 1.76	12.4	12.4	16.0	13.6 ± 1.70

SD : Standard deviation

Table 3.4 Adhesive strength σ_c and critical value of corner stress intensity factor $K_{\sigma c} = F_{\sigma}\sigma_c W^{1-\lambda}$ assuming perfectly bonded model.

h/W	Medium carbon steel S35C, Epoxy resin A			Medium carbon steel S35C, Epoxy resin B		
	σ_c [MPa]	F_{σ}	$K_{\sigma c}$ [MPa.m$^{0.315}$]	σ_c [MPa]	F_{σ}	$K_{\sigma c}$ [MPa.m$^{0.326}$]
0.001	–	0.0435	–	–	0.0396	–
0.00394	57.2	0.0671	0.970 ± 0.125	76.8	0.0620	1.15 ± 0.0442
0.00787	53.3	0.0831	1.12 ± 0.137	71.4	0.0778	1.34 ± 0.0184
0.01	–	0.0902	–	–	0.0842	–
0.0236	32.5	0.119	0.978 ± 0.0818	49.7	0.112	1.34 ± 0.0818
0.0472	25.9	0.150	0.981 ± 0.102	41.2	0.142	1.41 ± 0.0665
0.0787	22.6	0.178	1.02 ± 0.0532	25.3	0.171	1.04 ± 0.127
0.1	–	0.194	–	–	0.187	–
0.157	18.4	0.231	1.07 ± 0.121	19.7	0.223	1.06 ± 0.0703
0.394	13.4	0.335	1.13 ± 0.149	13.6	0.331	1.09 ± 0.135
0.5	–	0.363	–	–	0.360	–
$K_{\sigma c(average)}$	–	–	1.04 ± 0.0643	–	–	1.20 ± 0.144

The analytical values of F_σ are listed in Table 3.4, which are dimensionless corner stress intensity factor obtained by using the calculation method in Chapter 3.2.1 with varying the adhesive thickness h in Fig. 3.1 (b). Then the critical values of the corner stress intensity factor $K_{\sigma c}$ are tabulated in Table 3.4 [see Eq. (3.7)].

$$K_{\sigma c} = F_\sigma \sigma_c W^{1-\lambda} \tag{3.7}$$

Furthermore, the relationship between $K_{\sigma c}$ and the thickness of adhesive layer h is plotted in Fig. 3.3 [23]. Here, the open circles denote $K_{\sigma c}$ values obtained from experiment, the solid circles denote the average value of $K_{\sigma c}$ for each h/W, and the solid line shows the average value of the solid circles. Fig. 3.3 shows that the solid circles are distributed around the solid line with slight variations. Table 3.4 indicates the average and standard deviation of the critical intensity as $K_{\sigma c} = 1.04 \pm 0.0643$ [MPa·m$^{0.315}$] for S35C steel/Epoxy A (Combination A, see Table 1) and $K_{\sigma c} = 1.20 \pm 0.144$ [MPa·m$^{0.326}$] for S35C steel/Epoxy B (Combination B, see Table 1). The coefficients of variations are 0.0618 for Combination A, and 0.120 for Combination B, which are defined as the standard deviation/ average.

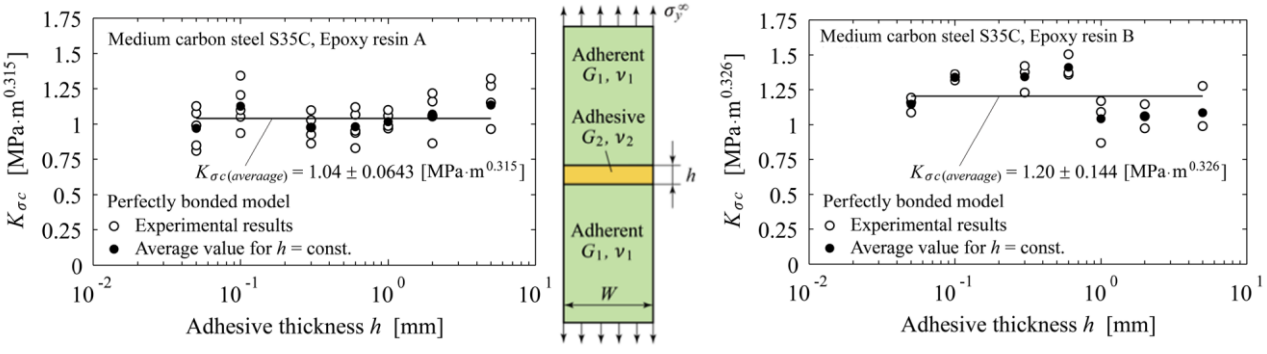

(a) (b)

Fig.3.3 Adhesive strength for bonded Medium carbon steel S35C expressed as a constant critical value of corner stress intensity factor $K_{\sigma c}$. (a) Medium carbon steel S35C, Epoxy resin A, (b) Medium carbon steel S35C, Epoxy resin B.

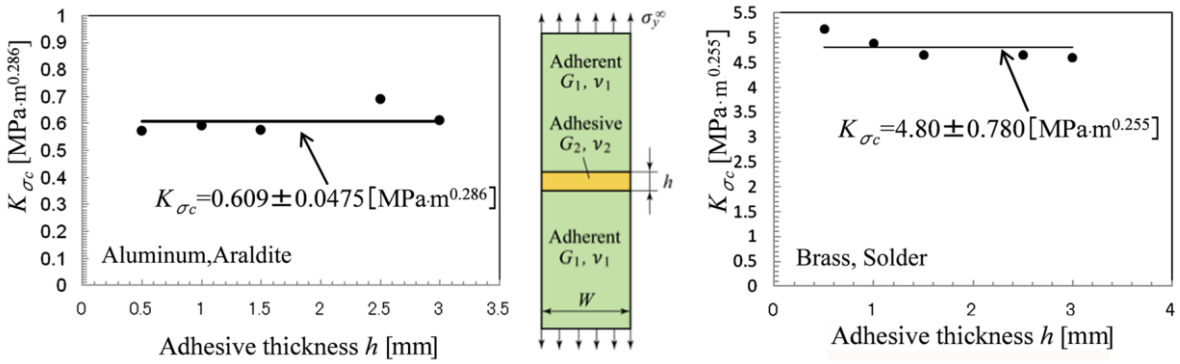

(a) (b)

Fig.3.4 Adhesive strength for bonded Aluminum and bonded Brass expressed as a constant critical value of corner stress intensity factor $K_{\sigma c}$. (a) Aluminum, Araldite, (b) Brass, Solder.

Fig. 3.4 shows the results obtained for Aluminum/Araldite and Brass/Solder as indicated in Table 3.5 as Combinations C and D. The adhesive strengths σ_c were obtained from Akisanya and Meng [35]. Microscopic examination of the fracture surface revealed that failure occurred at the interface corner and the initiated crack grew along the interface in both Combinations C and D. Table 3.6 shows the average and standard deviation as $K_{\sigma c} = 0.609 \pm 0.0475$ [MPa · m$^{0.286}$] for Combination C and $K_{\sigma c} = 4.80 \pm 0.780$ [MPa · m$^{0.255}$] for Combination D. The coefficients of variations are 0.0780, 0.163.

Table 3.5 Material properties of adherent and adhesives.

Combination			Young's modulus E [GPa]	Poisson's ratio ν	ε	α	β	λ
C	Adherent	Aluminum	70	0.35	-0.0664	0.94	0.21	0.714
	Adhesive	Araldite	2.1	0.36				
D	Adherent	Brass	90	0.34	-0.0485	0.86	0.15	0.745
	Adhesive	Solder	6.4	0.39				

Table 3.6 Adhesive strength σ_c and critical value of corner stress intensity factor $K_{\sigma c} = F_\sigma \sigma_c W^{1-\lambda}$ assuming perfectly bonded model.

h [mm]	Aluminum, Araldite			Brass, Solder		
	σ_c [MPa]	F_σ	$K_{\sigma c}$ [MPa·m$^{0.286}$]	σ_c [MPa]	F_σ	$K_{\sigma c}$ [MPa·m$^{0.255}$]
0.5	12.4	0.173	0.574	90.3	0.186	5.18
1.0	10.2	0.217	0.593	68.9	0.230	4.89
1.5	8.61	0.250	0.577	57.3	0.263	4.66
2.5	8.49	0.303	0.690	47.2	0.320	4.66
3.0	7.03	0.325	0.612	43.2	0.345	4.60
$K_{\sigma c(average)}$	—	—	0.609±0.0475	—	—	4.80±0.780

From Fig. 3.3 and Fig. 3.4, it is seen that the adhesive strength can be evaluated by the constant corner stress intensity factor as $K_{\sigma c}$ =const. Meanwhile, Suzuki's results were evaluated in terms of H singular stress and expressed as H_{cr}=const [36, 37]. Furthermore, H_{cr} criterion is also applied to evaluate scarf joint. However, local geometrical difference disables us for comparing those results because of different singular index singular fields [38-41]. On the other hand, the fictitious crack model enables us to compare the results independent of the local geometrical difference. In the following, we will focus on the application of the fictitious crack model.

Akisanya and Meng [35] state that in the case of Brass/Solder joint, the stress intensity factor is not suitable to characterize the initiation of fracture because of the large plastic zone size. However, Fig. 3.4 (b) shows the adhesive strength can be expressed almost as a constant critical value of corner stress intensity factor $K_{\sigma c}$. Usually, in the fracture mechanics approach, the small size of plastic zone is necessary and known as small scale yielding condition. However, in the present approach, we considered the singular stress at the interface. In this case, the yielding condition is not clear because two different material characters should be considered and the real

interface and the model's interface may be different. Therefore, in this study, the elastic singular stress is discussed. Then, if something cannot be explained in the future by this approach, plasticity should be considered, the authors think.

3.3 Debonding strength evaluation in terms of the intensity of singular stress field at the interface corner with crack

3.3.1 Convenient analysis method for interface crack

Here, we consider Fig. 3.5 to explain the outline of the method of analysis for interface crack. The details are indicated in [24, 25, 42, 43, 44]. The two different interface crack problems A and B in Fig. 3.5 have same crack length a and material combination, assuming the interface stress intensity factor of problem A is available and that for problem B has not been solved yet. An asterisk (*) means the value of the reference problem A. Then, the problems A and B are solved by applying the same FEM mesh pattern around the interface crack tip.

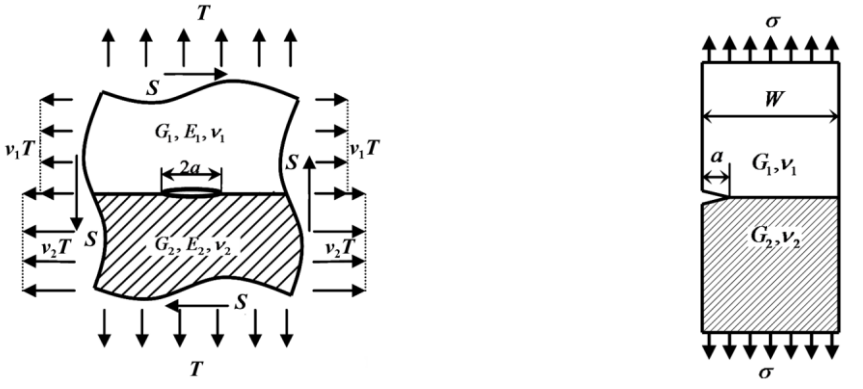

(a) (b)

Fig.3.5 (a) Reference problem A and (b) a given unknown problem B to explain the method of analysis.

The analytical solution of the singular stress factors at the crack tip for the reference problem takes the form

$$K_I^* + iK_{II}^* = (T + iS)\sqrt{\pi a}(1 + 2i\varepsilon), \tag{3.8}$$

where T, S are the remote uniform tension and shear applied to the bonded dissimilar half-planes.

The stresses at the crack tip of the reference problem are expressed as

$$\begin{aligned} \sigma_{y0}^{FEM*} &= \sigma_{y0}^{FEM*}|_{T=1,S=0} \times T + \sigma_{y0}^{FEM*}|_{T=0,S=1} \times S, \\ \tau_{xy0}^{FEM*} &= \tau_{xy0}^{FEM*}|_{T=1,S=0} \times T + \tau_{xy0}^{FEM*}|_{T=0,S=1} \times S. \end{aligned} \tag{3.9}$$

Then, the finite element stress components at the crack tip for the problems A and B have relation

$$\left[\frac{\tau_{xy0}^{FEM*}}{\sigma_{y0}^{FEM*}}\right]_A = \left[\frac{\tau_{xy0}^{FEM}}{\sigma_{y0}^{FEM}}\right]_B. \tag{3.10}$$

Let T=1, the value of S can be determined as

$$S = \frac{\sigma_{y0}^{FEM} \times \tau_{xy0}^{FEM*}|_{T=1,S=0} - \tau_{xy0}^{FEM} \times \sigma_{y0}^{FEM*}|_{T=1,S=0}}{\tau_{xy0}^{FEM} \times \sigma_{y0}^{FEM*}|_{T=0,S=1} - \sigma_{y0}^{FEM} \times \tau_{xy0}^{FEM*}|_{T=0,S=1}}. \tag{3.11}$$

Finally, the singular intensity factors for the given unknown problem B can be yielded using the proportional relationship as given in Eq. (3.12).

$$[K_I]_B = \frac{[\sigma_{y0}^{FEM}]_B}{[\sigma_{y0}^{FEM*}]_A}[K_I^*]_A, \quad [K_{II}]_B = \frac{[\tau_{xy0}^{FEM}]_B}{[\tau_{xy0}^{FEM*}]_A}[K_{II}^*]_A \tag{3.12}$$

Fig.3.6 shows the stress distributions near the interface crack tip for problems A and B if Eq. (3.9) and Eq. (3.10) are satisfied. It is seen that the singular stress field of the interface crack is controlled by $\tau_{xyo}^{FEM} / \sigma_{yo}^{FEM}$ at the crack tip. The authors think this method is convenient to analyze the interface stress intensity factors.

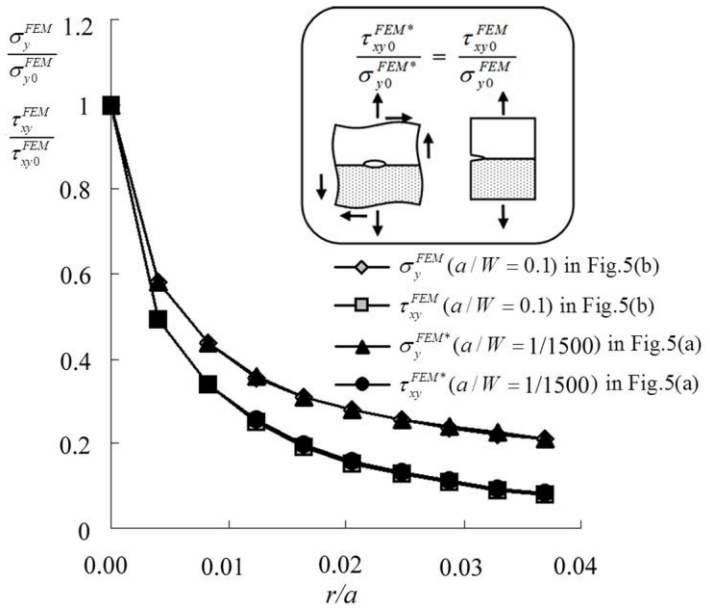

Fig.3.6 Comparison of relative stress distributions near crack tip.

3.3.2 Usefulness of fictitious crack model

In general, singular stress field near edge interface can be expressed as shown in the following equation by using three terms, that is, (A) singular index λ_m, (B) angle function with vertices singularity $f_{ij}(\theta)$, (C) stress intensity factor K_m.

$$\sigma_{ij}(r,\theta) = \sum_{m=1} \frac{K_m}{r^{1-\lambda_m}} f_{ij}(\theta), \ (ij = r,\theta,r\theta) \tag{3.13}$$

Singular indexes λ_m may be obtained from solving the characteristic equation, which expresses geometrical boundary conditions around the singular point. The roots λ_m can be single or multiple real roots as expressed in equation (3.2); and the roots can be complex roots expressed by different types of equations.

Consider an IC package as shown in Fig. 3.7. To evaluate the interface strength, we have to calculate K_m considering distinct singular index λ_m and angle function $f_{ij}(\theta)$ at five points A to E. Although the material combinations are the same at points A, B, C, the singular indexes λ_m at points A, B, C are different as well as the angle functions

$f_{ij}(\theta)$ and intensities K_m .

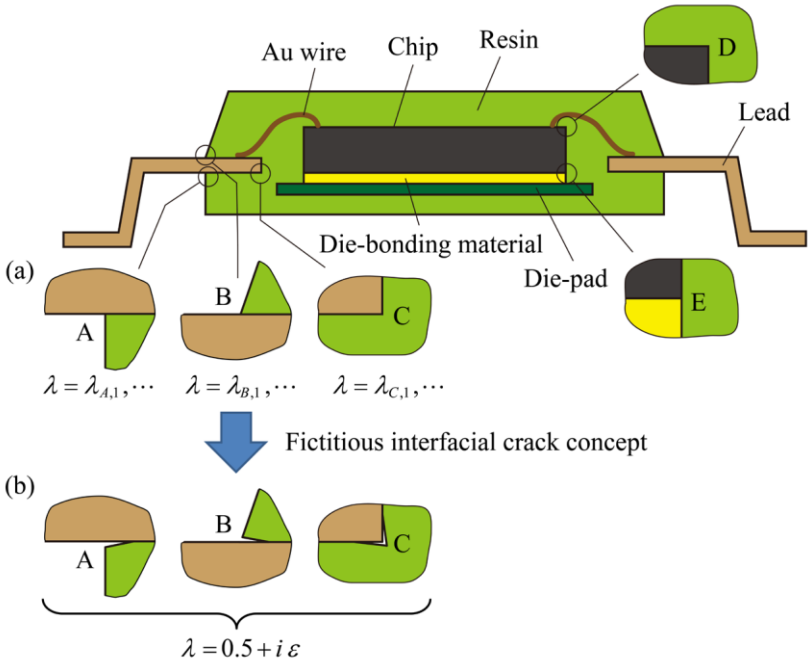

Fig.3.7 An example of IC package; (a) perfectly bonded model; (b) fictitious crack model

In this way, the singular stress field for dissimilar materials bonded interface varies depending on the geometry and material combination, and therefore it is difficult to compare the intensities.

The fictitious crack model as shown in Fig. 3.1(c) has some advantages when we have to compare the interface strength at points A, B, and C. A fictitious crack is not a real debonding. A fictitious crack is just used to evaluate the severity at the end of the interface. This is because the interface crack always has the distinct singular stress field, whose singular index is $\lambda = 1/2 + i\varepsilon$ and expressed in Eq. (3.14) [24-28, 30, 42, 43].

$$[\sigma_y + i\,\tau_{xy}]_{\theta=0} = \frac{K_I + iK_{II}}{\sqrt{2\pi r}}\left(\frac{r}{a}\right)^{i\varepsilon},\ \varepsilon = \frac{1}{2\pi}\ln\left(\frac{1-\beta}{1+\beta}\right) \tag{3.14}$$

$$K_I + iK_{II} = (F_I + iF_{II})\,\sigma_y^{\infty}\sqrt{\pi a} \tag{3.15}$$

Here, K_I and K_{II} are the interface stress intensity factors. The real part of the

singular index λ=1/2 is independent of the shape of the edge interface and also independent of the material combination. Since the singular stress of edge interface is expressed by the unified singular stress field, the advantage of assuming fictitious crack model can be summarized as follows [45, 46].

(1) The distinct singular stress field as Eq. (3.13) is not necessarily to be obtained. Although the points A, B, C have distinct singular fields, assumed fictitious cracks always provide the same singular fields in Eq. (3.14) [26,42,43] (see Fig.3.7(b)).

(2) If the critical value of the interface stress intensity factor is available at A, for example, the results can be applied to other points B and C since they have the same singular fields.

3.3.3. An example of fictitious crack model application

By taking an example of V-shaped notch problem in Fig.3.8, the usefulness of the fictitious crack will be explained. The details are indicated in [39-41]. First, the static tensile strength of notched acrylic resin plate will be discussed by applying the notch stress intensity factors K_{I,λ_1} without using fictitious crack.

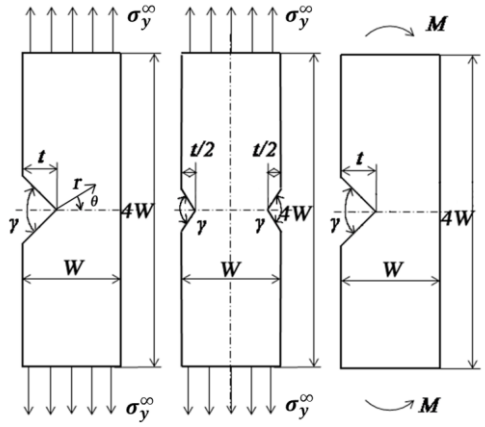

Fig.3.8 V-shaped sharp notch specimens of acrylic resin (W =40mm).

The singular stress at the sharp V-notch can be expressed in Eq. (3.16) [47].

$$\sigma_{ij} = f_{ij}^{I}(\theta)\frac{K_{I,\lambda_1}}{r^{1-\lambda_1}} = \frac{\lambda_1}{\sqrt{2\pi}}\{(\lambda_1+1)\sin[\lambda_1(\pi-\gamma)] - \lambda_1\sin[\lambda_1(\pi-\gamma)+\gamma] + \sin(\lambda_1\pi)\}\frac{K_{I,\lambda_1}}{r^{1-\lambda_1}} \quad (3.16)$$

In Eq. (3.16), the singular stress field around the notch tip is defined in terms of notch stress intensity factor K_{I,λ_1}, which is defined in Eq. (3.17).

$$K_{I,\lambda_1} = \lim_{r\to 0}[\sqrt{2\pi}r^{1-\lambda_1}\sigma_\theta(r,\theta)|_{\theta=0}] \quad (3.17)$$

Here, $\sigma_\theta(r,\theta)|_{\theta=0}$ is the stress along the bisector of the notch, and λ_1 is the singularity index, in the range of $0<\lambda<1$, obtained from the following eigenequation:

$$\sin\left[\lambda_1(2\pi-\gamma)\right] = \lambda_1\sin\gamma\,. \quad (3.18)$$

The notch stress intensity factor K_{I,λ_1} can be expressed in Eq. (3.19) [47]. Several dimensionless notch stress intensity factors F_{I,λ_1} are indicated in [39-41, 47-51].

$$K_{I,\lambda_1} = F_{I,\lambda_1}\sigma^\infty\sqrt{\pi}t^{1-\lambda_1},\ \sigma^\infty = \begin{cases}\sigma_y^\infty & :\text{Tension}\\ 6M/W^2 & :\text{Bending}\end{cases} \quad (3.19)$$

Fig.3.9 shows the critical value K_{IC,λ_1} experimentally obtained, which is necessary to fracture the specimens with the same notch opening angle $\gamma = 60^o$. As shown in Fig.3.9, it is found that K_{IC,λ_1} is almost constant independent of the notch depth t/W and whether the notch is single or double.

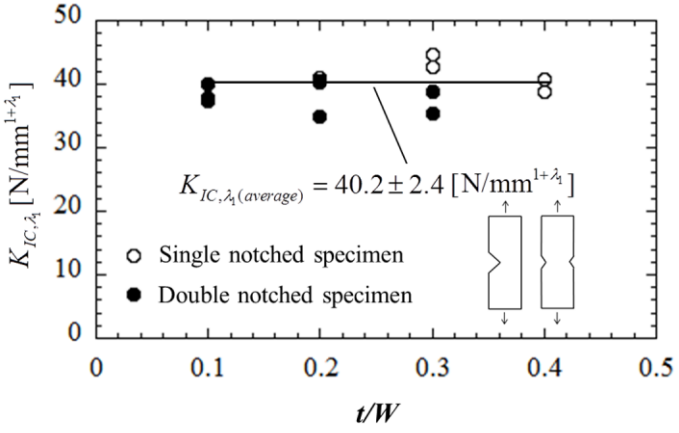

Fig.3.9 Experimental results of critical value of notch stress intensity factor K_{IC,λ_1} for notches of $\gamma = 60^o$ with various notch depths t.

Fig.3.10 shows the experimental results of K_{IC,λ_1} with various notch opening angles γ. The value is depending on the notch opening angle γ which has distinct singular stress index λ_1. As shown in Table 3.7, the value of λ_1 increases with increasing the notch opening angle γ. On this sense, the sharp V-notch fracture problem is different from the crack fracture problem because the critical value of notch stress intensity factors necessary to notch fracture is a function of the notch opening angle γ. Thus, even for mode I fracture problem, many data of K_{I,λ_1} are necessary under different notch opening angle although only K_{IC} can be applied to all the crack problems.

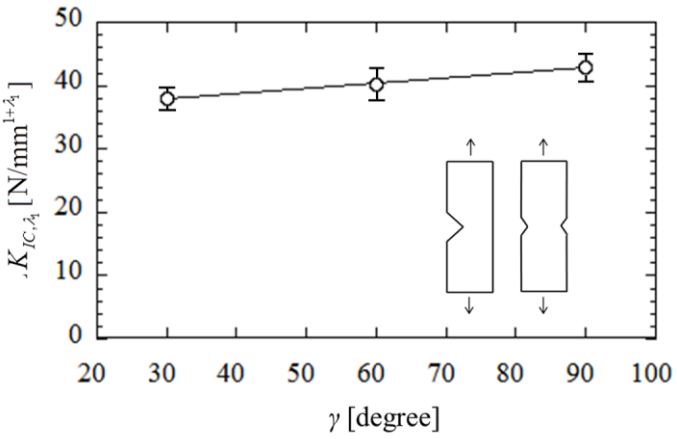

Fig.3.10 Results of critical value of notch stress intensity factor K_{IC,λ_1} (average ± standard deviation).

Table 3.7 Results of notch stress intensity factor K_{IC,λ_1} and singularity index λ_1

γ	K_{IC,λ_1} [N/mm$^{1+\lambda_1}$]	λ_1
30°	38.0 ± 1.2	0.50145
60°	40.2 ± 2.4	0.51222
90°	42.9 ± 1.6	0.54448

Therefore, another fracture criterion using fictitious crack is useful in application

[39-41]. Here, the critical values of stress intensity factors can be estimated from the mechanical properties of the considered material such as the tensile strength σ_B or the critical value of stress intensity factor K_{IC}.

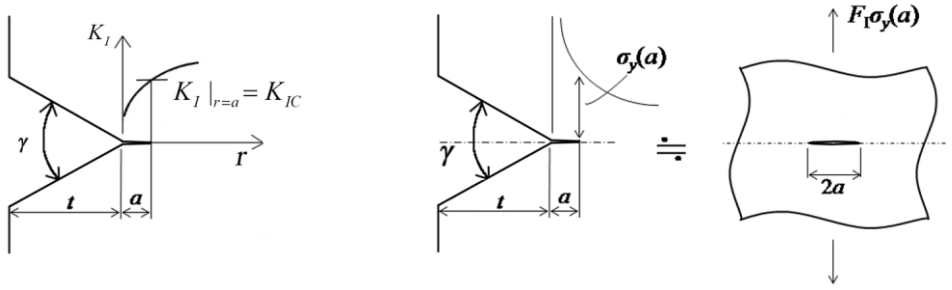

(a) (b)

Fig.3.11 (a) Fracture criterion at notch root based on (b) the results for dimensionless stress intensity factor.

In Fig.3.11, a fictitious crack is considered at the notch tip. Here, the fracture at the notch tip is simulated by propagation of this small fictitious crack, with a length of "a", imagined at the notch tip. Fracture occurs when the stress intensity factor at the crack tip K_I is larger than the critical value K_{IC} [see Eq. (3.20)].

$$K_I\big|_{r=a} \geq K_{IC} \tag{3.20}$$

The crack length "a" obtained by Eq.(3.20) is related to the fracture process zone size.

The fracture strength for the sharp notch specimen is discussed by using the stress intensity factor of small fictitious crack. The dimensionless stress intensity factor F_I at the crack tip is expressed as shown in Eq.(3.21) by using the stress $\sigma_y(a)$ ahead of the notch without crack as shown in Fig.3.11 [41].

$$F_I = \frac{K_I}{\sigma_y(a)\sqrt{\pi a}} = \frac{K_I}{K_{I,\lambda_1}} a^{0.5-\lambda_1} \tag{3.21}$$

Therefore the fracture criterion Eq.(3.20) can be expressed as

$$K_I\big|_{r=a} = F_I a^{\lambda_1 - 0.5} K_{I,\lambda_1} \geq K_{IC}. \tag{3.22}$$

The dimensionless stress intensity factor and singularity index are tabulated in Table.3.8. Here, the F_I decreases with increasing the notch opening angle γ. Fig.3.12 indicates that F_I for $\gamma = 90^\circ$ has the same value when $a/t \leq 0.005$ independent of t/W.

Table 3.8 Dimensionless stress intensity factor F_I and singularity index γ for $a/t \leq 0.005$

γ	F_I	λ_1
15°	0.995	0.50018
30°	0.985	0.50145
60°	0.961	0.51222
90°	0.953	0.54448

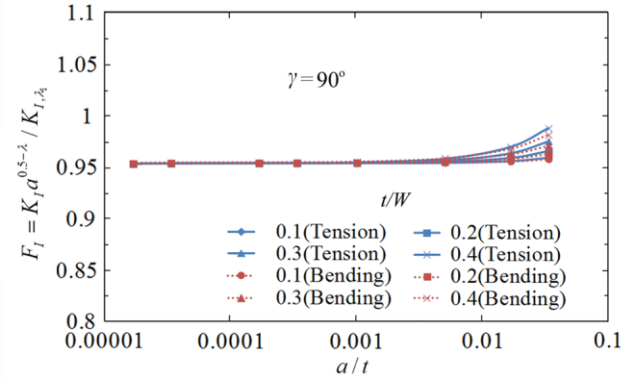

Fig.3.12 Relation between dimensionless stress intensity factor F_I and a/t when $\gamma = 90^\circ$.

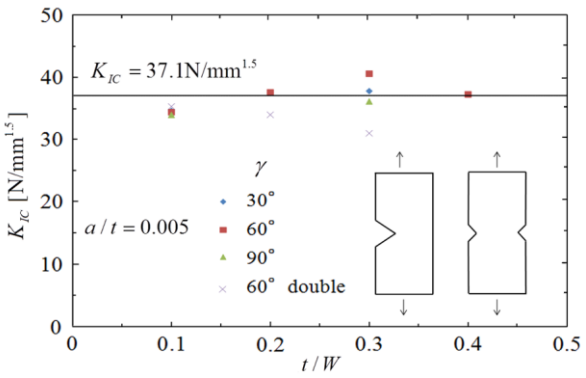

Fig.3.13 Static strength of acrylic resin with different V-shaped notches expressed as a constant critical value of stress intensity factor K_{IC} by assuming fictitious crack $a/t = 0.005$ (a =0.02-0.08mm) in Fig.3.11.

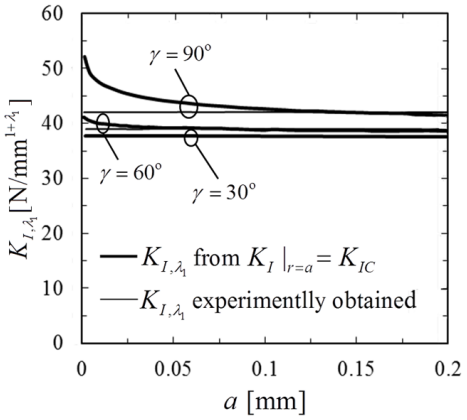

Fig.3.14 Predicted K_{I,λ_1} based on $K_I|_{r=a} = K_{IC}$ in Fig. 3.11 and K_{I,λ_1} experimentally obtained.

The relationships between the critical value of stress intensity factor K_{IC} and t/W are plotted in Fig.3.13 for $a/t = 0.005$. It is found that the K_{IC} is almost constant independent of a/t and opening angle γ. In this case, all sharp V-notch fractures can be expressed as $K_{IC} = 37.1\text{N/mm}^{1.5}$ independent of notch opening angle γ and notch depth t assuming the fictitious crack length $a/t = 0.005$. In Fig.3.14 a suitable fictitious crack length is discussed by comparing the predicted K_{I,λ_1} obtained from Eq.(3.22) $K_I|_{r=a} \geq K_{IC}$ with the experimental value [40]. It is seen that the predicted K_{I,λ_1} is insensitive to the crack length "a" since the value is almost constant except for very

small value of "a". In [40] a fictitious crack whose length a = 0.042 – 0.166mm is found to be suitable, but Fig.3.13 shows smaller values of a =0.02mm~ also can be used with $K_{IC} = 37.1\text{N/mm}^{1.5}$.

3.3.4 Adhesive strength expressed as a constant interface stress intensity factor K_{IC} by assuming fictitious crack

The calculation method described in chapter 3.2.2 and [24, 25] is applied and the dimensionless interface stress intensity factors F_I are listed with the ratio F_{II}/F_I in Table 3.9 under a/W =0.01, 0.1. Except for the extremely thin adhesive layer, it is seen that the debonding strength can be expressed as a constant value of K_{IC}. Since the value of F_{II}/F_I is also almost constant regardless of a/W, the critical values of the mode I interface stress intensity factors K_{IC} are tabulated in Table 3.9 [see Eq. (3.23)].

$$K_{IC} = F_I \sigma_c \sqrt{\pi a} \tag{3.23}$$

The relationships between the critical interface stress intensity factors K_{IC} and the adhesive thickness h are plotted in Fig. 3.15 for $a/W = 0.01$ and in Fig. 3.16 for $a/W = 0.1$.

As shown in Table 3.9, when $a/W = 0.01$, the average value and standard deviations $K_{IC} = 0.446 \pm 0.0356\ [\text{MPa}\sqrt{\text{m}}]$ for Combination A, and $K_{IC} = 0.551 \pm 0.0576\ [\text{MPa}\sqrt{\text{m}}]$ for Combination B. The coefficients of variation are 0.0789 and 0.105, respectively. When $a/W = 0.1$, the average value and standard deviations $K_{IC} = 0.844 \pm 0.0517\ [\text{MPa}\sqrt{\text{m}}]$ for Combination A, and $K_{IC} = 1.01 \pm 0.107\ [\text{MPa}\sqrt{\text{m}}]$ for Combination B. The coefficients of variation are 0.0603 and 0.106, respectively. It is seen that the adhesive strength can be evaluated from the critical value of interface stress intensity factor K_{IC} =const.

Table 3. 9 Adhesive strength σ_c and critical value of interface stress intensity factor K_{IC} assuming fictitious crack model when $a/W = 0.01$, 0.1.

(a) Medium carbon steel S35C, Epoxy resin A

h/W	σ_c [MPa]	$a/W = 0.01$			$a/W = 0.1$		
		F_I	F_{II}/F_I	K_{IC} [MPa$\sqrt{\text{m}}$]	F_I	F_{II}/F_I	K_{IC} [MPa$\sqrt{\text{m}}$]
0.001	–	0.256	−0.507	–	0.214	−0.703	–
0.00394	57.2	0.367	−0.418	0.419 ± 0.0538	0.237	−0.577	0.856 ± 0.110
0.00787	53.3	0.457	−0.415	0.487 ± 0.0596	0.271	−0.521	0.914 ± 0.112
0.01	–	0.492	−0.424	–	0.288	−0.504	–
0.0236	32.5	0.631	−0.446	0.410 ± 0.0343	0.372	−0.446	0.765 ± 0.0640
0.0472	25.9	0.790	−0.430	0.409 ± 0.0427	0.478	−0.416	0.783 ± 0.0818
0.0787	22.6	0.952	−0.407	0.429 ± 0.0224	0.579	−0.418	0.825 ± 0.0431
0.1	–	1.04	−0.397	–	0.633	−0.425	–
0.157	18.4	1.26	−0.379	0.463 ± 0.0524	0.744	−0.434	0.863 ± 0.0976
0.394	13.4	1.88	−0.356	0.503 ± 0.0660	1.06	−0.400	0.899 ± 0.118
0.5	–	1.94	−0.353	–	1.15	−0.382	–
$K_{IC(average)}$	–	–	–	0.446 ± 0.0356	–	–	0.844 ± 0.0517

(σ_c : Experimental result, $K_{IC} = F_I \sigma_c \sqrt{\pi a}$)

(b) Medium carbon steel S35C, Epoxy resin B

h/W	σ_c [MPa]	$a/W = 0.01$			$a/W = 0.1$		
		F_I	F_{II}/F_I	K_{IC} [MPa$\sqrt{\text{m}}$]	F_I	F_{II}/F_I	K_{IC} [MPa$\sqrt{\text{m}}$]
0.001	–	0.228	−0.509	–	0.183	−0.699	–
0.00394	76.8	0.340	−0.423	0.521 ± 0.0201	0.208	−0.577	1.010 ± 0.0389
0.00787	71.4	0.431	−0.425	0.615 ± 0.00844	0.244	−0.523	1.100 ± 0.0151
0.01	–	0.466	−0.436	–	0.261	−0.506	–
0.0236	49.7	0.604	−0.464	0.599 ± 0.0365	0.347	−0.450	1.089 ± 0.0664
0.0472	41.2	0.767	−0.442	0.631 ± 0.0297	0.455	−0.423	1.182 ± 0.0557
0.0787	25.3	0.936	−0.415	0.474 ± 0.0578	0.557	−0.429	0.891 ± 0.109
0.1	–	1.04	−0.402	–	0.611	−0.438	–
0.157	19.7	1.26	−0.382	0.466 ± 0.0330	0.723	−0.450	0.900 ± 0.0597
0.394	13.6	1.93	−0.357	0.500 ± 0.0653	1.06	−0.409	0.908 ± 0.113
0.5	–	1.99	−0.353	–	1.15	−0.389	–
$K_{IC(average)}$	–	–	–	0.551 ± 0.0576	–	–	1.01 ± 0.107

(σ_c : Experimental result, $K_{IC} = F_I \sigma_c \sqrt{\pi a}$)

Table 3. 10 Adhesive strength σ_c and critical value of interface stress intensity factor K_{IC} assuming fictitious crack model when $a/W = 0.01$, 0.1.

(a) Aluminum, Araldite

h [mm]	σ_c [MPa]	$a/W = 0.01$			$a/W = 0.1$		
		F_I	F_{II}/F_I	K_{IC} [MPa$\sqrt{\text{m}}$]	F_I	F_{II}/F_I	K_{IC} [MPa$\sqrt{\text{m}}$]
0.5	12.4	0.823	0.413	0.180	0.530	0.400	0.367
1.0	10.2	1.042	0.386	0.188	0.663	0.406	0.379
1.5	8.61	1.210	0.372	0.185	0.754	0.413	0.364
2.5	8.49	1.483	0.359	0.223	0.898	0.407	0.427
3.0	7.03	1.598	0.355	0.199	0.959	0.400	0.378
$K_{IC(average)}$	–	–	–	0.195 ± 0.015	–	–	0.383± 0.023

(σ_c : Experimental result, $K_{IC} = F_I \sigma_c \sqrt{\pi a}$)

(b) Brass, Solder

h [mm]	σ_c [MPa]	$a/W = 0.01$			$a/W = 0.1$		
		F_I	F_{II}/F_I	K_{IC} [MPa$\sqrt{\text{m}}$]	F_I	F_{II}/F_I	K_{IC} [MPa$\sqrt{\text{m}}$]
0.5	90.3	0.799	0.394	1.279	0.601	0.353	3.044
1.0	68.9	0.994	0.360	1.213	0.695	0.380	2.686
1.5	57.3	1.149	0.344	1.166	0.764	0.396	2.454
2.5	47.2	1.412	0.328	1.180	0.893	0.391	2.360
3.0	43.2	1.527	0.324	1.168	0.953	0.382	2.307
$K_{IC(average)}$	–	–	–	1.201± 0.042	–	–	2.570 ± 0.270

(σ_c : Experimental result, $K_{IC} = F_I \sigma_c \sqrt{\pi a}$)

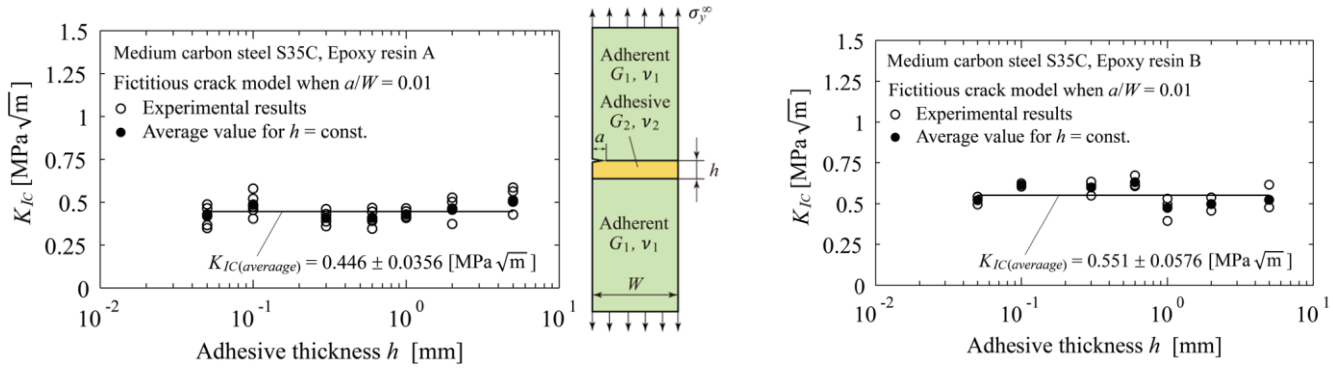

(a) (b)

Fig.3.15 Adhesive strength for bonded Medium carbon steel S35C expressed as a constant critical value of interface stress intensity factor K_{IC} by assuming fictitious crack $a/W = 0.01$. (a) Medium carbon steel S35C, Epoxy resin A, (b) Medium carbon steel S35C, Epoxy resin B.

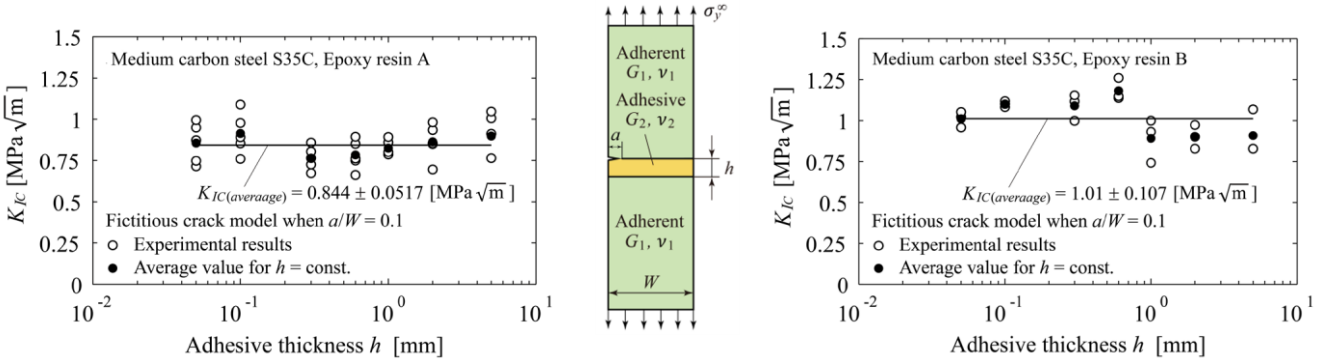

(a) (b)

Fig.3.16 Adhesive strength for bonded Medium carbon steel S35C expressed as a constant critical value of interface stress intensity factor K_{IC} by assuming fictitious crack $a/W = 0.1$. (a) Medium carbon steel S35C, Epoxy resin A, (b) Medium carbon steel S35C, Epoxy resin B.

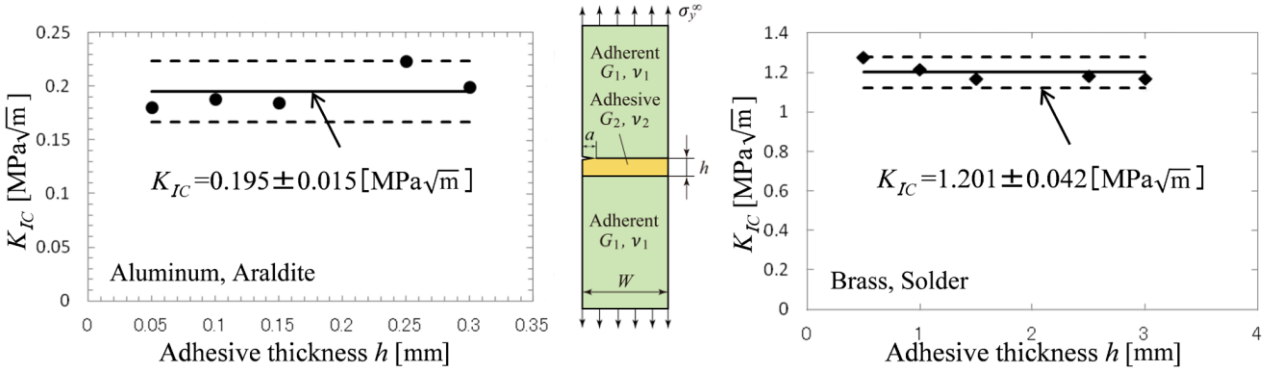

(a) (b)

Fig.3.17 Adhesive strength for bonded Aluminum and bonded Brass expressed as a constant critical value of interface stress intensity factor K_{IC} by assuming fictitious crack $a/W = 0.01$. (a) Aluminum, Araldite, (b) Brass, Solder.

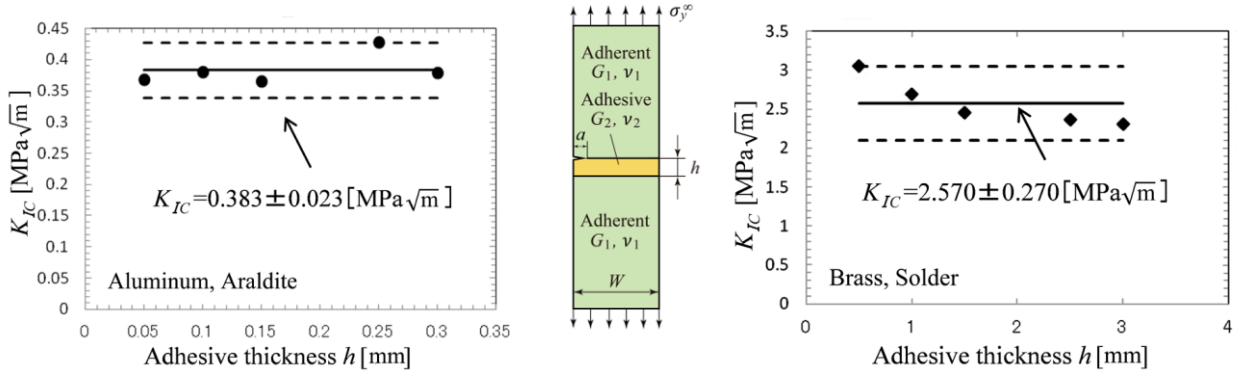

(a) (b)

Fig.3.18 Adhesive strength for bonded Aluminum and bonded Brass expressed as a constant critical value of interface stress intensity factor K_{IC} by assuming fictitious crack $a/W = 0.1$. (a) Aluminum, Araldite, (b) Brass, Solder.

In a similar way, Akisanya's results are indicated in Table 3.10, Fig. 3.17 and Fig. 3.18. From the comparison between Tables 3.4, 3.6, 3.9, 3.10 and Figs. 3.3, 3.4, 3.15-18, no significant difference can be seen for the variation between the $K_{\sigma c}$ and the K_{IC}. In other words, there is no large difference between the results from the perfectly bonded model and the fictitious crack model.

3.3.5 Adhesive strength predicted by assuming different fictitious crack lengths

The previous chapter shows that the adhesive strength can be evaluated accurately, even though $a/W = 0.1$ is not very small as the fictitious crack length. In this section, we discuss the suitable length of the fictitious crack based on the interface stress intensity factor [26]. Fig. 3.19 shows F_I vs. a/W for the geometry of Fig. 3.1(c). The F_I value goes to infinity as $a/W \to 0$. This is due to the singular stress appearing at the end of interface when there is no crack. Therefore the following constant C_I should be introduced because C_I takes a constant value as $a/W \to 0$ [26]. The detail explanation of the constant C_I is shown in the Appendix B [26].

$$C_I = F_I \left(\frac{a}{W} \right)^{1-\lambda} \tag{3.24}$$

Fig. 3.20 shows C_I vs. a/W for Fig. 3.1 (c) based on the results in Table 3.11. When the crack length is sufficiently small compared to the thickness of the adhesive layer, the C_I value is almost constant. The interface stress intensity factor can be expressed as shown in Eq. (3.25).

$$K_I = F_I \sigma \sqrt{\pi a} = C_I \left(\frac{W}{a} \right)^{1-\lambda} \sigma \sqrt{\pi a} = \frac{C_I}{F_\sigma} \frac{F_\sigma W^{1-\lambda} \sigma}{a^{1-\lambda}} \sqrt{\pi a} = \frac{C_I}{F_\sigma} \frac{K_\sigma}{a^{1-\lambda}} \sqrt{\pi a} \tag{3.25}$$

As shown in Eq. (3.25), if the ratio C_I / F_σ is independent of the crack length, K_I is controlled by the stress field without crack K_σ. This means that the short crack is placed at the singular stress field at the interface end. When the adhesive layer is thin, and h/W is small, K_I can be controlled by the singular stress field without crack if we take small a/W. Adhesive strength can be expressed from K_{IC} as shown in Eq. (3.26).

$$\sigma_c = \frac{K_{\sigma c}}{F_\sigma W^{1-\lambda}} = \frac{K_{IC}}{F_I \sqrt{\pi a}} = \left(\frac{a}{W} \right)^{1-\lambda} \frac{K_{IC}}{C_I \sqrt{\pi a}} \tag{3.26}$$

And therefore,

$$K_{IC} = \frac{C_I\sqrt{\pi a}}{F_\sigma a^{1-\lambda}} K_{\sigma c} = \frac{C_I^*}{a^{0.5-\lambda}} K_{\sigma c} = C_I^* K_{\sigma c} a^{\lambda-0.5},\ C_I^* = \sqrt{\pi}\frac{C_I}{F_\sigma}. \tag{3.27}$$

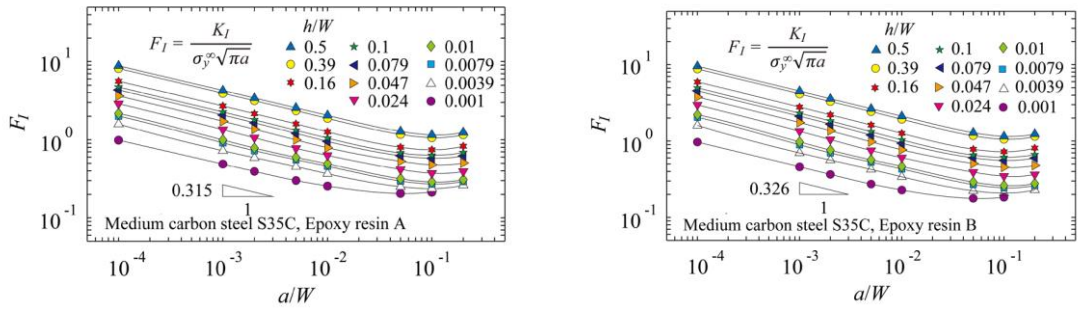

(a) (b)

Fig.3.19 Relationship between F_I and a/W for bonded Medium carbon steel S35C. (a) Medium carbon steel S35C, Epoxy resin A, (b) Medium carbon steel S35C, Epoxy resin B.

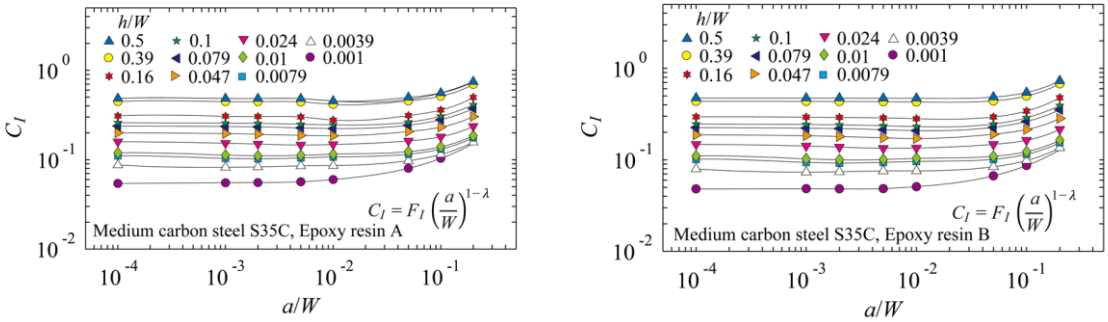

(a) (b)

Fig.3.20 Relationship between C_I and a/W for bonded Medium carbon steel S35C. (a) Medium carbon steel S35C, Epoxy resin A, (b) Medium carbon steel S35C, Epoxy resin B.

Table 3. 11 F_I and C_I values in Fig. 3.1(c).

(a) Medium carbon steel S35C, Epoxy resin A

a/W	$h/W=0.0472$		$h/W=0.0787$		$h/W=0.1$		$h/W=0.157$		$h/W=0.394$		$h/W=0.5$		$h/W\geq 1$	
	F_I	C_I	F_I	C_I	F_I	C_I	F_I	C_I	F_I	C_I	F_I	C_I	F_I	C_I
0.0001	3.640	0.2000	4.341	0.2386	4.729	0.2599	5.611	0.3083	8.155	0.4482	8.838	0.4857	9.838	0.5406
0.001	1.724	0.1957	2.073	0.2353	2.265	0.2571	2.699	0.3063	3.938	0.4470	4.269	0.4845	4.753	0.5394
0.002	1.363	0.1925	1.648	0.2327	1.804	0.2547	2.156	0.3044	3.159	0.4460	3.426	0.4838	3.818	0.5391
0.005	0.9932	0.1872	1.205	0.2271	1.323	0.2493	1.596	0.3008	2.355	0.4437	2.559	0.4821	2.861	0.5391
0.01	0.7897	0.1851	0.9520	0.2232	1.048	0.2457	1.262	0.2958	1.880	0.4406	2.054	0.4816	2.309	0.5413
0.05	0.5301	0.2063	0.6251	0.2433	0.6764	0.2633	0.8000	0.3114	1.170	0.4554	1.279	0.4979	1.489	0.5718
0.1	0.4780	0.2314	0.5792	0.2804	0.6331	0.3065	0.7435	0.3600	1.062	0.5140	1.154	0.5585	1.320	0.6391
0.2	0.5049	0.3041	0.6209	0.3740	0.6856	0.4129	0.8272	0.4982	1.157	0.6968	1.241	0.7477	1.387	0.8354

(b) Medium carbon steel S35C, Epoxy resin B

a/W	$h/W=0.0472$		$h/W=0.0787$		$h/W=0.1$		$h/W=0.157$		$h/W=0.394$		$h/W=0.5$		$h/W\geq 1$	
	F_I	C_I	F_I	C_I	F_I	C_I	F_I	C_I	F_I	C_I	F_I	C_I	F_I	C_I
0.0001	3.779	0.1877	4.539	0.2254	4.962	0.2464	5.936	0.2948	8.797	0.4369	9.569	0.4752	10.70	0.5314
0.001	1.743	0.1834	2.113	0.2222	2.317	0.2437	2.784	0.2929	4.143	0.4358	4.507	0.4742	5.040	0.5302
0.002	1.365	0.1800	1.665	0.2196	1.830	0.2414	2.207	0.2910	3.298	0.4349	3.591	0.4735	4.018	0.5299
0.005	0.9784	0.1739	1.201	0.2134	1.327	0.2358	1.616	0.2872	2.434	0.4326	2.654	0.4718	2.981	0.5300
0.01	0.7671	0.1709	0.9364	0.2087	1.038	0.2312	1.264	0.2816	1.927	0.4293	2.115	0.4712	2.388	0.5321
0.05	0.5063	0.1907	0.6015	0.2265	0.6543	0.2461	0.7809	0.2941	1.173	0.4418	1.290	0.4856	1.491	0.5616
0.1	0.4545	0.2146	0.5568	0.2628	0.6114	0.2886	0.7234	0.3415	1.057	0.4987	1.154	0.5448	1.330	0.6280
0.2	0.4794	0.2837	0.5974	0.3535	0.6632	0.3924	0.8078	0.4780	1.148	0.6796	1.237	0.7322	1.391	0.8230

Fig. 3.21 shows the relation between K_{IC} and "a". Here, it should be noted that this K_{IC} is a fictitious critical intensity factor when a fictitious crack is assumed. To express the same adhesive strength σ_c, the fictitious K_{IC} value increases with increasing the fictitious crack length "a". When $a/W \leq 0.01$ with $W = 12.7\text{mm}$, for example, since $\lambda - 0.5 = 0.685 - 0.5 = 0.185$ for Combination A, we have $K_{IC} = C_I^* K_{\sigma c} a^{0.185}$. Since $C_I^* = \sqrt{\pi} C_I / F_\sigma$, if C_I / F_σ is independent of the crack length "a", we have $K_{IC} \propto a^{\lambda - 0.5} K_{\sigma c}$.

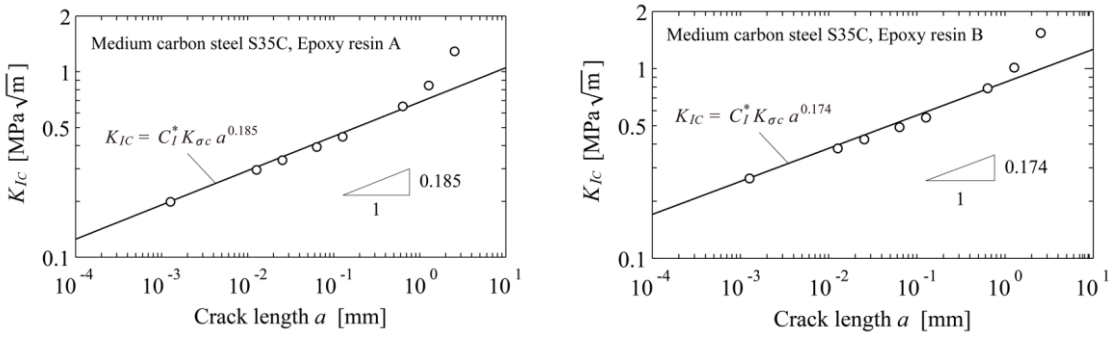

(a) (b)

Fig.3.21 Relationship between K_{IC} and "a" for bonded Medium carbon steel S35C. (a) Medium carbon steel S35C, Epoxy resin A, (b) Medium carbon steel S35C, Epoxy resin B.

Fig. 3.22 shows the relationship between C_I/F_σ and a/W. It is found that the adhesive strength can be evaluated conveniently and accurately independent of the fictitious crack length. Furthermore, except for thin adhesive layer, the adhesive strength can be estimated for a wide range of adhesive layer thickness almost independent of fictitious crack length.

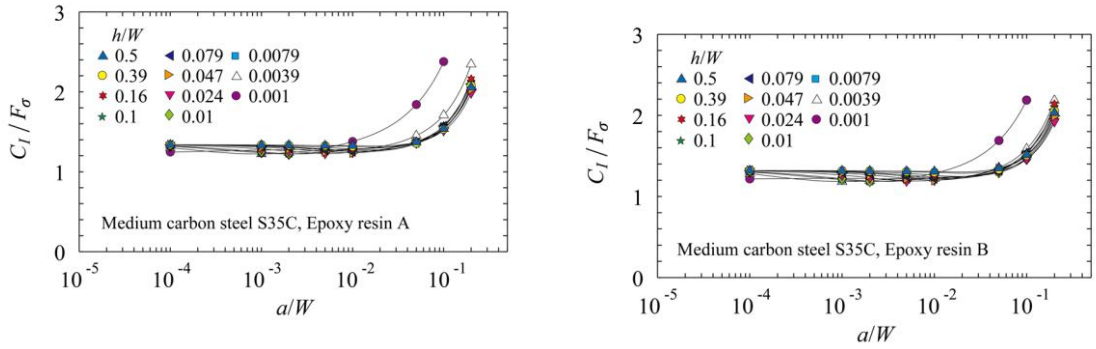

(a) (b)

Fig.3.22 Relationship between C_I/F_σ and a/W for bonded Medium carbon steel S35C. (a) Medium carbon steel S35C, Epoxy resin A, (b) Medium carbon steel S35C, Epoxy resin B.

Assume debonding happens at the average value of $K_{\sigma c\,(average)}$ obtained in Chapter 3.2.2. Then, Table 3.12 and Fig. 3.23 indicate the adhesive strength σ_c, which are calculated from the Eq. (3.28). The error is also indicated from the comparison of the

experimental results σ_c in Table 3.3.

$$\sigma_c = \frac{K_{\sigma c\,(average)}}{F_\sigma\, W^{1-\lambda}} \tag{3.28}$$

Assume debonding happens at the fictitious fracture toughness for a/W =0.01, 0.1 obtained in chapter 3.3.3. Then, Table 3.12 and Fig. 3.23 indicate the adhesive strength calculated from Eq. (3.29). The error is also indicated from the comparison of the experimental results σ_c in Table 3.3.

$$\sigma_c = \frac{K_{IC\,(average)}}{F_I \sqrt{\pi a}} \tag{3.29}$$

As shown in Table 3.12 the error is 11.4% under a/W =0.01 and 10.3% under a/W =0.1 for Combination A, and 16.4% under a/W =0.01 and 14.4% under a/W =0.1 for Combination B. It is found that the adhesive strength can be predicted with nearly the same accuracy of the perfectly bonded models. The error for Combination B is rather larger compared to the error for Combination A. This is probably because the number of test specimens for Combination B is only three affecting the error. With increasing the number the error may decrease. It may be also concluded that small fictitious crack length provides the same accuracy for the perfectly bonded model.

In this chapter, the fictitious critical interface stress intensity factor K_{IC} is used to evaluate the adhesive butt joint strength. The fictitious crack length in the range $a/W \le 0.1$ can be used since the fictitious K_{IC} varies depending on the a/W. If K_{IC} is measured experimentally and used in this evaluation, the crack length a/W should be determined by considering the fracture process zone mentioned in chapter 3.3.3 without using too small value of a/W. In other words, if real K_{IC} is used, the crack length "a" should be determined from $K_I\big|_{r=a} \ge K_{IC}$. Real K_{IC} may be necessary for evaluating

different singular index problems in Fig. 3.7.

Table 3.12 Results of estimated adhesive tensile strength σ_c.

(a) Medium carbon steel S35C, Epoxy resin A

h/W	Experimental adhesive strength	Perfectly bonded model	Fictitious crack model	
			$a/W = 0.01$	$a/W = 0.1$
	σ_c [MPa]	σ_c [MPa] when $K_{\sigma c} = 1.04$ $\mathrm{MPa \cdot m^{0.315}}$ (Error %)	σ_c [MPa] when $K_{IC} = 0.446$ $\mathrm{MPa\sqrt{m}}$ (Error %)	σ_c [MPa] when $K_{IC} = 0.844$ $\mathrm{MPa\sqrt{m}}$ (Error %)
0.001	–	94.5	74.7	58.5
0.003	57.2	61.3 (+ 7.1%)	60.9 (+ 6.4%)	56.4 (− 1.4%)
0.007	53.3	49.5 (− 7.2%)	48.8 (− 8.4%)	49.2 (− 7.7%)
0.01	–	56.2	43.7	46.0
0.023	32.5	34.5 (+ 6.2%)	35.4 (+ 8.8%)	35.9 (+ 10.3%)
0.047	25.9	27.5 (+ 5.9%)	28.3 (+ 8.9%)	27.9 (+ 7.7%)
0.078	22.6	23.0 (+ 2.1%)	23.4 (+ 3.9%)	23.1 (+ 2.2%)
0.1	–	19.5	21.4	21.3
0.157	18.4	17.8 (− 3.0%)	17.7 (− 3.8%)	18.0 (− 2.3%)
0.394	13.4	12.3 (− 8.5%)	11.9 (− 11.4%)	12.6 (− 6.1%)
0.5	–	11.3	14.5	14.1

(b) Medium carbon steel S35C, Epoxy resin B

h/W	Experimental adhesive strength	Perfectly bonded model	Fictitious crack model	
			$a/W = 0.01$	$a/W = 0.1$
	σ_c [MPa]	σ_c [MPa] when $K_{\sigma c} = 1.20$ $\mathrm{MPa \cdot m^{0.326}}$ (Error %)	σ_c [MPa] when $K_{IC} = 0.551$ $\mathrm{MPa\sqrt{m}}$ (Error %)	σ_c [MPa] when $K_{IC} = 1.01$ $\mathrm{MPa\sqrt{m}}$ (Error %)
0.001	–	98.3	118.0	84.0
0.003	76.8	80.6 (+ 5.0%)	81.2 (+ 5.8%)	76.9 (+ 0.1%)
0.007	71.4	64.2 (− 10.1%)	64.1 (− 10.3%)	65.7 (− 8.1%)
0.01	–	76.4	58.0	61.2
0.023	49.7	44.5 (− 10.3%)	45.7 (− 8.0%)	46.1 (− 7.1%)
0.047	41.2	35.1 (− 14.7%)	36.0 (− 12.6%)	35.2 (− 14.4%)
0.079	25.3	29.3 (+ 15.5%)	29.5 (+ 16.4%)	28.8 (+ 13.5%)
0.1	–	23.4	25.9	25.9
0.157	19.7	22.4 (+ 13.5%)	21.8 (+ 10.9%)	22.1 (+ 12.4%)
0.394	13.4	15.1 (+ 11.0%)	14.3 (+ 5.4%)	15.2 (+ 11.4%)
0.5	–	17.4	12.9	14.1

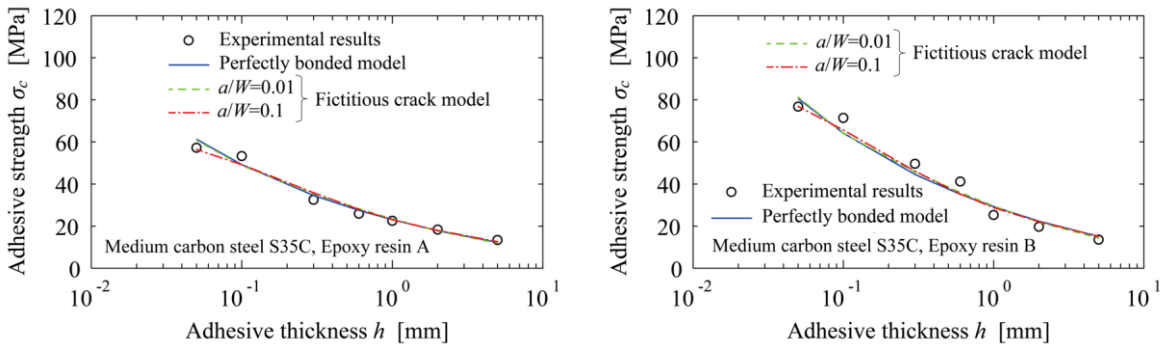

(a) (b)

Fig.3.23 Relationship between σ_c and h for bonded Medium carbon steel S35C. (a) Medium carbon steel S35C, Epoxy resin A, (b) Medium carbon steel S35C, Epoxy resin B.

3.4 Conclusion

In this study, several types of adhesive joints are considered in terms of the intensity of singular stress at the interface corner with and without fictitious crack. To evaluate the debonding strength conveniently and efficiently, the elastic and homogeneous adhesive layer is simply assumed without considering other defects and residual strain. The conclusions can be summarized in the following way.

1. The corner stress intensity factors K_σ can be obtained conveniently by using the analysis method presented. Then the adhesive strength σ_c for various butt joints can be evaluated as $K_{\sigma c}$=const for carbon steel/epoxy resin, aluminum/araldite, and brass/solder as shown in Figs. 3.3, 3.4. As well as the results of Suzuki for carbon steel/epoxy resin [22], whose specimens are carefully prepared to exclude the defect and residual strain, other experimental results can be expressed as the critical stress intensity factor $K_{\sigma c}$=const.
2. The interface intensity factors K_I and K_{II} can be obtained conveniently by using the analysis method presented. Then the adhesive strength σ_c for various butt

joints can be evaluated as K_{IC}=const assuming fictitious crack modeling as shown in Figs. 3.15 - 18.

3. The usefulness of the fictitious crack modeling was highlighted by taking an example of sharp V-notch problems. Although different notch opening angle has distinct singular index, the static strength of notched acrylic resin can be expressed as K_{IC}=const. The suitable fictitious crack length is found to be a = 0.02-0.16mm on the basis of the criterion when the fracture occurs at the crack tip as $K_I\big|_{r=a} \geq K_{IC}$.
4. The relationship between the critical value of interface stress intensity factor K_{IC} and critical value of corner stress intensity factor $K_{\sigma c}$ is considered. The relation $K_{IC} \propto a^{\lambda-0.5} K_{\sigma c}$ can be derived for the fictitious crack length $a/W \leq 0.01$ (see Figs. 3.21, 22).
5. The suitable dimension for fictitious crack was discussed for butt joints. The applicability should be confirmed in the further studies for other types of joint geometries.

3.5 References

[1] Yuuki R. Mechanics of interface. 1st ed. Baifuukann, Tokyo; 1992 [in Japanese].

[2] Hibino Y. Influence of types and surface treatment of dental alloy and film thickness of cements on bond strength of dental luting cements. J Jpn Soc Dent Mater Devices 1990; 9(6):786-805 [in Japanese].

[3] Asada B, Shinya A, Yokozuka S. Effect of dental adhesive film thickness on bond strength. Adhes Dent 1990;8:201–26 [in Japanese].

[4] Kagawa F, Yamada J, Suzuki T, Hisamitsu H, Wakumoto S. The relationship between film thickness of resin luting cements and bond strength, the influence of thermal stress. Jpn J Conserv Dent 1991;34(2):392–8 [in Japanese].

[5] Naito K, Onta M, Kogo Y. The effect of adhesive thickness on tensile and shear strength of polyimide adhesive. Int J Adhes Adhes 2012;36:77–85.

[6] Liu ZX, Huang YA, Yin ZP, Bennati S, Valvo PS. A general solution for the two-dimensional stress analysis of balanced and unbalanced adhesively bonded joints. Int J Adhes Adhes 2014;54:112–23.

[7] Uddin MA, Ali MY, Chan HP. Achieving optimum adhesion of conductive adhesive bonded flip-chip on flex packages. Rev Adv Mater Sci 2009;21 (2):165–72.

[8] Huang Z, Kumar P, Dutta I, Pang JHL, Sidhu R. A general methodology for calculating mixed mode stress intensity factors and fracture toughness of solder joints with interfacial cracks. Eng Fract Mech 2014;131:9–25.

[9] Kitasako Y, Burrow MF, Nikaido T, Harada N, Inokoshi S, Yamada T, Takatsu T. Shear and tensile bond testing for resin cement evaluation. Dent Mater 1995;11(5–6):298–304.

[10] Yasuda M. Hitachi Technical Report 40. 2003. p. 7–12.

[11] Shibutani T. Evaluation of crack initiation at interfacial edge on the basis of fracture mechanics concept and application to electronics devices (Tutorial Series: Foundations for reliability analysis). J Jpn Inst Electron Packag 2004;7 (7):639–44 [in Japanese].

[12] Hattori T, Sakata S, Hatsuda T, Murakami G. A stress singularity parameter approach for evaluating adhesive strength. JSME Int J Ser 1 Solid Mech Strength Mater 1988;31(4):718–23.

[13] Shiratori M. Problems of joints in packaging of electronic devices. Trans Jpn Soc Mech Eng A 1994;60(577):1905–12 [in Japanese].

[14] Di Pisa C, Aliabadi MH. An efficient BEM formulation for analysis of bond-line cracks in thin walled aircraft structures. Int J Fract 2013;179(1-2):129–45.

[15] Hasebe N, Kato S. Solution of problem of two dissimilar materials bonded at one interface subjected to temperature. Arch Appl Mech 2014;84(6):913–31.

[16] Krishnan A, Roy Xu L. An experimental study on the crack initiation from notches connected to interfaces of bonded bi-materials. Eng Fract Mech 2013;111:65–76.

[17] Ikegami K, Kajiyama M, Kamiko S, Shiratori E. Experimental studies of the strength of an adhesive joint in a state of combined stress. J Adhes 1979;10 (1):25–38.

[18] Yamato T, Shirahama M, Hara S. Effect of adhesive thickness on the strength of chlorinated rubber adhesive. J Soc Rubber Sci Technol 1957;30(11):842–7 [in Japanese].

[19] Yokoyama T, Nakai K, Ikeda T. Effect of specimen geometry on tensile properties of structual adhesive butt joints. In: JSME annual meeting; 2006. p. 861–2 [in Japanese].

[20] Akinmade A O, Nicholson J W. Effect of adhesive layer thickness on the bond strength of a zinc polycarboxylate dental cement. Biomaterials 1995; 16(2):149-54.

[21] Till Vallée, João R. Correia, Thomas Keller. Optimum thickness of joints made of GFPR pultruded adherends and polyurethane adhesive. Compos Struct 2010;92(9):2102–8.

[22] Suzuki Y. Adhesive tensile strengths of scarf and butt joints of steel plates (Relation between adhesive layer thicknesses and adhesive strengths of joints). JSME IntJ 1987;30(265):1042–51.

[23] Zhang Y, Noda NA, Takaishi K, Lan X. Effect of adhesive thickness on the intensity of singular stress at the adhesive dissimilar joint. J Solid Mech Mater Eng 2010;4(10):1467–79.

[24] Noda NA, Zhang Y, Lan X, Takase Y, Oda K. Stress intensity factors of an interface crack in a bonded plate under uni-axial tension. J Solid Mech Mater Eng 2010;4(7):974–87.

[25] Lan X, Noda NA, Michinaka K, Zhang Y. The effect of material combinations and relative crack size on the stress intensity factors at the crack tip of a bi-material bonded strip. Eng Fract Mech 2011;78(14):2572–84.

[26] Noda NA, Lan X. Stress intensity factors for an edge interface crack in a bonded semi-infinite plate for arbitrary material combination. Int J Solids Struct 2012;49(10):1241–51.

[27] Zhang Y, Noda NA, Takaishi K, Lan X. Stress intensity factors of a central interface crack in a bonded finite plate and periodic interface cracks under arbitrary material combinations. Eng Fract Mech 2011;78(6):1218–32.

[28] Zhang Y. Intensity of singular stress field at the end of interface under arbitrary material combination. Japan: Kyushu Institute of Technology; 2011 Ph.D. dissertation.

[29] Zhang Y, Noda NA, Wu PZ, Duan ML. A mesh-independent technique to evaluate stress singularities in adhesive joints. Int J Adhes Adhes 2015;57:105– 17 the corrigendum of authorship is published in Int J Adhes Adhes 60, 2015.

[30] Noda NA, Oda K. Interaction effect of stress intensity factors for any number of collinear interface cracks. Int J Fract 1997;84:117–28.

[31] Bogy DB. Edge-bonded dissimilar orthogonal elastic wedges under normal and shear loading. Trans ASME J Appl Mech 1968;35(3):460–6.

[32] Bogy DB. Two edge-bonded elastic wedges of different materials and wedge angles under surface tractions. Trans ASME J Appl Mech 1971;38(2):377–86.

[33] Noda NA, Shirao R, Li J, Sugimoto JS. Intensity of singular stress fields causing interfacial debonding at the end of a fiber under pullout force and transverse tension. Int J Solids Struct 2007;44:4472–91.

[34] Inoue S. Mechanics of adhesion. Kobunshi 1956; 5(12):583–7. [in Japanese]

[35] Akisanya AR, Meng CS. Initiation of fracture at the interface corner of bi-material joints. J Mech Phys Solids 2003;51(1):27–46.

[36] Qian Z, Akisanya AR. An experimental investigation of failure initiation in bonded joints. Acta Mater 1998;46(14):4895–904.

[37] Mintzas A, Nowell D. Validation of an H_{cr}-based fracture initiation criterion for adhesively bonded joints. Eng Fract Mech 2012;80:13–27.

[38] Chen DH, Nisitani H. Singular stress fields near a corner of jointed dissimilar materials. Trans Jpn Soc Mech Eng A 1991;57(542):2509–15 [in Japanese].

[39] Chen DH, Noda NA, Takase Y, Morodomi T. Evaluation of static strength by the application of stress intensity of angular corner. Trans Jpn Soc Mech Eng A 1996;62(598):1445–9 [in Japanese].

[40] Chen DH, Noda NA. A consideration on the fracture criterion for a sharp notch. Trans Jpn Soc Mech Eng A 1998;64(626):2574–82 [in Japanese].

[41] Shimoda Y, Oda K, Tsutsumi N. Evaluation of singular field for V-shaped notch specimen by small crack concept. In: Proceedings of ACMFMS 2014 mechanics of functional materials and structures; 2014. p. 593–4.

[42] Oda K, Kamisugi K, Noda NA. Analysis of stress intensity factor for interface cracks based on proportional method. Trans Jpn Soc Mech Eng A 2009;75 (752):476–82 [in Japanese].

[43] Oda K, Noda NA, Atluri SN. Accurate determination of stress intensity factor for interface crack by finite element method. Key Eng Mater 2007;353- 358:3124–7.

[44] Oda K, Lan X, Noda N, Michinaka K. Effect of arbitrary bi-material combination and bending loading conditions on stress intensity factors of an edge interface crack. International Journal of Structural Integrity 2012; 3(4): 457-475.

[45] Terasaki T, Akiyama T, Kaneko T, Hisada H. Proposal of implant type torsion test for estimating adhesive strength of sprayed coatings. Q J Jpn Weld Soc 1991;9(4):97–103 [in Japanese].

[46] Terasaki T, Akiyama T, Kamiwaki S. Study of interfacial strength of bonded dissimilar materials. Q J Jpn Weld Soc 1992;10(2):83–8 [in Japanese].

[47] Chen DH, Nisitani H. Stress intensity factors K_{I,λ_1} and K_{II,λ_2} of a strip with a V-Shaped single notch under tension or in-plane bending. Trans Jpn Soc Mech Eng A 1993;59(560):1069–74 [in Japanese].

[48] Chen DH, Nisitani H. Singular stress fields near the tip of a V-notch in a semi-finite plate. Trans Jpn Soc Mech Eng A 1991;57(538):1406–11.

[49] Noda NA, Oda K, Inoue T. Analysis of newly-defined stress intensity factors for angular corners using singular integral equations of the body force method. Int J Fract 1996;76:243–61.

[50] Chen DH. Stress intensity factors for V-notched strip under tension or in-plane bending. Int J Fract 1995;70:81–97.

[51] Noda NA, Takase Y. Generalized stress intensity factors of V-shaped notch in a round bar under torsion, tension, and bending. Eng Fract Mech 2003;70:1447– 66.

Chapter 4 Convenient analysis method for the intensity of singular stress field (ISSF) of lap joint

4.1 Introduction

Adhesively bonded joints are economical, practical and easy to make; thus they have been widely used in a variety of industries. The single-lap shear testing [1-3] is general popular testing method widely used. However, the debonding strength is affected by the specimen dimension and difficult to be applied to other geometries. Compared with double lap joint, single lap joint can be used conveniently. However, the shear strength of double lap joint is nearly twice larger than the one of single lap joint. Therefore, it is necessary to find a suitable evaluation method for single lap joint testing. The single lap joint testing should be done under pure shear loading, but pure shear testing is difficult to be realized in the experiment. Due to the bend deformation of single lap joint during testing, the peeling force is applied to the adhesive region. Then the intensity of singular stress field (ISSF) at the interface corner is affected by the peeling force due to the deformation. Therefore, it is necessary to find a suitable evaluation method to minimize the ISSF for single lap joint. To minimize the ISSF for single lap joint, a practical and convenient analysis method for the ISSF of lap joint is required first.

Recently, Mintzas and Nowell [4] investigated the ISSF for double lap joint by using William's eigenfunction expansion method in combination with a path independent contour integral method[5-10]. However, since the contour integral method requires the complex and difficult calculations such as matrix operation and numerical

integration, it is difficult to be widely used and may bring low practicality. Therefore, an effective and convenient analysis method for lap joint is expected.

In the last chapter, since the ISSF of butt joint can be obatined conveniently by using the analysis method presented in previous studies, the debonding strength of butt joint is investigetaed in terms of the ISSF, and it is found the adhesive butt joint strength in Fig. 4.1 can be expressed as a critical value of ISSF $K_{\sigma c}$=const by using a mesh independent calculation technique [11, 12]. However, since the singular stress field of lap joint is complex than butt joint, the method for butt joint cannot be applied to the lap joint analysis directly. Therefore, in this chapter, a convenient analysis method for lap joint will be proposed. The single lap joint specimen as shown in Fig.4.2 [13] will be used as an example to evaluate the analysis method.

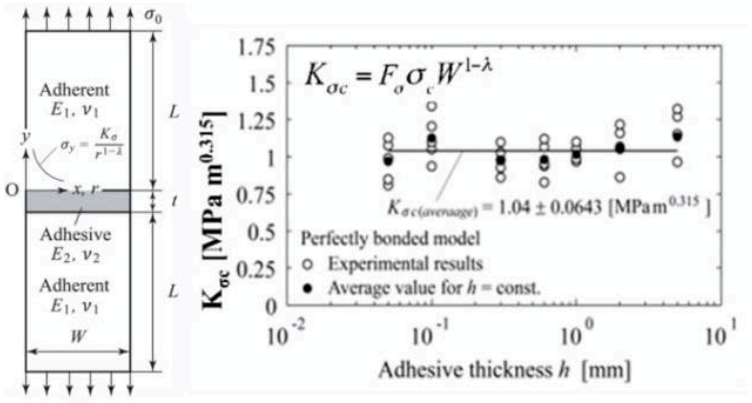

Fig.4.1 Adhesive strength expressed as $K_{\sigma c}$=const for butt joint.

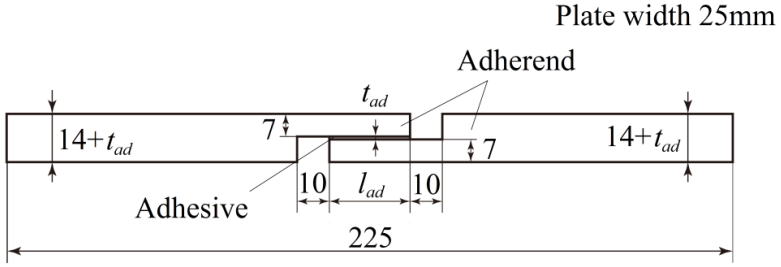

Fig.4.2 Specimen configurations.

4.2 Analysis method for lap joints focusing on the distinct singular stress field

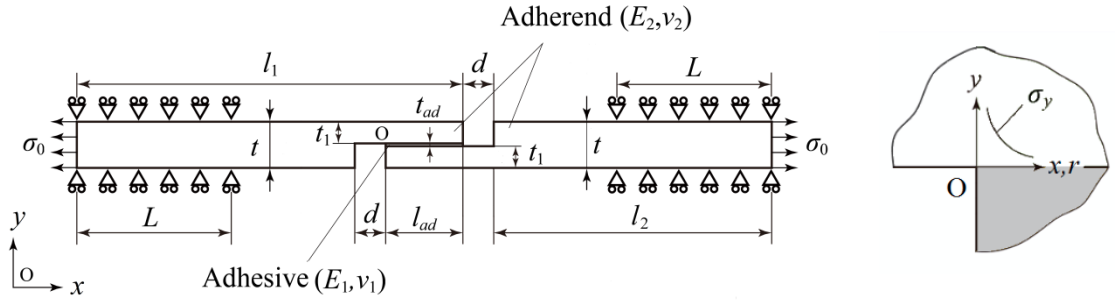

Fig.4. 3 Analysis model and boundary condition.

As shown in chapter 3, the ISSF for butt joints can be obtained conveniently because of only one real root in Eq.(3.2) and the exact reference solution K_σ^* available for bonded plate [14]. However, the lap joints have a distinct singular stress field at the interface corner [15]. In this chapter, the single lap joint in Fig.4.3 will be considered as an example to evaluate the analysis method of lap joints. The value of the singular index λ can be determined from the eigenequation (4.1), which was derived by Bogy [16, 17].

$$\begin{aligned}&4\sin^2(\pi\lambda)\left\{\sin^2\left(\frac{\pi\lambda}{2}\right)-\lambda^2\right\}\beta^2+4\lambda^2\sin^2(\pi\lambda)\alpha\beta+\left\{\sin^2\left(\frac{\pi\lambda}{2}\right)-\lambda^2\right\}\alpha^2-4\lambda^2\sin^2(\pi\lambda)\beta\\&-2\left\{\lambda^2\cos(2\pi\lambda)+\sin^2\left(\frac{\pi\lambda}{2}\right)\cos(\pi\lambda)+\frac{1}{2}\sin^2(\pi\lambda)\right\}\alpha+\sin^2\left(\frac{3\pi}{2}\lambda\right)-\lambda^2=0\end{aligned}\quad (4.1)$$

Here, α and β are Dundurs' parameters [18], which are expressed by Possion's ratio ν and shear modulus G ($_j$=1 is for adhesive, $_j$=2 is for adherend).

$$\alpha=\frac{G_1(\kappa_2+1)-G_2(\kappa_1+1)}{G_1(\kappa_2+1)+G_2(\kappa_1+1)},\ \beta=\frac{G_1(\kappa_2-1)-G_2(\kappa_1-1)}{G_1(\kappa_2+1)+G_2(\kappa_1+1)},\ \kappa_j=\begin{cases}\dfrac{3-\nu_j}{1+\nu_j} & (\text{plane stress})\\ 3-4\nu_j & (\text{plane strain})\end{cases}\quad (j=1,2)\quad (4.2)$$

The lap joint has two real roots in most of material combination as shown in Appendix C.

The adhesive strength testing of single lap joint is standardized by Japanese Industrial Standards (JIS K6850) [3]. This standard prescribes the specimens with a

small thickness 1.6 ± 0.1 mm. Since large deformations usually appear before debonding for thin specimen, the thick specimens used by Park [13] in Fig. 4.2 will be analyzed in this study, where the adherends aluminum alloy 6061-T6 are bonded with adhesive FM73M epoxy. Table 4.1 shows the elastic parameters of the adherend and adhesive. The egenequation of λ has two different real roots, that is, λ_1=0.6062 and λ_2=0.9989. Then, the stresses σ_y and τ_{xy} can be expressed as follows.

$$\sigma_y = \frac{K_{\sigma,\lambda_1}}{r^{1-\lambda_1}} + \frac{K_{\sigma,\lambda_2}}{r^{1-\lambda_2}}, \quad \tau_{xy} = \frac{K_{\tau,\lambda_1}}{r^{1-\lambda_1}} + \frac{K_{\tau,\lambda_2}}{r^{1-\lambda_2}}. \tag{4.3}$$

Table 4.1 Material properties of adhesive and adherend.

Material		Young's modulus E [GPa]	Poisson's ratio ν	α	β	λ_1	λ_2
Adherent	6061-T6	68.9	0.30	-0.8699	-0.06642	0.6062	0.9989
Adhesive	Epoxy resin	4.20	0.45				

As shown in Eq. (4.3), the singular stress field of lap joint is complex and therefore the analysis is more difficult than the analysis of the butt joint. Since the method in chapter 3 cannot be applied to the lap joint analysis directly, the singular stress field for the lap joint will be investigated.

Since the two-dimensional model is confirmed to be good enough for the strength evaluation, in this study, two-dimensional FEM model is considered. Fig. 4.3 shows the analysis model where l_1 and t_1 are the adherend length and adherend thickness, l_{ad} and t_{ad} are the adhesive length and adhesive thickness, L is the fixed boundary length of adherend, and σ_o is the tension at both ends of single lap joint. In addition, (E_1, ν_1) and (E_2, ν_2) are Young's modulus and Poisson's ratio of the adhesive and adherend, respectively. The total length of the specimen in Fig. 4.3 is fixed as 225mm with varying the adhesive thickness t_{ad}=0.15~0.9mm and the adhesive length l_{ad} =10~50mm. Table 4.2 shows the dimensions of the specimens considered in this study.

Table 4.2 Dimensions of the adhesive joint specimens

Specimen	l_{ad} [mm]	t_{ad} [mm]
A10	10	0.15
A15	15	0.15
A20	20	0.15
A25	25	0.15
A30	30	0.15
A35	35	0.15
A40	40	0.15
A50	50	0.15
A25-30	25	0.30
A25-45	25	0.45
A25-90	25	0.90
A30-30	30	0.30
A30-45	30	0.45
A30-90	30	0.90

Fig. 4.4 shows the schematic illustration of the mesh pattern in the vicinity of the interface corner of lap joint. The linear elastic analyses are performed under the plane strain condition by using the software MSC Marc. In this analysis, the elements near the edge corners of all models are set so as to be the same size and shape around the corner independent of the adhesive dimensions. Then, the minimum size of the element around the corner $e_{\min}$ is changed, the effect of the mesh pattern on the stress distribution is investigated. The value of $e_{\min}$ is set to 3^{-8}mm, 3^{-9}mm, 3^{-10}mm and 3^{-11}mm.

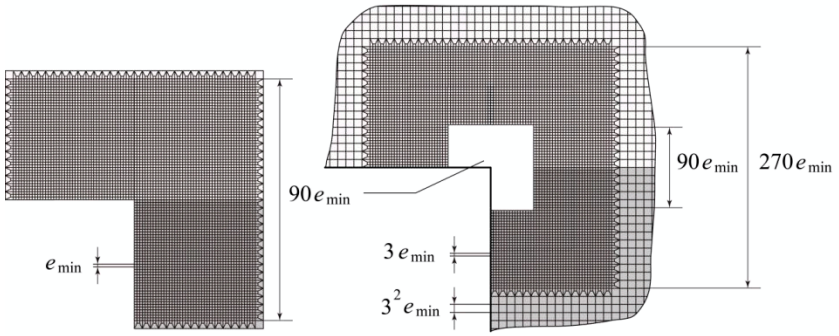

Fig.4.4 Mesh pattern near the interface edge.

Table 4.3 shows the singular stress distributions obtained by FEM stress $\sigma_{y,\mathrm{FEM}}$, $\tau_{y,\mathrm{FEM}}$ for the specimens A25, A50, A25-90 under the applied stress $\sigma_0 = 1\,\mathrm{MPa}$. Based on the fixed boundary length prescribed in JIS K6850 [3], L=50mm is fixed in this study. It is found that the stress ratios become almost constant independent of $e_{\min}$. Fig. 4.5 shows the normalized stress distribution $\sigma_{y,\mathrm{FEM}}^{\mathrm{A50}} / \sigma_{y,\mathrm{FEM}}^{\mathrm{A25}}$, $\tau_{xy,\mathrm{FEM}}^{\mathrm{A50}} / \tau_{xy,\mathrm{FEM}}^{\mathrm{A25}}$ under the applied stress σ_0 =1MPa. Fig. 4.6 shows the normalized stress distributions $\sigma_{y,\mathrm{FEM}}^{\mathrm{A25-90}} / \sigma_{y,\mathrm{FEM}}^{\mathrm{A25}}$, $\tau_{xy,\mathrm{FEM}}^{\mathrm{A25\text{-}90}} / \tau_{xy,\mathrm{FEM}}^{\mathrm{A25}}$ under the applied stress σ_0 =1MPa. The stress distributions of the specimen A25-90 are different from those of the specimen A50. That is because the bending moment which is applied to the adhesive layer changes depending on the adhesive thickness. However, when the $r < 10^{-4}$ mm, $\sigma_{y0,\mathrm{FEM}}^{\mathrm{A25\text{-}90}} / \sigma_{y0,\mathrm{FEM}}^{\mathrm{A25}}$ and $\tau_{xy,\mathrm{FEM}}^{\mathrm{A25-90}} / \tau_{xy,\mathrm{FEM}}^{\mathrm{A25}}$ become almost constant.

Table 4.3 Stress distributions on the interface of specimens A25, A50 and A25-90 when $\sigma_0 = 1\,\mathrm{MPa}$

(a) $e_{\min} = 3^{-8}$ mm

	A25		A50		A25-90					
r [mm]	$\sigma_{y,\mathrm{FEM}}^{\mathrm{A25}}$ [MPa]	$\tau_{y,\mathrm{FEM}}^{\mathrm{A25}}$ [MPa]	$\sigma_{y,\mathrm{FEM}}^{\mathrm{A50}}$ [MPa]	$\tau_{y,\mathrm{FEM}}^{\mathrm{A50}}$ [MPa]	$\sigma_{y,\mathrm{FEM}}^{\mathrm{A25-90}}$ [MPa]	$\tau_{y,\mathrm{FEM}}^{\mathrm{A25-90}}$ [MPa]	$\frac{\sigma_{y,\mathrm{FEM}}^{\mathrm{A50}}}{\sigma_{y,\mathrm{FEM}}^{\mathrm{A25}}}$	$\frac{\tau_{xy,\mathrm{FEM}}^{\mathrm{A50}}}{\tau_{xy,\mathrm{FEM}}^{\mathrm{A25}}}$	$\frac{\sigma_{y,\mathrm{FEM}}^{\mathrm{A25-90}}}{\sigma_{y,\mathrm{FEM}}^{\mathrm{A25}}}$	$\frac{\tau_{xy,\mathrm{FEM}}^{\mathrm{A25-90}}}{\tau_{xy,\mathrm{FEM}}^{\mathrm{A25}}}$
$0/3^8$	108.089	-34.3491	82.2182	-26.1290	108.513	-34.4831	0.760653	0.760690	1.00392	1.00390
$1/3^8$	60.9108	-17.5542	46.3257	-13.3538	61.1477	-17.6315	0.760550	0.760718	1.00389	1.00440
$2/3^8$	45.8040	-14.9598	34.8342	-11.3807	45.9878	-15.0364	0.760506	0.760752	1.00401	1.00512
$3/3^8$	36.3691	-13.4622	27.6575	-10.2414	36.5270	-13.5417	0.760467	0.760752	1.00434	1.00591
$4/3^8$	31.0483	-12.2658	23.6104	-9.33110	31.1985	-12.3473	0.760441	0.760741	1.00484	1.00664
$5/3^8$	27.6319	-11.3873	21.0119	-8.66264	27.7833	-11.4705	0.760422	0.760728	1.00548	1.00731
$6/3^8$	25.2208	-10.6877	19.1718	-8.13018	25.3777	-10.7719	0.760158	0.760704	1.00622	1.00788

(b) $e_{\min} = 3^{-11}$ mm

r [mm]	A25 $\sigma_{y,\mathrm{FEM}}^{\mathrm{A25}}$ [MPa]	A25 $\tau_{y,\mathrm{FEM}}^{\mathrm{A25}}$ [MPa]	A50 $\sigma_{y,\mathrm{FEM}}^{\mathrm{A50}}$ [MPa]	A50 $\tau_{y,\mathrm{FEM}}^{\mathrm{A50}}$ [MPa]	A25-90 $\sigma_{y,\mathrm{FEM}}^{\mathrm{A25-90}}$ [MPa]	A25-90 $\tau_{y,\mathrm{FEM}}^{\mathrm{A25-90}}$ [MPa]	$\frac{\sigma_{y,\mathrm{FEM}}^{\mathrm{A50}}}{\sigma_{y,\mathrm{FEM}}^{\mathrm{A25}}}$	$\frac{\tau_{xy,\mathrm{FEM}}^{\mathrm{A50}}}{\tau_{xy,\mathrm{FEM}}^{\mathrm{A25}}}$	$\frac{\sigma_{y,\mathrm{FEM}}^{\mathrm{A25-90}}}{\sigma_{y,\mathrm{FEM}}^{\mathrm{A25}}}$	$\frac{\tau_{xy,\mathrm{FEM}}^{\mathrm{A25-90}}}{\tau_{xy,\mathrm{FEM}}^{\mathrm{A25}}}$
$0/3^{11}$	396.766	-125.975	301.826	-95.8324	398.250	-126.441	0.760715	0.760726	1.00374	1.00370
$1/3^{11}$	224.377	-64.3886	170.680	-48.9821	225.258	-64.6264	0.760684	0.760726	1.00393	1.00369
$2/3^{11}$	169.059	-54.8550	128.597	-41.7302	169.735	-55.0544	0.760663	0.760736	1.00400	1.00364
$3/3^{11}$	134.534	-49.3942	102.333	-37.5760	135.084	-49.5722	0.760648	0.760737	1.00409	1.00360
$4/3^{11}$	115.084	-45.0352	87.5367	-34.2601	115.560	-45.1967	0.760633	0.760740	1.00414	1.00359
$5/3^{11}$	102.616	-41.8377	78.0522	-31.8277	103.046	-41.9899	0.760624	0.760742	1.00419	1.00364
$6/3^{11}$	93.8343	-39.2910	71.3715	-29.8904	94.2297	-39.4337	0.760612	0.760744	1.00421	1.00363

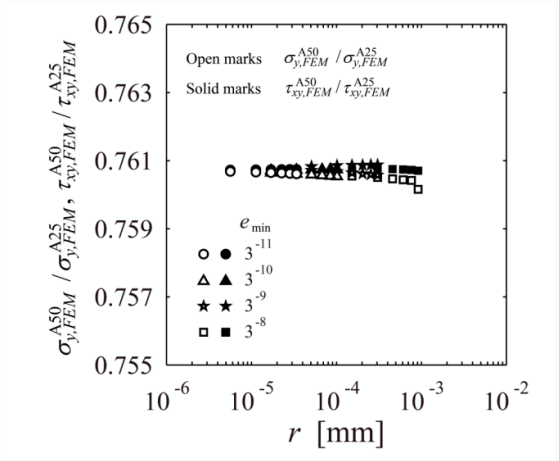

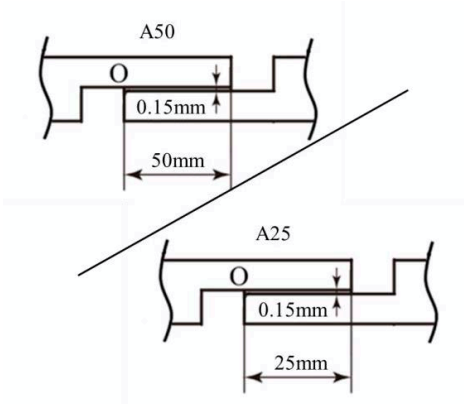

Fig.4.5 Normalized stress distributions $\sigma_{y,\mathrm{FEM}}^{\mathrm{A50}} / \sigma_{y,\mathrm{FEM}}^{\mathrm{A25}}$, $\tau_{xy,\mathrm{FEM}}^{\mathrm{A50}} / \tau_{xy,\mathrm{FEM}}^{\mathrm{A25}}$ under $\sigma_0 = 1$ MPa.

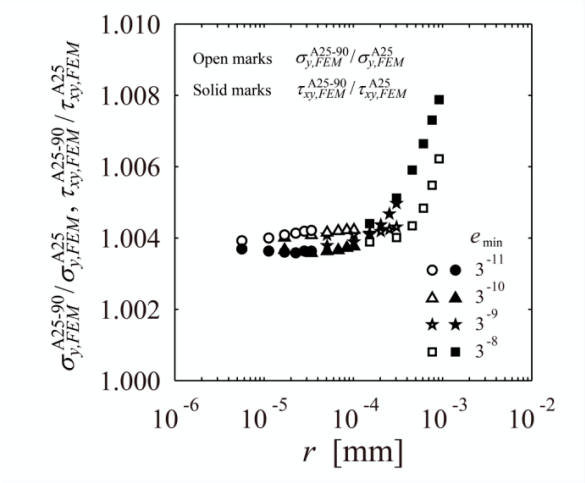

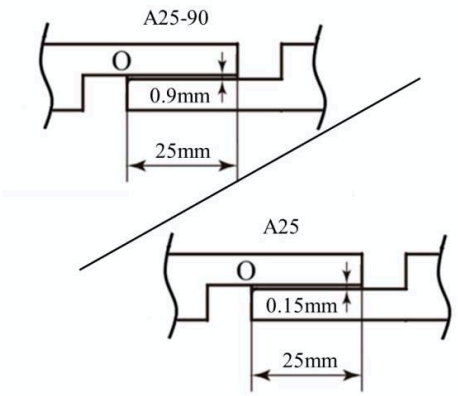

Fig.4.6 Normalized stress distributions $\sigma_{y,\mathrm{FEM}}^{\mathrm{A25-90}} / \sigma_{y,\mathrm{FEM}}^{\mathrm{A25}}$, $\tau_{xy,\mathrm{FEM}}^{\mathrm{A25-90}} / \tau_{xy,\mathrm{FEM}}^{\mathrm{A25}}$ under $\sigma_0 = 1$ MPa.

From the results of Table 4.4 and Figs. 4.5, 4.6, it is found that the stress ratios at the edge corner become almost constant independent of $e_{\min}$, t_{ad} and l_{ad}. Therefore, the following relations can be conjectured at the edge corner.

$$\sigma_y = \frac{K_{\sigma,\lambda_1}}{r^{1-\lambda_1}} + \frac{K_{\sigma,\lambda_2}}{r^{1-\lambda_2}} \cong K_{\sigma,\lambda_1}\left(\frac{1}{r^{1-\lambda_1}} + \frac{C_\sigma}{r^{1-\lambda_2}}\right), \tag{4.4}$$

$$\tau_{xy} = \frac{K_{\tau,\lambda_1}}{r^{1-\lambda_1}} + \frac{K_{\tau,\lambda_2}}{r^{1-\lambda_2}} \cong K_{\tau,\lambda_1}\left(\frac{1}{r^{1-\lambda_1}} + \frac{C_\tau}{r^{1-\lambda_2}}\right) \tag{4.5}$$

Since the normalized stress is independent of the mesh size and the geometry of the adhesive joint, constant values C_σ and C_τ in Eqs. (4.4), (4.5) can be assumed. The validity of this assumption will be confirmed in the next Chapter. Here, the reference solution is denoted by K^*_{σ,λ_1} and the unknown solution is denoted by K_{σ,λ_1}. Then, the FEM stresses obtained at the corner point are denoted by $\sigma^*_{y0,\mathrm{FEM}}$ for the reference solution and $\sigma_{y0,\mathrm{FEM}}$ for unknown problem. From Eq.(4.4), the relation between $K_{\sigma,\lambda_1}/K^*_{\sigma,\lambda_1}$ and $\sigma_{y0,\mathrm{FEM}}/\sigma^*_{y0,\mathrm{FEM}}$ can be expressed as follows.

$$\frac{K_{\sigma,\lambda_1}}{K^*_{\sigma,\lambda_1}} = \frac{\sigma_{y0,\mathrm{FEM}}}{\sigma^*_{y0,\mathrm{FEM}}} \tag{4.6}$$

If K^*_{σ,λ_1} is available, K_{σ,λ_1} can be obtained from the EFM stress ratio by applying the same mesh pattern to the reference problem. Similarly, K_{τ,λ_1} can be obtained from the FEM shear stress ratio (see Eq.(4.7)).

$$\frac{K_{\tau,\lambda_1}}{K^*_{\tau,\lambda_1}} = \frac{\tau_{xy0,\mathrm{FEM}}}{\tau^*_{xy0,\mathrm{FEM}}} \tag{4.7}$$

As shown in Fig. 4.5, it is found that the different between $\sigma^{\mathrm{A50}}_{y0,\mathrm{FEM}}/\sigma^{\mathrm{A25}}_{y0,\mathrm{FEM}}$ and $\tau^{\mathrm{A50}}_{xy0,\mathrm{FEM}}/\tau^{\mathrm{A25}}_{xy0,\mathrm{FEM}}$ tends to become small with the *r* decreasing. Then, from Fig. 4.6, the different between $\sigma^{\mathrm{A25\text{-}90}}_{y0,\mathrm{FEM}}/\sigma^{\mathrm{A25}}_{y0,\mathrm{FEM}}$ and $\tau^{\mathrm{A25\text{-}90}}_{xy0,\mathrm{FEM}}/\tau^{\mathrm{A25}}_{xy0,\mathrm{FEM}}$ tends to become small with the *r* decreasing. From Table 4.4, the relations of $\sigma^{\mathrm{A50}}_{y0,\mathrm{FEM}}/\sigma^{\mathrm{A25}}_{y0,\mathrm{FEM}} = \tau^{\mathrm{A50}}_{xy0,\mathrm{FEM}}/\tau^{\mathrm{A25}}_{xy0,\mathrm{FEM}}$ and $\sigma^{\mathrm{A25\text{-}90}}_{y0,\mathrm{FEM}}/\sigma^{\mathrm{A25}}_{y0,\mathrm{FEM}} = \tau^{\mathrm{A25\text{-}90}}_{xy0,FEM}/\tau^{\mathrm{A25}}_{xy0,FEM}$ can be confirmed. This means

$\sigma_{y0,\mathrm{FEM}} / \sigma^*_{y0,\mathrm{FEM}} = \tau_{xy0,\mathrm{FEM}} / \tau^*_{xy0,\mathrm{FEM}}$, that is, following equation.

$$\frac{K_{\sigma,\lambda_1}}{K^*_{\sigma,\lambda_1}} = \frac{K_{\tau,\lambda_1}}{K^*_{\tau,\lambda_1}} \tag{4.8}$$

Regarding Eqs.(4.6)~ (4.8), similar equations can be obtained for K_{σ,λ_2} and K_{τ,λ_2}. This is because C_σ and C_τ are constant. Since the weaker singular index is close to no singularity as λ_2=0.9989 $\approx$1, considering the stronger singular stress field with λ_1 is enough. Table 4.4 shows the singular indexes λ_1, λ_2 of some other material combinations in [12] including stainless steel SUS304, aluminum alloy A7075, silicon and IC substrate FR-4.5 as the adherends with resin as the adhesive. It is found that the weaker singular indexes λ_2 is in the small range of 0.9914~0.9999.

Table 4.4 Singular indexes for single lap joint with different material combinations

	Material	Young's modulus E [GPa]	Poisson's ratio ν	λ_1	λ_2
Adherent	SUS304(stainless steel)	206	0.3	0.6568	0.9999
	A7075(aluminum alloys)	71	0.33	0.6489	0.9995
	Silicon	166	0.26	0.6552	0.9999
	FR-4.5(IC substrate)	15.34	0.15	0.6020	0.9914
Adhesive	Resin	2.74	0.38		

Fig.4.7 shows the results of λ_2 under arbitrarily material combination. In this figure, the open circles (○) denote the results of λ_2 used in previous experimental studies where the resin is used as the adhesive. The results show that λ_2=0.99-1. Therefore, just consider $\lambda_2 \approx 1$ is enough for the strength evaluation.

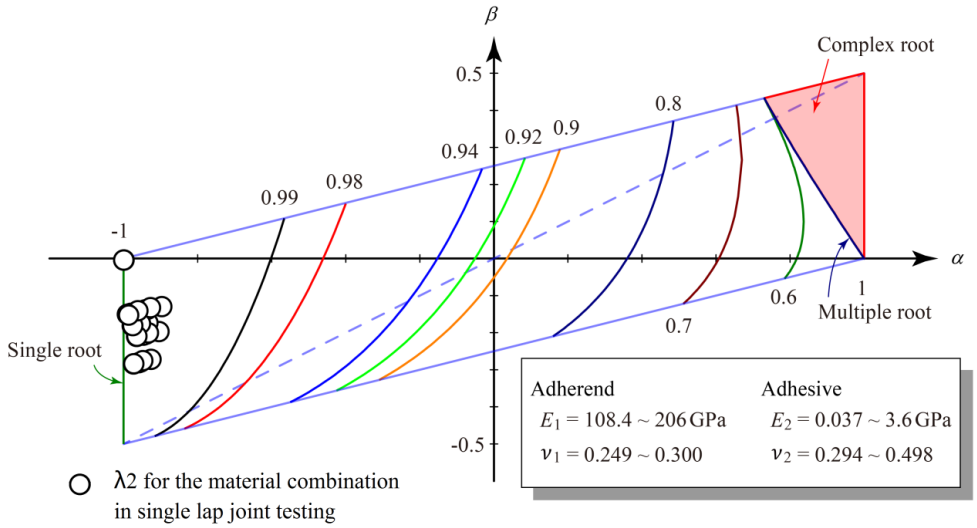

Fig.4.7 The results of λ_2 for all (α, β).

4.3 Discussion for evaluating the singular stress field of lap joints

In chapter 4.2, a convenient evaluation method was presented to obtain the ISSF of single lap joint. It was found that the singular stress field is expressed similarly independent of the geometry of the adhesive joint. However, only the normalized singular stress field can be discussed by using this method from Eqs. (4.6~4.8). The ISSF cannot be obtained since there is no exact reference solution for the lap joint. In this chapter, therefore, the reference solution will be obtained by using the reciprocal work contour integral method (RWCIM) [19] , and the usefuless of the proposed method in chapter 4.2 will be clarified by comparing the results of RWCIM. The detail of this method is indicated in Appendix D.

Around interface corner O in Fig. 4.3, the stresses σ_θ and $\tau_{r\theta}$ in the r direction can be expressed as follows. The notation r denotes the radial distance away from the corner singular point O.

$$\sigma_\theta = \frac{K_1}{r^{1-\lambda_1}} f_{\theta\theta}(\theta,\lambda_1) + \frac{K_2}{r^{1-\lambda_2}} f_{\theta\theta}(\theta,\lambda_2),$$
$$\tau_{r\theta} = \frac{K_1}{r^{1-\lambda_1}} f_{r\theta}(\theta,\lambda_1) + \frac{K_2}{r^{1-\lambda_2}} f_{r\theta}(\theta,\lambda_2). \quad (4.9)$$

Here, K_k （ $k=1,2$ ） has real values, the $f_{\theta\theta}(\theta,\lambda_k)$ and $f_{r\theta}(\theta,\lambda_k)$ are non-dimensional functions of angle θ and λ_k. Three boundaries exist in a biomaterial open wedge such as the one shown in Fig. 4.3, two traction free edges (at angles $\theta=-\pi/2$ and $\theta=\pi$) and an interface ($\theta=0$). By focusing on the interface stress, the intensity of singular stress fields are controlled by the following four parameters.

$$K_1 f_{\theta\theta}(\theta,\lambda_1)\big|_{\theta=0} = K_{\sigma,\lambda_1},\ K_2 f_{\theta\theta}(\theta,\lambda_2)\big|_{\theta=0} = K_{\sigma,\lambda_2},$$
$$K_1 f_{r\theta}(\theta,\lambda_1)\big|_{\theta=0} = K_{\tau,\lambda_1},\ K_2 f_{r\theta}(\theta,\lambda_2)\big|_{\theta=0} = K_{\tau,\lambda_2}. \quad (4.10)$$

As shown in Eq.(4.10), since the four parameters K_{σ,λ_1}, K_{σ,λ_2}, K_{τ,λ_1}, K_{τ,λ_2} are determined from K_1 and K_2, the singular stress field is also determined by the two real parameters.

Fig. 4.8 shows the integral path for RWCIM. The linear elastic analyses are performed under the plane strain condition by using the software MSC Marc. Fig. 4.9 shows the schematic illustration of the mesh pattern in the present analyses. Here, 8-node elements are used in the vicinity of the interface corner edge, 4-node elements are used in other regions.

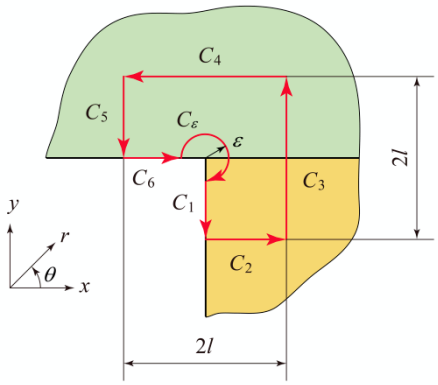

Fig.4.8 Integral path C for RWCIM ($C = C_1 + C_2 + C_3 + C_4 + C_5 + C_6 + C_\varepsilon$).

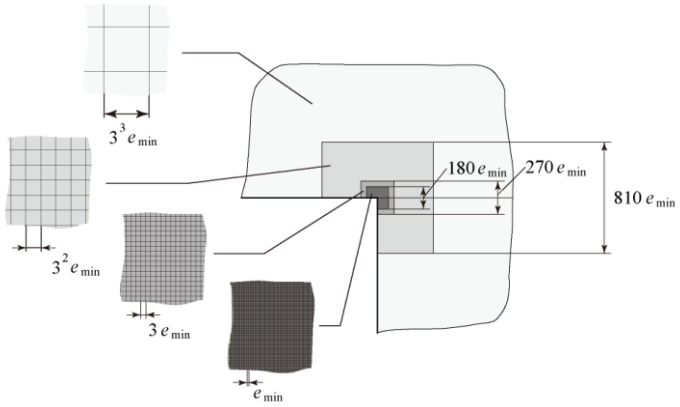

Fig.4. 9 Mesh pattern near the interface edge corner.

The analysis results of the specimen A25 under $\sigma_0 = 1$ MPa are shown as follows. The contour integral path C in Fig. 4.8 and the mesh pattern in Fig. 4.9 are used in order to calculate the ISSF. Table 4.5 shows K_{σ,λ_1}, K_{σ,λ_2}, K_{τ,λ_1}, K_{τ,λ_2} with varying $e_{\min}$ and $l/e_{\min}$ where l is the path dimension in Fig. 4.8 and $e_{\min}$ is the mesh dimension in Fig. 4.9. As shown in Table 4.5, the values with stronger singularity can be obtained as K_{σ,λ_1} =0.1010 and K_{τ,λ_1} = -0.04723 when $l/e_{\min} \geq 10$. Similarly, the values with weaker singularity can be obtained as K_{σ,λ_2} =-0.5485 and K_{τ,λ_2} = -0.01168 when $l/e_{\min}$ is large enough. Fig. 4.10 shows the interface stress σ_y and τ_{xy} obtained by substituting these intensity of singular stress fields into Eq.(4.3). The circle and triangle marks denote the

stresses σ_y and τ_{xy} obtained by using FEM, respectively. When $r \le 0.01$ mm, the marks are in good agreement with the solid curves.

Table 4.5 K_{σ,λ_1}, K_{σ,λ_2}, K_{τ,λ_1} and K_{τ,λ_2} of specimen A25 under $\sigma_0 = 1$ MPa

$l/e_{\min}$	$e_{\min} = 3^{-11}$ mm				$e_{\min} = 3^{-9}$ mm			
	K_{σ,λ_1}	K_{σ,λ_2}	K_{τ,λ_1}	K_{τ,λ_2}	K_{σ,λ_1}	K_{σ,λ_2}	K_{τ,λ_1}	K_{τ,λ_2}
5	0.1010	-0.5347	-0.04727	-0.01139	0.1011	-0.5511	-0.04728	-0.01174
10	0.1010	-0.5440	-0.04724	-0.01158	0.1010	-0.5497	-0.04724	-0.01171
20	0.1010	-0.5500	-0.04724	-0.01171	0.1010	-0.5484	-0.04724	-0.01168
40	0.1010	-0.5472	-0.04723	-0.01165	0.1010	-0.5485	-0.04723	-0.01168
80	0.1010	-0.5485	-0.04723	-0.01168	0.1010	-0.5486	-0.04723	-0.01168

K_{σ,λ_1}, K_{τ,λ_1}: $\mathrm{MPa}\cdot\mathrm{m}^{1-\lambda_1}$, K_{σ,λ_2}, K_{τ,λ_2}: $\mathrm{MPa}\cdot\mathrm{m}^{1-\lambda_2}$

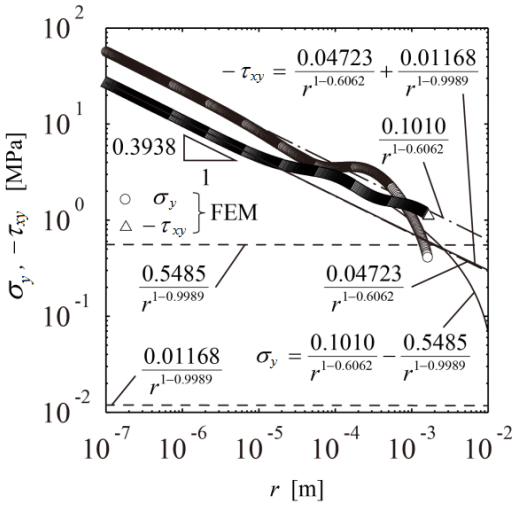

Fig.4. 10 Comparison between stress distribution of specimen A 25 by Eq. (4.3) and FEM.

Since chapter 4.2 shows the stress distribution normalized by the results of A25, the specimen geometry of A25 in Table 4.2 is analyzed by RWCIM and indicated in Table 4.5. Table 4.6 shows the all results in Table 4.3 obtained from in Eqs. (4.6), (4.7) with Table 4.6. Table 4.6 also shows the results obtained by applying RWCIM directly to all geometries in Table 4.2. The results with the stronger stress singularity λ_1 agree well

with the RWCIM's results although small difference can be seen for the results for weaker stress singularity λ_2. It may be concluded that the proposed method with the reference solution provides the ISSF conveniently. In addition, the normalized ISSF can be obtained more easily without the reference solution. Then they can predict the strength of adhesive joint accurately and conveniently.

Table 4.6 Comparisons of ISSF by using proposal method and RWCIM

(a) K_{σ,λ_1} and K_{τ,λ_1}

Specimen	K_{σ,λ_1} [MPa·m$^{1-\lambda_1}$]			K_{τ,λ_1} [MPa·m$^{1-\lambda_1}$]		
	K_{σ,λ_1} by using Eq.(4.6)	K_{σ,λ_1} by using RWCIM	Error(%)	K_{τ,λ_1} by using Eq.(4.7)	K_{τ,λ_1} by using RWCIM	Error(%)
A25(Ref)	0.1010	0.1010	0	-0.04723	-0.04723	0
A10	0.1065	0.1065	-0.0063	-0.0498	-0.04981	-0.0109
A15	0.1084	0.1083	0.0706	-0.05068	-0.05068	0.0024
A20	0.1056	0.1056	0.0241	-0.04938	-0.0494	-0.0127
A30	0.09609	0.09606	0.0303	-0.04493	-0.04723	-0.0130
A35	0.09111	0.09107	0.0396	-0.0426	-0.04494	-0.0137
A40	0.08621	0.08618	0.0359	-0.04032	-0.04261	-0.0121
A50	0.07682	0.07680	0.0295	-0.03593	-0.04032	-0.0131
A25-30	0.09801	0.09796	0.0471	-0.04583	-0.03593	-0.0043
A25-45	0.09782	0.09777	0.0500	-0.04574	-0.04583	-0.0011
A25-90	0.1013	0.1013	0.0288	-0.04738	-0.04574	-0.0006
A30-30	0.09298	0.09294	0.0444	-0.04348	-0.04738	-0.0031
A30-45	0.09250	0.09246	0.0456	-0.04325	-0.04348	0.0083
A30-90	0.09487	0.09482	0.0510	-0.04436	-0.04325	-0.0030

(b) K_{σ,λ_2} and K_{τ,λ_2}

Specimen	K_{σ,λ_2} [MPa·m$^{1-\lambda_2}$]			K_{τ,λ_2} [MPa·m$^{1-\lambda_2}$]		
	K_{σ,λ_2} by using Eq.(4.6)	K_{σ,λ_2} by using RWCIM	Error(%)	K_{τ,λ_2} by using Eq.(4.7)	K_{τ,λ_2} by using RWCIM	Error(%)
A25(Ref)	-0.5485	-0.5485	0	-0.01168	-0.01168	0
A10	-0.5783	-0.6469	-10.600	-0.01232	-0.01378	-10.619
A15	-0.5886	-0.6021	-2.2489	-0.01253	-0.01282	-2.2349
A20	-0.5736	-0.5735	0.0208	-0.01222	-0.01222	-0.0402
A30	-0.5218	-0.5237	-0.3570	-0.01111	-0.01168	-0.4279
A35	-0.4948	-0.4985	-0.7484	-0.01054	-0.01116	-0.7907
A40	-0.4682	-0.4741	-1.2476	-0.01000	-0.01062	-1.2876
A50	-0.4172	-0.4280	-2.5233	-0.00889	-0.00912	-2.5627
A25-30	-0.5322	-0.5022	5.9819	-0.01133	-0.01070	5.9186
A25-45	-0.5312	-0.4884	8.7683	-0.01131	-0.01040	8.7635
A25-90	-0.5503	-0.4888	12.579	-0.01172	-0.01041	12.555
A30-30	-0.5050	-0.4785	5.5283	-0.01075	-0.01019	5.5181
A30-45	-0.5024	-0.4644	8.1720	-0.01070	-0.00989	8.1233
A30-90	-0.5152	-0.4631	11.251	-0.01097	-0.00987	11.200

Table 4.7 shows the ratios of $K_{\sigma,\lambda_2}/K_{\sigma,\lambda_1}$, $K_{\tau,\lambda_2}/K_{\tau,\lambda_1}$ and $K_{\tau,\lambda_1}/K_{\sigma,\lambda_1}$, $K_{\tau,\lambda_2}/K_{\sigma,\lambda_2}$. Because K_{σ,λ_1} and K_{τ,λ_1} are defined from K_1 as shown in Eq. (4.10), the $K_{\tau,\lambda_1}/K_{\sigma,\lambda_1}$ is always constant as $K_{\tau,\lambda_1}/K_{\sigma,\lambda_1} \equiv -0.4678$ independent of l_{ad}, t_{ad}. Similarly, $K_{\tau,\lambda_2}/K_{\sigma,\lambda_2}$ is also always constant as $K_{\tau,\lambda_2}/K_{\sigma,\lambda_2} \equiv 0.02130$. In the experiment, the cohesive fracture occurs when l_{ad} < 15mm (specimens A10 and A15) and the adhesive fracture occurs when l_{ad} > 15mm as indicated in [8]. Except for the models A10 and A15, the values of $K_{\sigma,\lambda_2}/K_{\sigma,\lambda_1}$ and $K_{\tau,\lambda_2}/K_{\tau,\lambda_1}$ are in the smaller ranges as $K_{\sigma,\lambda_2}/K_{\sigma,\lambda_1}$ =-5.574 ~ -4.827 and $K_{\tau,\lambda_2}/K_{\tau,\lambda_1}$ =0.2198 ~ 0.2538 insensitive to l_{ad} and t_{ad}.

Table 4. 7 $K_{\sigma,\lambda_2}/K_{\sigma,\lambda_1}$, $K_{\tau,\lambda_2}/K_{\tau,\lambda_1}$, $K_{\tau,\lambda_1}/K_{\sigma,\lambda_1}$ and $K_{\tau,\lambda_2}/K_{\sigma,\lambda_2}$

Specimen	$K_{\sigma,\lambda_2}/K_{\sigma,\lambda_1}=C_\sigma$	$K_{\tau,\lambda_2}/K_{\tau,\lambda_1}=C_\tau$	$K_{\tau,\lambda_1}/K_{\sigma,\lambda_1}$	$K_{\tau,\lambda_2}/K_{\sigma,\lambda_2}$
A10	– 6.075	0.2766	-0.4678	0.02130
A15	– 5.557	0.2530	-0.4678	0.02130
A20	– 5.431	0.2473	-0.4678	0.02130
A25	– 5.430	0.2473	-0.4678	0.02130
A30	– 5.452	0.2483	-0.4678	0.02130
A35	– 5.474	0.2492	-0.4678	0.02130
A40	– 5.501	0.2505	-0.4678	0.02130
A50	– 5.574	0.2538	-0.4678	0.02130
A25-30	– 5.125	0.2334	-0.4678	0.02130
A25-45	– 4.995	0.2274	-0.4678	0.02130
A25-90	– 4.827	0.2198	-0.4678	0.02130
A30-30	– 5.148	0.2344	-0.4678	0.02130
A30-45	– 5.022	0.2287	-0.4678	0.02130
A30-90	– 4.885	0.2224	-0.4678	0.02130

$K_{\sigma,\lambda_2}/K_{\sigma,\lambda_1}$, $K_{\tau,\lambda_2}/K_{\tau,\lambda_1}$: $\mathrm{m}^{\lambda_1-\lambda_2}$

Therefore, interface stresses σ_y and τ_{xy} may be expressed by the following equation.

$$\sigma_y \cong \frac{K_{\sigma,\lambda_1}}{r^{1-\lambda_1}}\left(1+C_\sigma r^{\lambda_2-\lambda_1}\right),\ \tau_{xy} \cong \frac{K_{\tau,\lambda_1}}{r^{1-\lambda_1}}\left(1+C_\tau r^{\lambda_2-\lambda_1}\right) \tag{4.11}$$

Here, C_σ and C_τ are almost constant expressed as $C_\sigma = -5.3213 \pm 0.3379$, $C_\tau = 0.2423 \pm 0.0154$ (within 7% error) as shown in Table 4.7(l_{ad} =10~50mm, t_{ad} =0.15~0.9mm). If l_{ad} =10~15mm (A10,A15) is not considered, $C_\sigma = -5.2387 \pm 0.2660$, $C_\tau = 0.2386 \pm 0.0121$ (within 5% error). Therefore, C_σ =const is suitable for most of adhesive geometries except for very short adhesive length. Fig. 4.11 shows $\sigma_y/(K_{\sigma,\lambda_1}/r^{1-\lambda_1})$ and $\tau_{xy}/(K_{\tau,\lambda_1}/r^{1-\lambda_1})$ for all specimens except for A10 and A15. The dashed line shows the results of A50 and the dashed-dotted line shows the results of A25-90. It is found that all curves are within the thin black area between A50 and A25-90. In other words, the singular stress fields of all the specimens are similar. Since

$\sigma_y/(K_{\sigma,\lambda_1}/r^{1-\lambda_1}) =$ 0.94~1 and $\tau_{xy}/(K_{\tau,\lambda_1}/r^{1-\lambda_1}) \cong 1$, the effects of $K_{\sigma,\lambda_2}/r^{1-\lambda_2}$ and $K_{\tau,\lambda_2}/r^{1-\lambda_2}$ in Eqs.(4.4),(4.5) are very small. Since K_{σ,λ_1} and K_{τ,λ_1} are defined from K_1 as shown in Eq. (4.10), the ISSF can be represented by K_{σ,λ_1} as discussed in chapter 4.2.

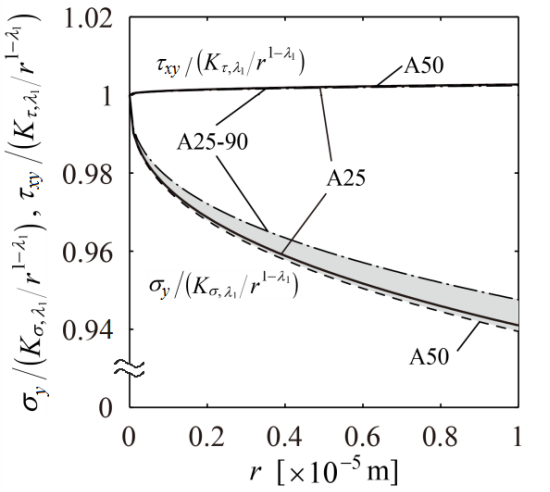

Fig.4.11 Normalized stress distributions $\sigma_y/\left(K_{\sigma,\lambda_1}/r^{1-\lambda_1}\right), \tau_{xy}/\left(K_{\tau,\lambda_1}/r^{1-\lambda_1}\right)$.

Therefore, the ISSF of lap joints as well as butt joints can be obtained conveniently by using the analysis method presented in this paper. It is found that although the singular stress is controlled by two factors for lap joints, it can be expressed almost similarly even if the adhesive geometries are changed widely. Since RWCIM requires the complex and difficult calculations such as matrix operation and numerical integration, the proposed method in chapter 4 is found to be very convenient and practical to determine ISSF.

4.4 Conclusions

In this chapter, a convenient analysis method for the ISSF of lap joint is presented. The conclusions can be summarized in the following way.

(1) In this study, a convenient analysis method of adhesive strength is presented in

terms of the ISSF (intensity of singular stress field). In this method, the same mesh pattern is applied to the unknown problems and the reference problems by focusing on the FEM stress at the interface corner.

(2) Although the singular stress is controlled by two factors for lap joints, it is found that the debonding condition can be expressed almost in the same way even if the adhesive geometries are widely changed. Therefore, the ISSF of lap joints as well as butt joints can be obtained conveniently by using the analysis method presented in this paper.

(3) The usefulness of the present solution is verified by comparing with the results of the conventional method (RWCIM). Since RWCIM requires the complex and difficult calculations such as matrix operation and numerical integration, the proposed method is found to be very convenient and practical to determine ISSF.

4.5 References

[1] BS EN 1465:1995, “Adhesives-determination of tensile lap-shear strength of rigidto-rigid bonded assemblies”.

[2] ASTM D 1002-1, “Standard test method for apparent shear strength of single-lap-joint adhesively bonded metal specimens by tension loading (metal-to-metal)”, ASTM Stand, 1-5.

[3] JIS K6850:1999. Adhesives-Determination of tensile lap-shear strength of rigid-to-rigid bonded assemblies.

[4] Mintzas A, Nowell D. Validation of an H_{cr}-based fracture initiation criterion for adhesively bonded joints. Eng Fract Mech 2012; 80: 13-27.

[5] Stern M, Soni ML. On the computation of stress intensities at fixed-free corners. Int

J Solids Struct 1976;12:331-7.

[6] Sinclair GB, Okajima M, Griffin JH. Path independent integrals for computing stress intensity factors at sharp notches in elastic plates. Int J Numer Methods Engng 1984;20:999-1008.

[7] Carpenter W, Byers C. A path independent integral for computing stress intensities for V-notched cracks in a bi-material. Int J Fract 1987;35:245-68.

[8] Qian ZQ, Akisanya AR. Wedge corner stress behavior of bonded dissimilar materials. Theor Appl Fract Mech 1999;32: 209-22.

[9] Labossiere PEW, Dunn ML. Stress intensities at interface corners in anisotropic biomaterials. Engng Fract Mech 1999;62:555-76.

[10] Im S, Kim KS. An application of two-state M-integral for computing the intensity of the singular near-tip field for a generic wedge. J Mech Phys Solids 2000;48: 129-51.

[11] Zhang Y, Noda NA, Takaishi K, Lan X. Effect of adhesive thickness on the intensity of singular stress at the adhesive dissimilar joint. J Solid Mech Mater Eng 2010; 4(10):1467–79.

[12] Zhang Y, Noda NA, Wu PZ, Duan ML. A mesh-independent technique to evaluate stress singularities in adhesive joints. Int J Adhes Adhes 2015; 57:105–117; the corrigendum of authorship is published in Int J Adhes Adhes 2015; 60:130.

[13] Park JH, Choi JH, Kweon JH. Evaluating the strengths of thick aluminum -to-aluminum joints with different adhesive lengths and thicknesses, Compos Struct 2010; 92: 2226-2235.

[14] Noda NA, Shirao R, Li J, Sugimoto JS. Intensity of singular stress fields causing interfacial debonding at the end of a fiber under pullout force and transverse tension.

Int J Solids Struct 2007; 44:4472–91.

[15] Yuuki, R. Mechanics of interface. Baifuukann, Tokyo, 1993, 283p [in Japanese].

[16] Bogy DB. Edge-bonded dissimilar orthogonal elastic wedges under normal and shear loading, Trans ASME J Appl Mech 1968; 35: 460-466.

[17] Bogy DB. Two edge-bonded elastic wedges of different materials and wedge angles under surface tractions, Trans ASME J Appl Mech 1971; 38: 377-386.

[18] Dundurs, J. Discussion: “Edge-bonded dissimilar orthogonal elastic wedges under normal and shear loading”. ASME J Appl Mech 1969; 36: 650-652.

[19] Carpenter, W. C. Byers C. A path independent integral for computing stress intensities for V-notched cracks in a bi-material, In J Fract 1987; 35: 245-268.

Chapter 5 Debonding criterion for single lap joint in terms of the ISSF

5.1 Introduction

Since the singular stress field usually exists at the interface corner [1], the interfacial debonding often occors under thermal and mechanical loading [2]. The experimental evaluation is time-consuming, therefore the practical and convenient debonding fracture criterion is desirable by using a convenient calculation method for the singular stress [3-6]. However, although the various studies have been done for single lap joints, the debonding fracture criterion cannot be expressed simply and conveniently [7,8].

In this chapter, the debonding strength of single lap joint will be investigated in terms of the critical value of ISSF $K_{\sigma c}$ by using the convenient analysis method presented in chapter 4, and the value of $K_{\sigma c}$ will be investigated based on the experimental results. The adhesive strength testing of single lap joint is standardized by Japanese Industrial Standards (JIS K6850) [9]. This standard prescribes the specimens with a small thickness 1.6 ± 0.1mm. Since large deformations usually appear before debonding for thin specimen, the thick specimens in Fig.5.1 [10,11] will be analyzed in this chapter.

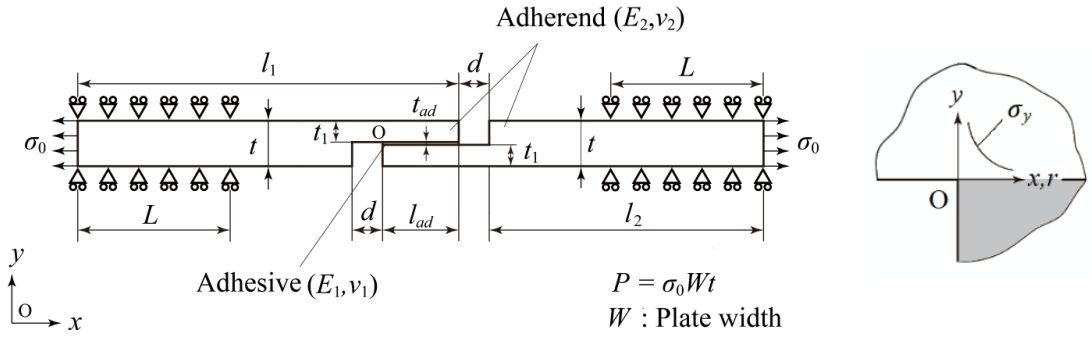

Fig.5. 1 Analysis model and boundary condition

5.2 Outline of the analysis method proposed for lap joint

As shown in chapter 4, for the single lap joint in Fig. 5.1 [10,11], the stresses σ_y and τ_{xy} at the interface corner can be expressed as follows.

$$\begin{aligned}\sigma_y &= \frac{K_{\sigma,\lambda_1}}{r^{1-\lambda_1}} + \frac{K_{\sigma,\lambda_2}}{r^{1-\lambda_2}} \cong \frac{K_{\sigma,\lambda_1}}{r^{1-\lambda_1}}\left(1 + C_\sigma\, r^{\lambda_2-\lambda_1}\right),\\ \tau_{xy} &= \frac{K_{\tau,\lambda_1}}{r^{1-\lambda_1}} + \frac{K_{\tau,\lambda_2}}{r^{1-\lambda_2}} \cong \frac{K_{\tau,\lambda_1}}{r^{1-\lambda_1}}\left(1 + C_\tau\, r^{\lambda_2-\lambda_1}\right).\end{aligned} \tag{5.1}$$

Here, $C_\sigma = K_{\sigma,\lambda_2} / K_{\sigma,\lambda_1}$ and $C_\tau = K_{\tau,\lambda_2} / K_{\tau,\lambda_1}$ are almost constant independent of adhesive geometry. The effects of $K_{\sigma,\lambda_2} / r^{1-\lambda_2}$ and $K_{\tau,\lambda_2} / r^{1-\lambda_2}$ in Eq.(5.1) are very small since $\lambda_2 \approx 1$, and the K_{σ,λ_1} and K_{τ,λ_1} are defined from same parameter K_1. Therefore, the ISSF can be represented by K_{σ,λ_1}.

The K_{σ,λ_1} can be obtained from the EFM stress ratio by applying the same mesh pattern to the reference problem as shown in Eq.(5.2). The exact value and calculate method of reference solution K^*_{σ,λ_1} were presented in chapter 4. Then, the critical ISSF $K_{\sigma c} = K_{\sigma,\lambda_1}|_{\sigma_o=\sigma_c}$ can be obtained.

$$\frac{K_{\sigma,\lambda_1}}{K^*_{\sigma,\lambda_1}} = \frac{\sigma_{y0,\mathrm{FEM}}}{\sigma^*_{y0,\mathrm{FEM}}} \tag{5.2}$$

5.3 Experimental results of single lap joint

The experimental results [10] considered in this chapter are presented. Since JIS specimen has a small thickness (adherend thickness is 1.5mm), it is difficult to calculate the critical stress intensity accurately because of large deformation appearing (see Fig. 5.2) before debonding was not indicated in the previous studies. In this chapter, therefore, the thick specimens used by Park [10] in Fig.5.1 are analyzed where the adherends aluminum alloy 6061-T6 are bonded with adhesive FM73M epoxy. In this

experiment, the authors prepared for the specimen very carefully to exclude the defect and voids. First, the surface of the adherend was polished with 40 mesh sandpaper and corroded using 27% sulfuric acid and 135g/L ferric sulfate for 12min. Then, the aluminum surfaces were cleaned and dried using water. The single lap joints were cured by autoclaving at 120 ^{o}C for 120 min. The typical force-displacement curves of the adhesively bonded joints show nearly linear behavior. In order to obtain an average failure load for each case, five specimens were tested. The failure load is the maximum value of the load, and a drop in load was used to detect a failure. In this experiment, during the bonding process, it was found that a small void may appear in the thicker adhesive (t_{ad}=0.3, 0.45, 0.9mm), which resulting in lower failure strength. To remove the voids from the thicker adhesive, the appropriate guide blocks were machined and secured onto the single lap joints. Failure load in the specimens without internal voids were 40.5% and 46.2% larger than for those with internal voids when the adhesive lengths of single lap joints are 25mm and 30mm, respectively [10]. Usually, the internal residual stress is caused by the contraction during the curing process, which affects the adhesive strength significantly. In this experiment, it was conjectured that the adhesive protrusion may be prevented between the adherend by using the guide blocks, which results in relieving the contraction due to the curing. Therefore, the guide blocks may contribute relieving the internal stress as well as removing the voids by curing the contraction.

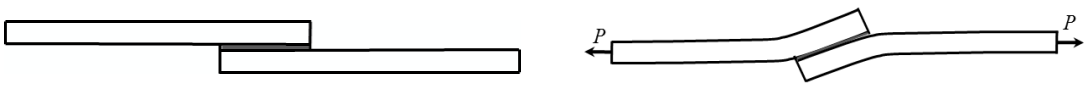

(a) Before loading (b) Under loading

Fig.5.2 Schematic illustration of deformation of thin lap joint.

In the experiment, fillet may exist at the bonded edge as shown in Fig.5.3(a). However, Arai and Kobayashi[12] found that the experimental specimens with fillet (see Fig.5.3(a)) and without fillet (see Fig.5.3(b)) have the same strength. The influence of the fillet geometries is numerically investigated by Campilho, Moura and Domingues[13]. It is reported that the joint strengths of the specimens with fillet (close to the actual fillet) are only slightly larger than the one without fillet. Therefore, the analysis model as shown in Fig.5.3(b) is considered in this study.

(a) With fillet (adhesive geometry in experiment)

(b) Without fillet (analysis model in this study)

Fig.5.3 Fillet at bonded edge

Table 5.1 shows the elastic parameters of the adherend and adhesive. Table 5.2 and Fig. 5.4 show the fracture load P_{af} and tensile adhesive strength σ_c ($\sigma_c = P_{af} / Wt$). As for all specimens except for A10, the relation between the load and displacement is almost linear. Therefore, it can be considered that the fractures were caused by the unstable growth of the crack which was initiated from the corner edge. The results bring the validation of the evaluation based on the ISSF. When the adhesive length becomes long under constant adhesive thickness condition, the adhesive strength tends to increase; when the adhesive layer becomes thick under constant adhesive length, the adhesive strength does not change remarkably. Fig. 5.5 shows the critical average shear stress τ_c. When l_{ad} is smaller than about 15mm, τ_c becomes constant at about 27.8MPa. However, when l_{ad} is larger than about 15mm, τ_c tends to decrease.

Nono and Nagahiro [14] discussed the adhesive joint strength with varying adhesive geometries. They indicated that the fracture average shear stress τ_c of the adhesive layer in lap joints is almost constant when the adhesive length is small enough. The fracture for single lap joint having smaller adhesive length may be described by the average shear stress, but the fracture of single lap joint having longer adhesive length can be described by the ISSF.

Table 5.1 Material properties of adhesive and adherent.

Material		Young's modulus E [GPa]	Poisson's ratio ν	α	β	λ_1	λ_2
Adherent	6061-T6	68.9	0.30	-0.8699	-0.06642	0.6062	0.9989
Adhesive	Epoxy resin	4.20	0.45				

Table 5.2 Experimental results

Specimen	l_{ad} [mm]	t_{ad} [mm]	P_{af} [kN]		σ_c [MPa]	
			without guide block	with guide block	without guide block	with guide block
A10	10	0.15	6.87	-	19.42	-
A15	15	0.15	10.57	-	29.88	-
A20	20	0.15	12.41	-	35.08	-
A25	25	0.15	14.17	-	40.06	-
A30	30	0.15	14.56	-	41.16	-
A35	35	0.15	16.41	-	46.39	-
A40	40	0.15	18.09	-	51.14	-
A50	50	0.15	18.22	-	51.51	-
A25-30	25	0.30	14.32	19.54	40.06	31.26
A25-45	25	0.45	14.26	20.04	39.47	32.06
A25-90	25	0.90	14.19	17.54	38.09	28.06
A30-30	30	0.30	16.91	22.85	47.30	30.47
A30-45	30	0.45	16.12	23.57	44.62	31.43
A30-90	30	0.90	15.37	21.50	41.26	28.67

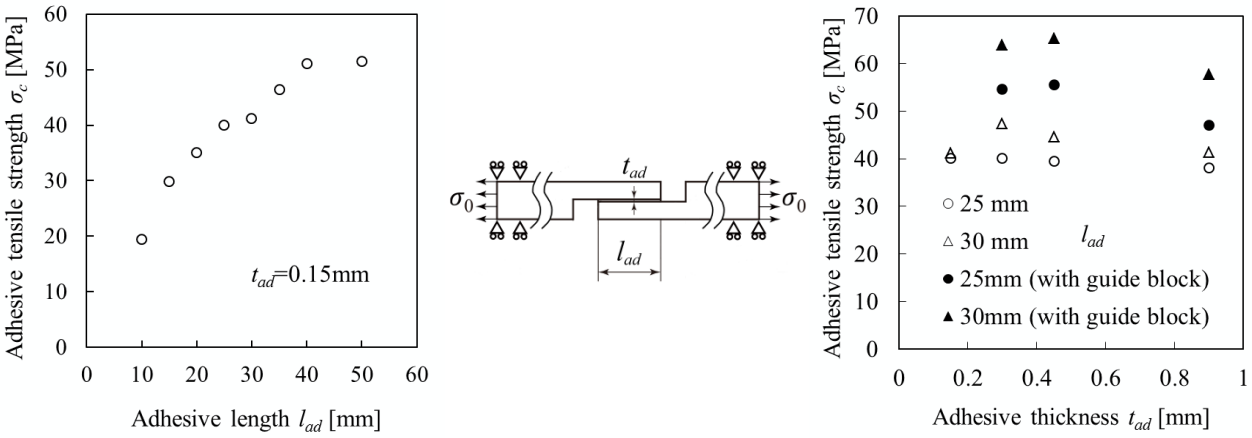

(a) t_{ad}=0.15mm (b) l_{ad}=25,30mm

Fig.5.4 Adhesive tensile strength.

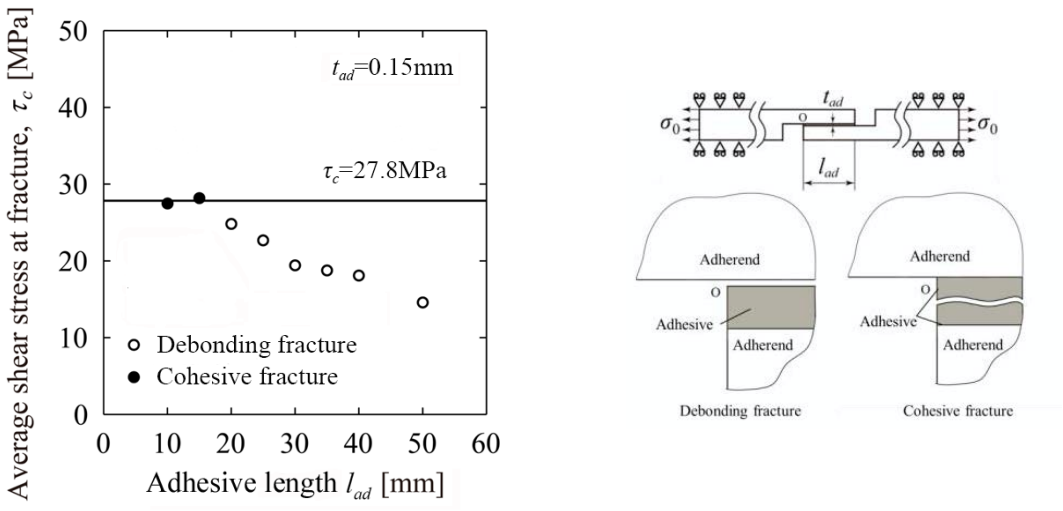

Fig.5.5 Average shear stress at fracture of specimens with t_{ad} = 0.15 mm.

In order to confirm the conclusion, the specimen used by Naito is also considered [11]. In this experiment, the authors also prepared for the specimen carefully to exclude the defect and voids, and there were no visible micro-sized voids in the polyimide adhesives. Before bonding, the adherends were cleaned and degreased by acetone and dried at room temperature under laboratory environment. Then, the adherends were heated to 200℃ to remove the residual solvent and the bond between the layers. The polyimide single lap joint was successfully fabricated by using the layer-by-layer

technique, drying process and autoclave curing. The load applied to the specimen was almost linearly proportional to the displacement until failure. The total length of the specimen is 190.5mm, adhesive length l_{ad}=12.7mm, the adherend thickness t_1=3mm, the adherend length l_2=25.4mm, the fixed boundary length L=25.4mm. Table 5.3 shows material properties of adherend and adhesives.

Table 5.4 and Fig. 5.6 show the adhesive shear strengths τ_c and tensile adhesive strength σ_c [11]. The experimental results show that when t_{ad} is smaller than about 0.3mm (l_{ad}=12.7mm), the change of the adhesive tensile strength σ_c is relatively unstable. When t_{ad} is larger than about 0.3mm, the adhesive tensile strength σ_c tends to decrease.

Table 5.3 Material properties of adherend and adhesives

Combination		Young's modulus E [GPa]	Poisson's ratio ν	α	β	λ_1	λ_2
Adherent	Aluminum alloy	69.6	0.33	-0.8963	-0.2145	0.6646	0.9990
Adhesive	Polyimide	3.77	0.342				

Table 5.4 Experimental results

t_{ad} [mm]	τ_c [MPa]	σ_c [MPa]
0.1	8.65±0.9	18.01±1.87
0.2	8.48±0.99	17.37±2.03
0.3	9.42±0.97	18.99±1.96
0.4	9.57±0.87	18.99±1.73
0.5	9.82±0.58	19.19±1.13
0.6	10.01±0.83	19.26±1.59
0.7	9.45±1.44	17.91±2.73
0.9	8.62±1.5	15.87±2.76

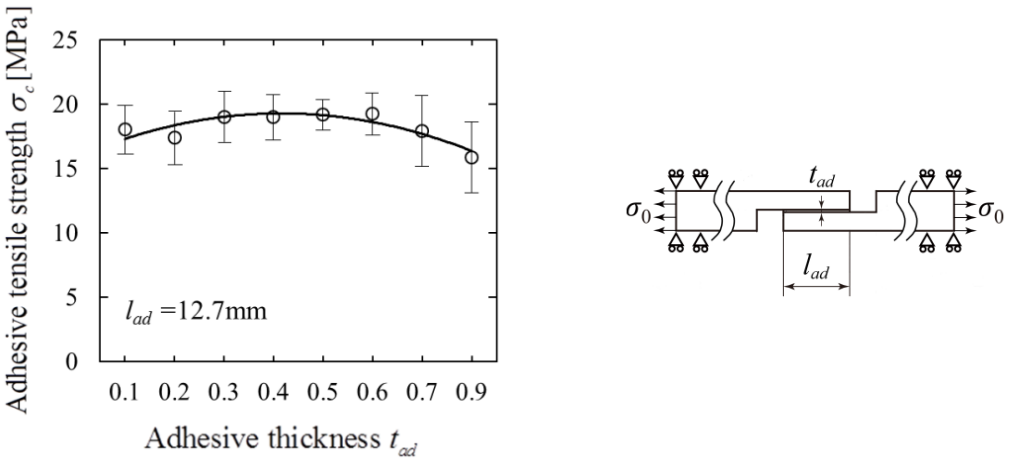

Fig.5.6 Adhesive tensile strength (l_{ad}=12.7mm).

5.4. Adhesive strength expressed as $K_{\sigma c}$ =const

In this chapter, the adhesive strength of single lap joint will be investigated by using the experimental results in chapter 5.3. First, the specimens in Table 5.2 [10] will be analyzed. Fig. 5.7 shows K_{σ,λ_1} under $\sigma_0 = 1$MPa with varying the adhesive length l_{ad}. It is seen that K_{σ,λ_1} decreases when $l_{ad} \geq 15$mm. The experimental observation in Fig. 5.8(a) shows that when l_{ad} < 15mm the cohesive fracture occurs. When l_{ad} > 15mm, the adhesive fracture occurs. Fig.5.8(b) shows the critical $K_{\sigma c}$ when the debonding occurs under $\sigma_o = \sigma_c$ with varying l_{ad}. When l_{ad} > 15mm, the adhesive fracture occurs and $K_{\sigma c}$ becomes constant independent of l_{ad}. The solid line shows the average value of $K_{\sigma c}$ for all specimens expect for specimens A10 and A15. The open circle marks are distributed near the solid line within about 10% error.

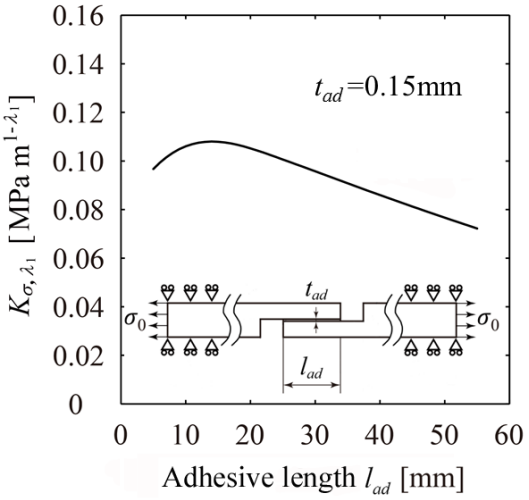

Fig.5.7 Relationship between K_{σ,λ_1} and l_{ad} under $\sigma_0 = 1\,\mathrm{MPa}$.

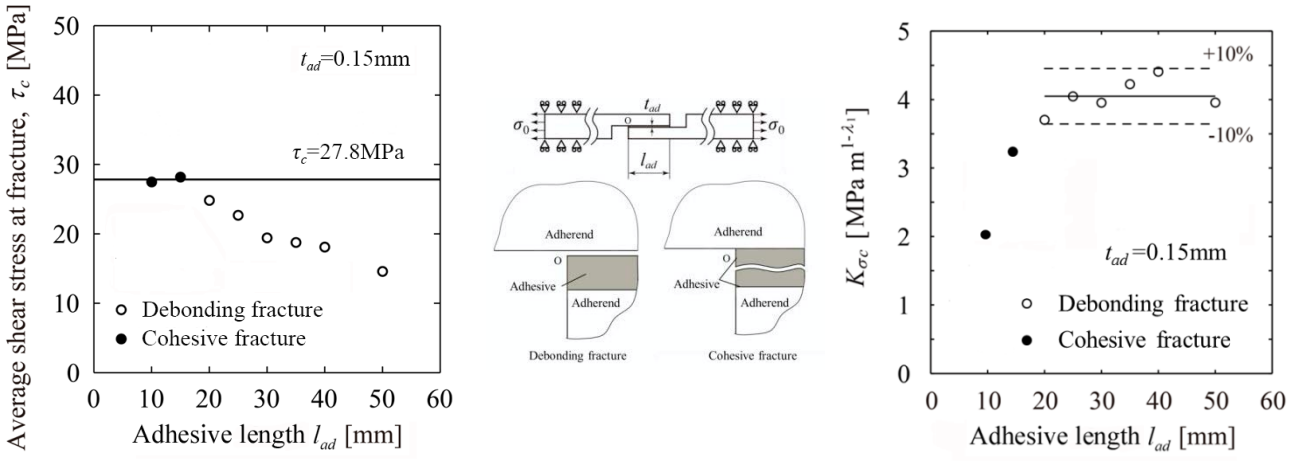

(a) (b)

Fig.5. 8 (a) Average shear stress at fracture of specimens with t_{ad} = 0.15 mm, (b) Relationship between $K_{\sigma c} = K_{\sigma,\lambda_1}|_{\sigma_o=\sigma_c}$ and l_{ad}.

Fig. 5.9 shows the relationship between K_{σ,λ_1} and adhesive thickness t_{ad} under $\sigma_0 = 1\,\mathrm{MPa}$. The solid line and dashed line denote the values of K_{σ,λ_1} for l_{ad}=25mm and 30mm, respectively. It is found that the K_{σ,λ_1} is almost constant independent of t_{ad}. Fig.5.10 shows the relationship between $K_{\sigma c}$ and t_{ad} under $\sigma_o = \sigma_c$. The results of $K_{\sigma c}$ are plotted in Fig. 5.10 (a) for the specimens without guide block and in Fig. 5.10

(b) for the specimens with guide block. It is seen that the strength is improved by using the guide block. This is because the size and number of the internal voids decrease by using the guide block. It is found that the values of $K_{\sigma c}$ are almost constant independent of t_{ad} even if changing the testing method.

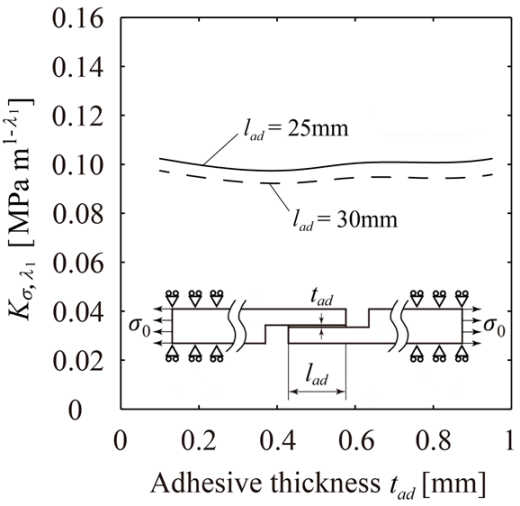

Fig.5.9 Relationship between K_{σ,λ_1} and t_{ad} when $\sigma_0 = 1\,\mathrm{MPa}$.

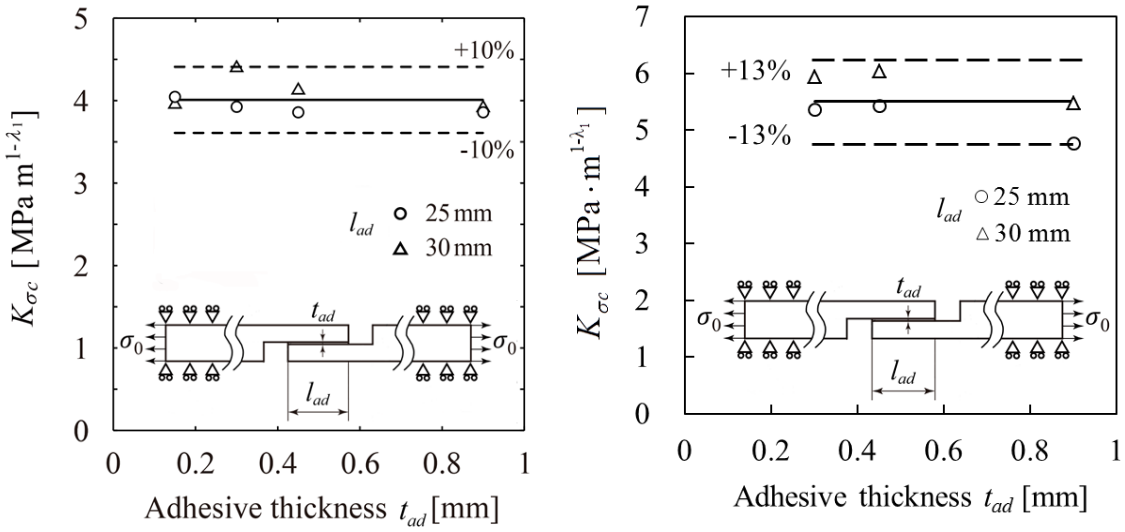

(a) Specimen without the guide block

(b) Specimen with the guide block

Fig.5.10 Relationship between $K_{\sigma c} = K_{\sigma,\lambda_1}|_{\sigma_o=\sigma_c}$ and t_{ad}.

Fig. 5.11 shows the critical $K_{\sigma c}$ of all specimens expect for specimens A10 and A15. The solid line shows the average values $K_{\sigma c,ave}$ = 4.030 MPa · m$^{1-\lambda_1}$ for the specimens without guide block, and $K_{\sigma c,ave}$ = 5.499 MPa · m$^{1-\lambda_1}$ for the specimens with guide block. The $K_{\sigma c}$ values are distributed within 10% error as shown in Fig. 5.11(a) and within 13% as shown in Fig. 5.11(b). It can be confirmed that the $K_{\sigma c}$ is almost constant independent of the l_{ad} and t_{ad}. Therefore, the debonding criterion of single lap joints can be described by the ISSF $K_{\sigma c}$ = const.

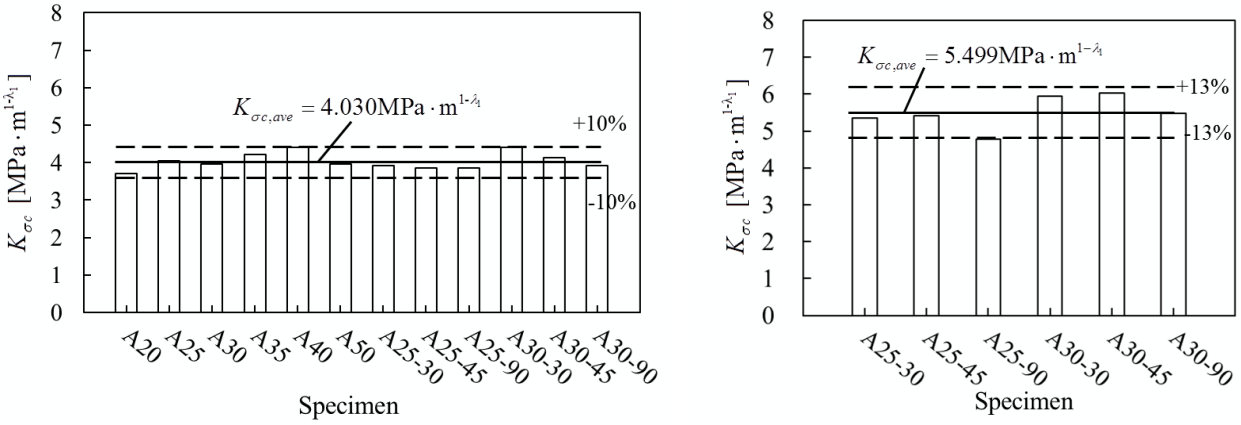

(a) Specimen without the guide block (b) Specimen with the guide block

Fig.5.11 Comparison between $K_{\sigma c}$ values.

In order to confirm the conclusion $K_{\sigma c}$ =const, the specimens in Table 5.4 are analyzed [11]. Fig.12 shows the relationship between K_{σ,λ_1} and adhesive thickness t_{ad} under σ_o =1MPa. When t_{ad} is smaller than about 0.3mm, the K_{σ,λ_1} tends to decrease. When t_{ad} is larger than about 0.3mm, K_{σ,λ_1} tends to increase. Fig. 5.13(a) shows the adhesive tensile strength σ_c with varying t_{ad}. Fig.5.13(b) shows the critical $K_{\sigma c}$ under $\sigma_o = \sigma_c$ with varying t_{ad}. The solid line shows the average value of $K_{\sigma c}$ for all specimens. It is found that the values of $K_{\sigma c}$ are almost constant independent of t_{ad}.

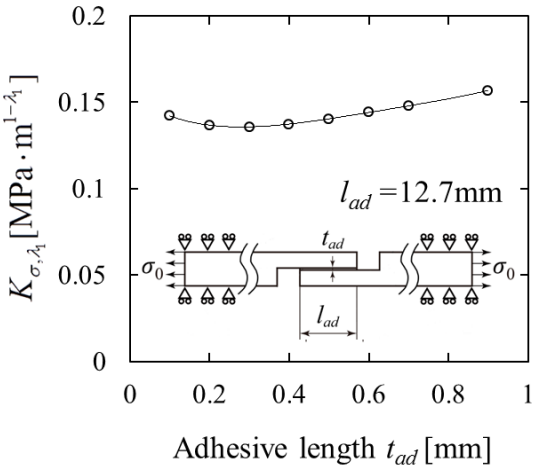

Fig.5.12 Relationship between K_{σ,λ_1} and t_{ad} when $\sigma_0 = 1$ MPa.

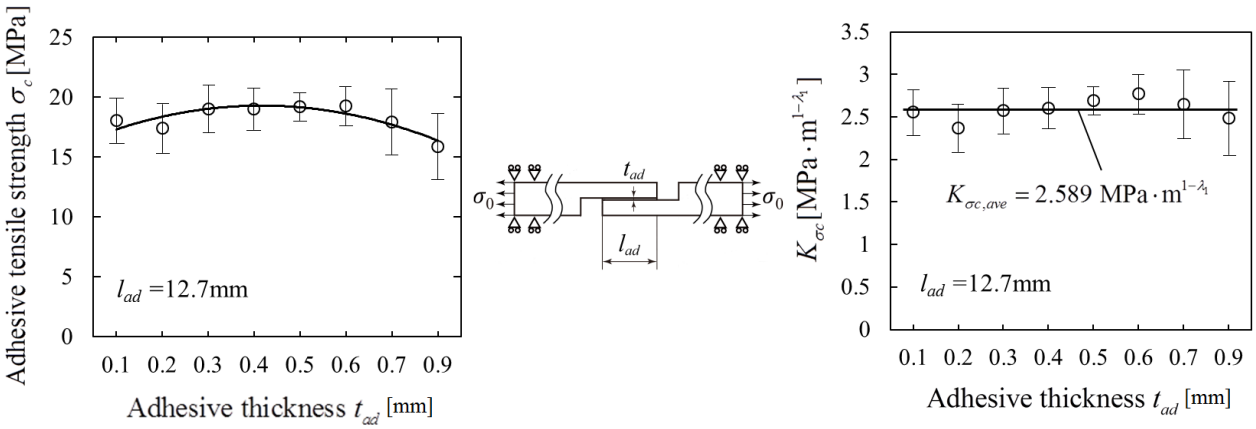

(a) (b)

Fig.5. 13 (a) Average tensile stress at fracture of specimens with l_{ad} = 12.7mm, (b) Relationship between $K_{\sigma c} = K_{\sigma,\lambda_1}|_{\sigma_o=\sigma_c}$ and t_{ad}.

In this chapter, the value of $K_{\sigma c}$ is investigated based on the experimental result. It is found that the adhesive strength can be expressed as $K_{\sigma c}$ =const. Since the experiments are often time-consuming, the proposed FEM calculation is helpful for predicting the adhesive strength accurately and conveniently.

5.5. Conclusion

In this study, the debonding fracture criterion for the single lap joint is examined with varying the adhesive length and adhesive length. The conclusions can be summarized in the following way.

(1) The adhesive strength of single lap joint is discussed in terms of critical ISSF $K_{\sigma c}$. The values of critical ISSF $K_{\sigma c}$ can be calculated by using the method presented in chapter 4.

(2) Based on the obtained ISSF, the debonding criterion is examined with varying the adhesive geometries. The results show that the adhesive strength for single lap joint can be evaluated as $K_{\sigma c}$=const when the debonding fracture occurs (except for the specimen with very short adhesive length).

5.6 References

[1] Yuuki, R. Mechanics of interface. Baifuukann, Tokyo, 1993, 283p [in Japanese].

[2] Shibuya T. Evaluation of crack initiation at interfacial edge on the basis of fracture mechanics concept and application to electronics devices. J Jpn Inst Electron Packag 2004; 7(7): 639-644 [in Japanese].

[3] Hattori T, Sakata S, Hatsuda T, Murakami G. A stress singularity parameter approach for evaluating adhesive strength. JSME Int J Ser 1 Solid Mech Strength Mater 1988; 31(4):718–23.

[4] M. Shiratori. Problems of joints in packaging of electronic devices. Trans Jpn Soc Mech Eng A 1994; 60(577): 1905-1912 [in Japanese].

[5] Kitamura T, Shibutani T, Ueno T. Development of evaluation method for interface strength between thin films and its application on delamination of Cu/TaN in an advanced LSI. Trans Jpn Soc Mech Eng A 2000; 66(648): 1568-1573 [in Japanese].

[6] Shibutani T, Tsuruga T, Yu Q, Shiratori M. Criteria of crack initiation at edge of

interface between thin films in opening an sliding modes for an advanced LSI. Trans Jpn Soc Mech Eng A 2003; 69(685): 1368-1373 [in Japanese].

[7] Nono K, Nagahiro T. A comparison of predicted strength and experimental results of adhesive joints. Trans Jpn Soc Mech Eng A 1986; 52(479): 1698-1707 [in Japanese].

[8] Kyogoku H, Sugibayashi T, Ikegami K. Strength evaluation of asymmetric single lap joints: 3rd Report, Effects of mechanical properties of adherends. Bull JSME 1986; 29(258): 4064-4071.

[9] JIS K6850:1999. Adhesives-Determination of tensile lap-shear strength of rigid-to-rigid bonded assemblies.

[10] Park JH, Choi JH, Kweon JH. Evaluating the strengths of thick aluminum -to-aluminum joints with different adhesive lengths and thicknesses, Compos Struct 2010; 92: 2226-2235.

[11] Naito K, Onta M, Kogo Y. The effect of adhesive thickness on tensile and shear strength of polyimide adhesive. Int J Adhes Adhes 2012;36:77–85.

[12] Arai M, Kobayashi H. Adhesively bonded lap joints: Fracture mechanisms and strength evaluation. Trans Jpn Sco Mech Eng A 1998: 64(619): 74-79.

[13] Campilho RDSG, Moura de MFSF, Domingues JJMS. Numerical prediction on the tensile residual strength of repaired CFRP under different geometric changes. International Journal of Adhesion and Adhesives 2009;29: 195-205.

[14] Nono K, Nagahiro T. A comparison of predicted strength and experimental results of adhesive joints. Trans Jpn Soc Mech Eng A 1986; 52(479): 1698-1707 [in Japanese].

Chapter 6 Adhesive strength evaluation method focusing on the ISSF to minimize bend effect for single lap joint

6.1 Introduction

The convenient analysis method of the ISSF for butt joint and lap joint is presented in previous chapters. The results shows that the adhesive strength for butt joint can be expressed as the critical ISSF $K_{\sigma c}$=const (see chapter 3), and the adhesive strength of single lap joint also can be expressed as $K_{\sigma c}$=const (see chapter 5).

The testing method for the adhesive strength of lap joints is standardized by Japanese Industrial Standards (JIS) [1]. However, the strength is affected by the specimen dimension and difficult to be applied to other geometries. Compared with double lap joint, single lap joint can be used conveniently. However, the experimental results in [2,3] show that the strength of double lap joint is nearly twice larger than the one of single lap joint (see Fig. 6.1). Therefore, it is necessary to find a suitable evaluation method for single lap joint testing.

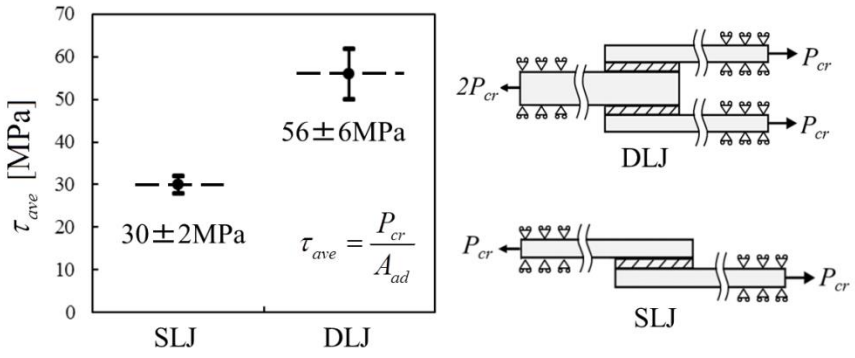

Fig.6.1 Adhesive strength for single lap joint (SLJ) and double lap joint (DLJ)
(Adherend: S45C, Adhesive: Epoxy)

The single lap joint testing should be done under pure shear loading, but pure shear

testing is difficult to be realized in the experiment. Due to the bend deformation of single lap joint during testing, the peeling force is applied to the adhesive region. Then the ISSF at the interface corner is affected by the peeling force due to the deformation. Therefore, in this chapter, the adhesive strength evaluation method to minimize bend effect for single lap joint will be investigated in terms of the ISSF appearing at the interface corner. The effect of the specimen geometry on ISSF and deformation angle at the interface corner will be considered under the same adhesive geometry and load P based on the specimen used by Park [4] (Adherend: Aluminum alloy 6061-T6, Adhesive: FM73M epoxy). The value of the ISSF of lap joint can be obatined by using the analysis method presented in chapter 4. In addition, the equivalent conditions of strength for the single lap joint and double lap joint will be considered.

6.2 Pure shear testing to minimize ISSF

In this chapter, the adhesive strength evaluation method to minimize bend effect is investigated in terms of the ISSF appearing at the interface corner. In order to minimize ISSF, the effect of specimen geometry is considered under the same adhesive geometry and load P.

Fig.6.2 shows the two models of single lap joint considered in this study. One is the model with different fixed boundary lengths L as shown in Fig.6.2(a), and the other is the model with different tensile force directions (L=0) as shown in Fig. 6.2(b). l_1 and t_1 are the adherend length and adherend thickness, l_{ad} and t_{ad} are the adhesive length and adhesive thickness, L is the fixed boundary length of adherend, σ_o is the tension at both ends of single lap joint, and e is the distance from center point of loading surface to loading point. In this chapter, the total length of the specimen is 225mm, the adhesive

length l_{ad} =25mm, adhesive thickness t_{ad} =0.15mm, d =10mm, load P =14.15N.

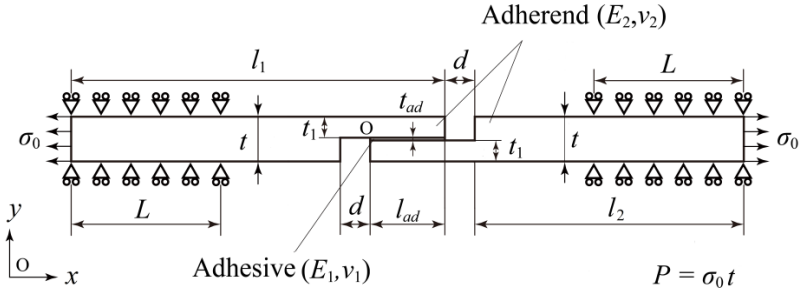

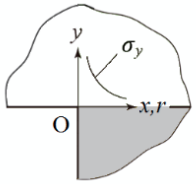

(a) Fixed boundary length $L \neq 0$

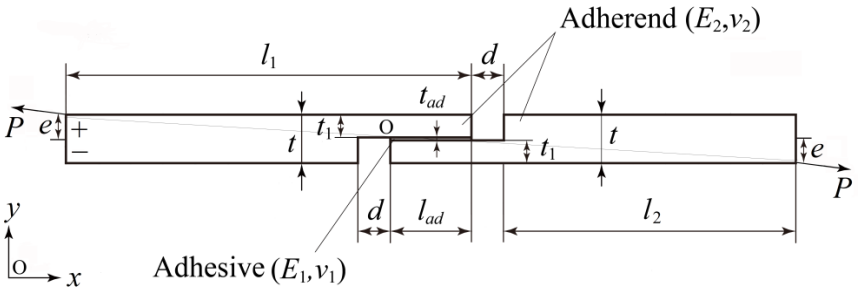

(b) Fixed boundary length $L = 0$, change P direction

Fig.6.2 Analysis model and boundary condition

Since the ISSF can be represented by K_{σ,λ_1} (see chapter 4), only K_{σ,λ_1} is considered in this study. The K_{σ,λ_1} can be obtained from the EFM stress ratio by applying the same mesh pattern to the reference problem as shown in Eq.(6.1). The exact value and calculate method of reference solution K^*_{σ,λ_1} were presented in chapter 4.

$$\frac{K_{\sigma,\lambda_1}}{K^*_{\sigma,\lambda_1}} = \frac{\sigma_{y0,\mathrm{FEM}}}{\sigma^*_{y0,\mathrm{FEM}}} \tag{6.1}$$

In order to obtain the value of minimum K_{σ,λ_1} ($K_{\sigma,\min}$), a special case in Fig. 6.3 is considered. Here, the adherends are fixed along x direction except for d. As shown in Fig. 6.3, the K_{σ,λ_1} first decreases and then increases with increasing adherend thickness t_1, and the K_{σ,λ_1} value becomes almost constant when t_1 is large enough. The $K_{\sigma,\min} = 0.0422\ \mathrm{MPa}\cdot\mathrm{m}^{1-\lambda_1}$ can be obtained when $t_1 = 13\mathrm{mm}$.

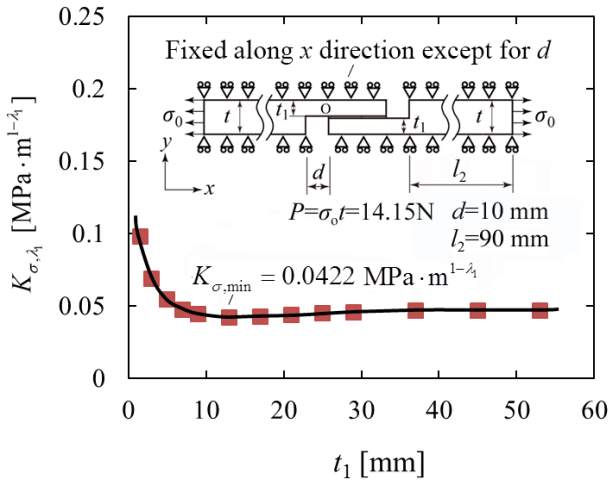

Fig.6.3 Effect of adherend thickness t_1 on K_{σ,λ_1} (Fixed along x direction except for d)

Fig. 6.4 shows the effects of adherend thickness t_1 and fixed boundary length L on ISSF K_{σ,λ_1}. Here, JIS* means the adherend thickness t_1=1.5mm and fixed boundary length L=50mm in JIS K6850 are used. The adshed line shows the value of $K_{\sigma,\min}$. As can be seen from the figure, the K_{σ,λ_1} decreases with increasing t_1 and L, and the K_{σ,λ_1} becomes constant if t_1 is large enough. When $t_1 \geq 25$mm, the K_{σ,λ_1} is almost constant independent of t_1 ($K_{\sigma,\lambda_1} \approx K_{\sigma,\min}$), and the effect of L on K_{σ,λ_1} can be ignored. The $K_{\sigma,\lambda_1}|_{t_1=1.5\text{mm}} = 0.2270$ MPa·m$^{1-\lambda_1}$ (JIS K6850) is 5 times larger than the one of $K_{\sigma,\min}$, the K_{σ,λ_1} of the specimen in [4] ($K_{\sigma,\lambda_1}|_{t_1=7\text{mm}} = 0.1010$ MPa·m$^{1-\lambda_1}$) is more than twice than that of $K_{\sigma,\min}$. It is seen that the specimen in [4] is better than the JIS, but it is more desirable to use larger adherend thickness.

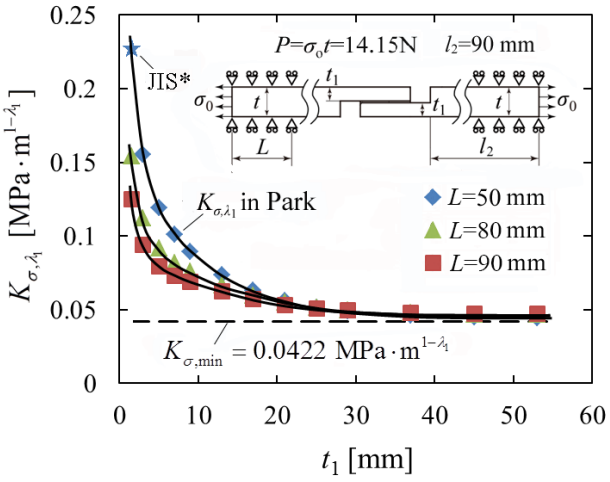

Fig.6.4 Effects of adherend thickness t_1 and fixed boundary length L on K_{σ,λ_1}
(JIS*: JIS K6850 prescribes specimen details t_1=1.5mm, L=50mm)

Fig. 6.5 shows the results of K_{σ,λ_1} with different adherend lengths l_2 and adherend thickness t_1 (L=50mm). Only in this figure, the total length of the specimen is not fixed in 225mm (145~335mm) because of the changing of adherend length l_2. The solid line shows the value of $K_{\sigma,\min}$. As shown in Fig. 6.5, the K_{σ,λ_1} increases with increasing l_2 when t_1=7mm. The values of K_{σ,λ_1} are distributed around the solid line with slight variations when t_1=53mm. Therefore, the influence of l_2 on the K_{σ,λ_1} can be ignored when t_1 is large enough. In other words, it is a good way to minimize K_{σ,λ_1} and reduce cost at the same time by using small l_2 and large t_1.

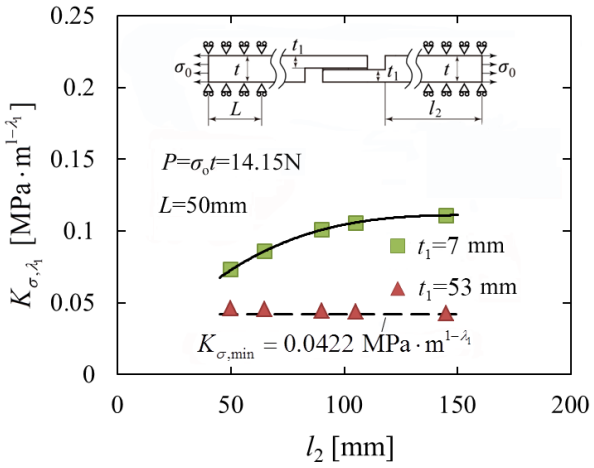

Fig.6. 5 Effects of adherend length l_2 and adherend thickness t_1 on K_{σ,λ_1}

As mentioned in chapter 4, the C_σ and C_τ are almost constant independent of adhesive geometry. However, it is found that the C_σ and C_τ are not only independent of adhesive geometry, but also almost constant independent of adherend geometry expect for thin adherend thickness. Fig. 6.6 shows the values of C_σ and C_τ for the single lap joint in Fig. 6.2(a) with various specimen geometries expect for t_1=1.5mm and t_1=3mm (l_{ad}=10~50mm, t_{ad}=0.15~0.9mm, t_1=5~53mm, l_2=50~145mm, L =50~90mm). As can be seen from Fig.6.6, C_σ=-5.0595±0.5467, C_τ=0.2304±0.0249, C_σ and C_τ are almost constant independent of specimen geometry. When t_1=1.5 and t_1=3mm (l_{ad}=25mm, t_{ad}=0.15mm, l_2=90mm, L=50mm), $C_\sigma|_{t_1=1.5\text{mm}}=-9.8942$, $C_\sigma|_{t_1=3\text{mm}}=-7.4799$, $C_\tau|_{t_1=1.5\text{mm}}=0.4505$, $C_\tau|_{t_1=3\text{mm}}=0.3406$. The possible reason for the large discrepancy between thin and thick specimen is thought to be due to the large deformation as well as the reason discussed for single lap joint strength. In the next chapter, we will investigate the deformation focusing on the deformation angle at the interface corner.

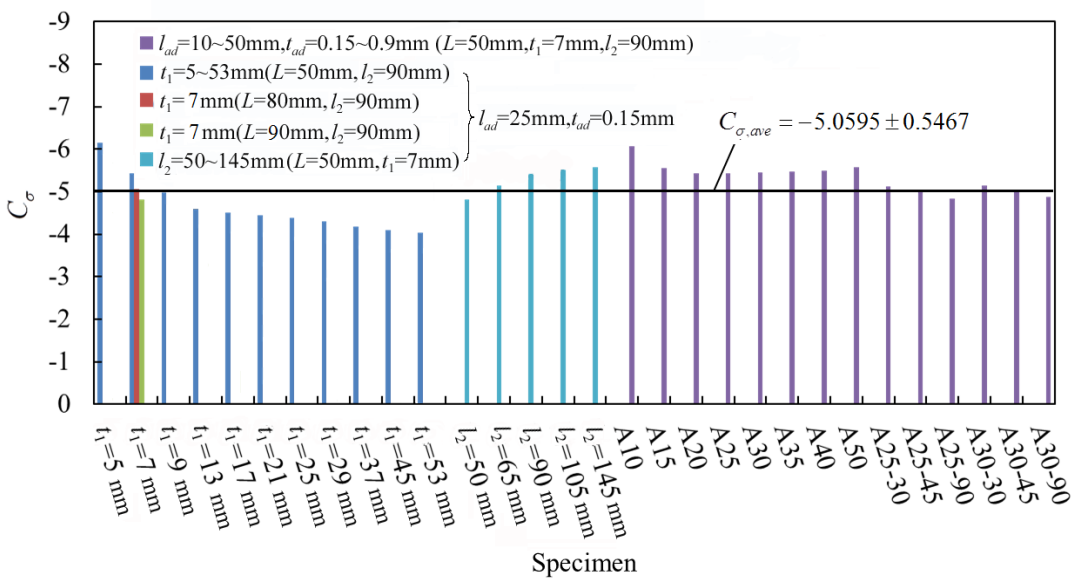

(a)

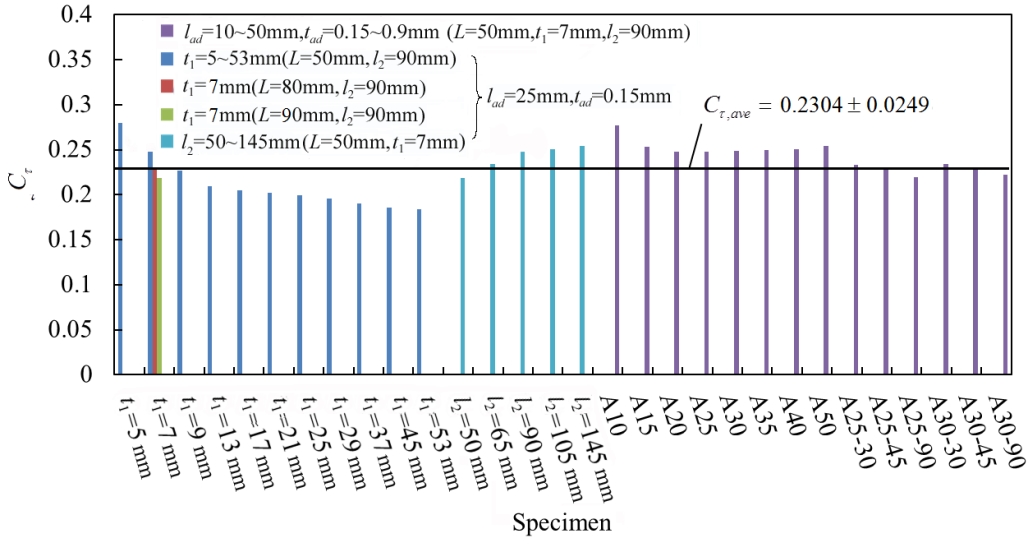

(b)

Fig.6.6 Results of (a) C_σ (b) C_τ for single lap joint with different specimen geometries

Fig. 6.7 shows the relationship between ISSF K_{σ,λ_1} and eccentric distance e for the model in Fig. 6.2(b). It is found that the K_{σ,λ_1} decreases with increasing distance e, the effect of e on the K_{σ,λ_1} is mainly reflected in the case of adherend thickness t_1 =7mm. When t_1=25mm, the K_{σ,λ_1} is almost constant independent of the e.

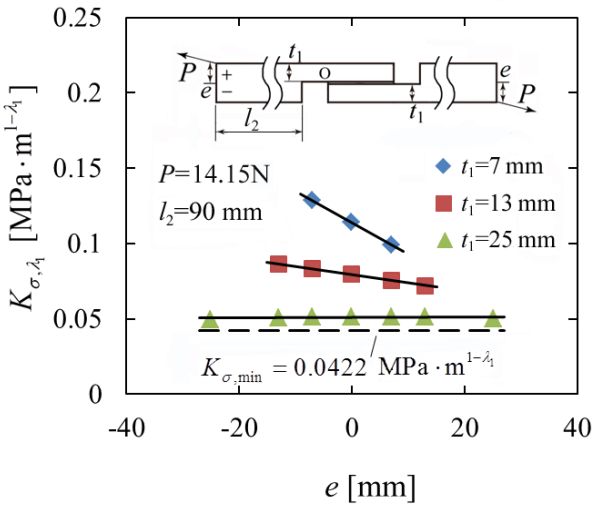

Fig.6.7 Effects of distance e and adherend thickness t_1 on K_{σ,λ_1}

6.3. Relationship between ISSF and deformation angle at the interface corner

Since ISSF is affected by the peeling force due to the deformation, the relationship between ISSF and deformation is investigated in this chapter. The same boundary condition and specimen geometry as in chapter 6.2 are used. The effect of specimen geometry is considered under the same adhesive geometry (l_{ad}=25mm, t_{ad}=0.15mm) and load P (P=14.15N) also.

Here, the deformation is studied by using the maximum value of the deformation angle θ_C at the interface corner C (see Fig.6.8). The detail information about the reason for this choice is indicated in Appendix E. For the deformation angle θ_C at the interface corner C, two target points are points C and D with distance l_θ.

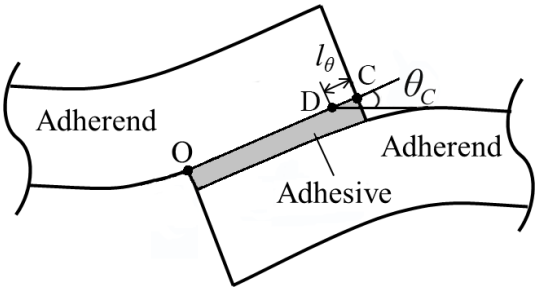

Fig. 6.8 Deformation near the interface corner

Table 6.1 shows the results of θ_C with different minimum mesh sizes $e_{\min}$ and distance l_θ (t_1=7mm, L=50mm and l_2=90mm). It is found that the maximum θ_C can be obtained when $l_\theta = 1/3^3$ mm and the value of maximum θ_C is constant independent of element size. This means that the analytical method is valid for single lap joint.

Table 6.1 θ_C with varying $e_{\min}$ and l_θ

l_θ [mm]	θ_C		
	$e_{\min}=1/3^{11}$ mm	$e_{\min}=1/3^{8}$ mm	$e_{\min}=1/3^{5}$ mm
$1/3^4$	0.0186	0.0188	0.0187
$1/3^3$	0.0194	0.0194	0.0194
$1/3^2$	0.0188	0.0188	0.0188
1/3	0.0162	0.0162	0.0162

In Fig. 6.3, a special case is considered to obtain the minimum ISSF K_{σ,λ_1}. In Fig. 6.9, the minimum deformation angle $\theta_C(\theta_{C,\min})$ is considered by using same boundary condition and specimen geometry as in Fig. 6.3. It is found that the deformation angle θ_C first decreases and then increases with increasing adherend thickness t_1, and the θ_C value becomes constant if t_1 is large enough. The $\theta_{C,\min} = 0.0042$ degree can be obtained when t_1=13mm.

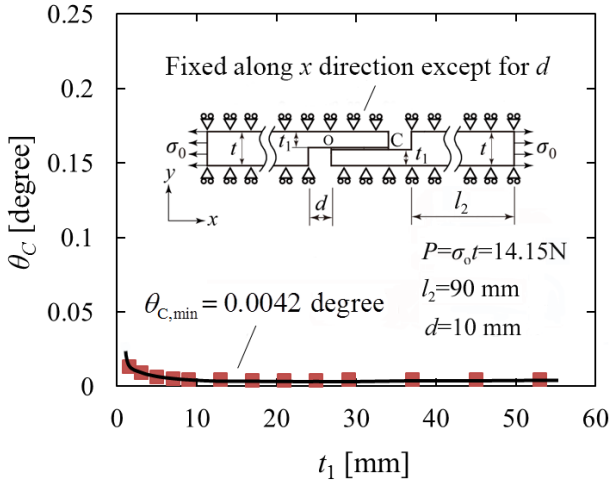

Fig.6.9 Effect of adherend thickness t_1 on θ_C (Fixed along x direction except for d)

The result of the deformation angle θ_C with different adherend thicknesses t_1 is plotted in Fig. 6.10. Since the fixed boundary length L is mostly around 50mm in the experiment, only L=50mm is considered in Fig. 6.10. The solid line shows the minimum value of θ_C. Here, JIS* means the adherend thickness t_1=1.5mm and fixed boundary length L=50mm in JIS K6850 are used. As can be seen from the figure, the θ_C first decreases rapidly and then become constant with increasing t_1, the minimum θ_C can be obtained when t_1 is large enough. The $\theta_C|_{t_1=1.5\text{mm}} = 0.1834$ degree (JIS) is about 40 times larger than the one of $\theta_{C,\min}$, the θ_C of the specimen in [4] ($\theta_C|_{t_1=7\text{mm}} = 0.0193$ degree) is about 4 times larger than that of $\theta_{C,\min}$. It is seen that the specimen in [4] is better than the JIS, but it is more desirable to use larger adherend thickness.

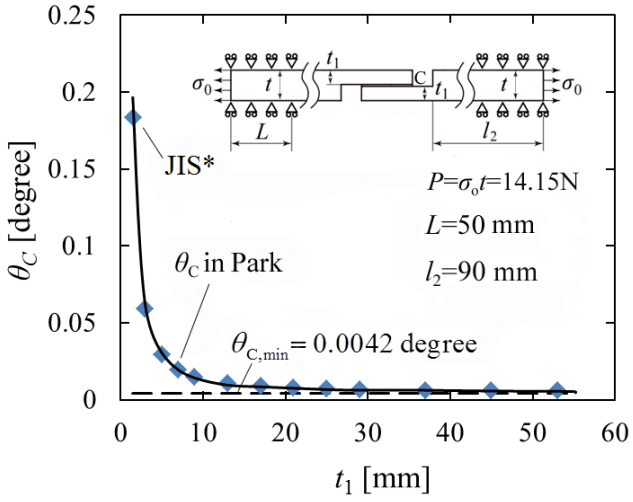

Fig.6.10 Effect of adherend thickness t_1 on deformation angle θ_C

Fig. 6.11 shows the results of deformation angle θ_C with different adherend lengths l_2 and adherend thicknesses t_1. The solid line shows the minimum value of θ_C. The θ_C increases with increasing l_2 when t_1=7mm. The values of θ_C are distributed around the solid line with slight variations when t_1=53mm. This means, when t_1 is large enough, the minimum θ_C can be obtained and the influence of l_2 on θ_C can be

ignored.

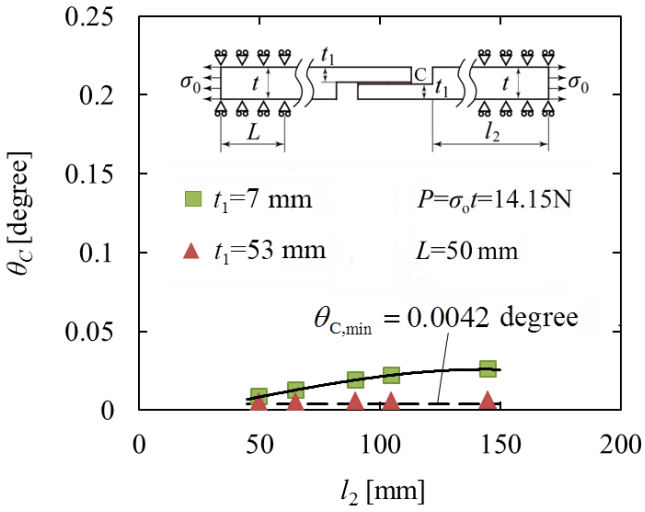

Fig.6.11 Effects of adherend length l_2 and adherend thickness t_1 on deformation angle θ_C

The relationship between θ_C and eccentric distance e for the model in Fig. 6.2(b) is plotted in Fig. 6.12. It is found that the θ_C decreases with increasing distance e, the influence of distance e on the θ_C is mainly reflected in the case of adherend thickness t_1=7mm. When t_1=25mm, the θ_C is almost constant independent of distance e.

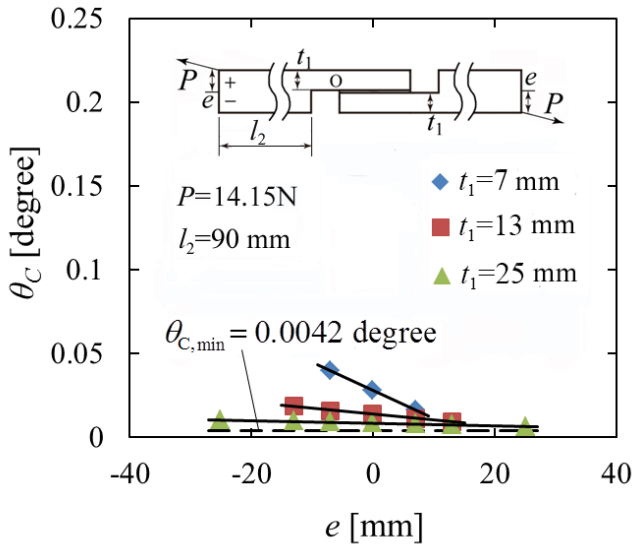

Fig.6.12 Effects of distance e and adherend thickness t_1 on deformation angle θ_C for the model in Fig. 6.2(b)

From the comparison between Figs. 6.3-6.5, 6.7 and Figs. 6.9-6.12, no significant different can be seen for the variation trend between the K_{σ,λ_1} and θ_C.

Fig. 6.13 shows the results of ISSF K_{σ,λ_1} and deformation angle θ_C for all of the models presented in this chapter. As can be seen from this figure, the K_{σ,λ_1} decreases with decreasing θ_C. This means that the changing of the ISSF can be explained by the deformation angle at the interface corner. Here, when adherend thickness t_1=1.5mm (JIS*), the K_{σ,λ_1} and θ_C are very large. The minimum K_{σ,λ_1} and θ_C can be obtained when the adherend thickness t_1 is large enough ($t_1 \geq 25$mm). It is seen that the bend effect is minimized when $t_1 \geq 25$mm. The possible reason of minimum $K_{\sigma,\lambda_1} \neq 0$ is the existence of local surface deformation at the interface corner even for very large thickness. Therefore, it is necessary to use the specimen with thick adherend thickness.

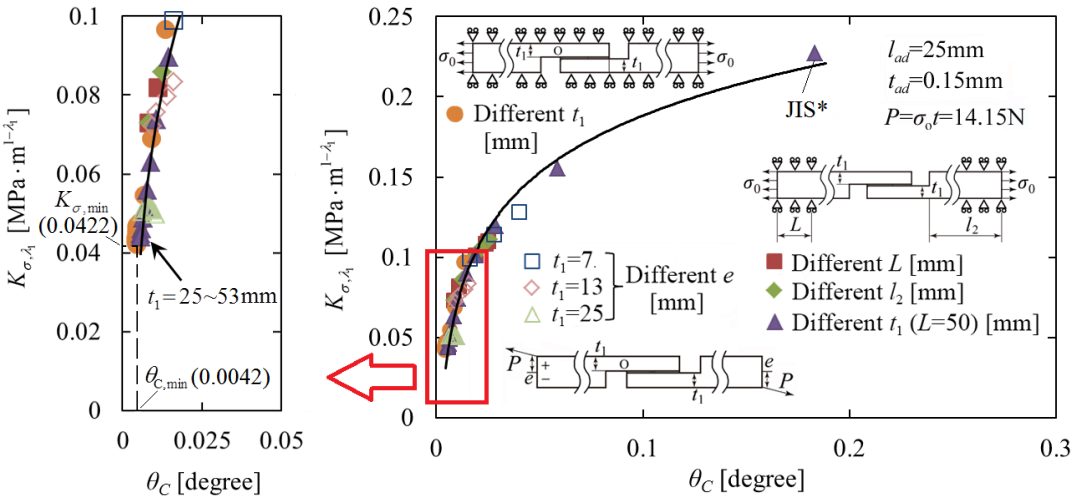

Fig.6.13 Relationship between K_{σ,λ_1} and θ_C.

6.4 How to obtain the adhesive strength for double lap joint by using single lap joint

The experimental results show that the shear strength of double lap joint is nearly twice larger than the one of single lap joint (see Fig.6.14(a)) [2]. However, the critical ISSF $K_{\sigma c}$ of the single lap joint is almost the same as the $K_{\sigma c}$ of double lap joint (see Fig.6.14(b)). Therefore, in this chapter, the equivalent conditions of strength for the double lap joint and single lap joint in Fig. 6.15 are considered in terms of the ISSF K_{σ,λ_1}. Here, based on the conclusions in chapter 6.3, the effect of the adherend thickness on K_{σ,λ_1} is considered.

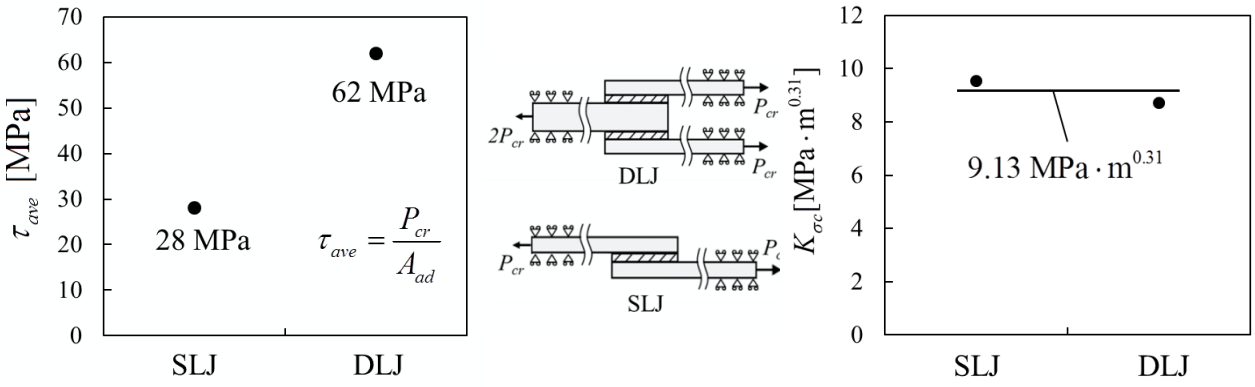

Fig.6.14 (a) Average shear strengths of single lap joint (SLJ) and double lap joint (DLJ), (b) $K_{\sigma c}$ of single lap joint (SLJ) and double lap joint (DLJ) (Adherend: S45C, Adhesive: Epoxy B).

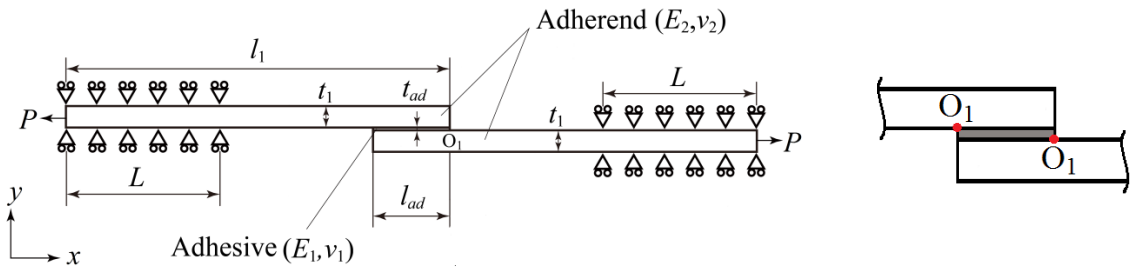

(a) Single lap joint (without tab)

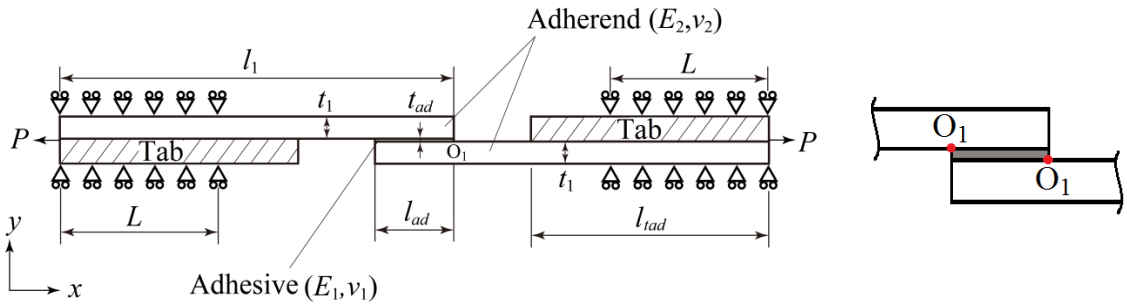

(b) Single lap joint (with tab)

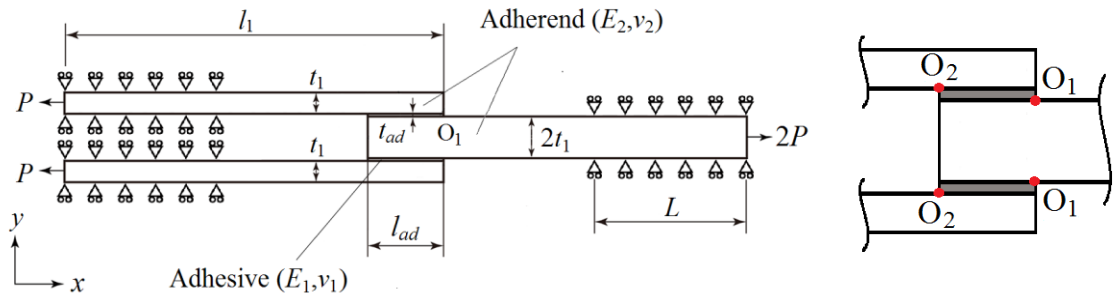

(c) Double lap joint (without tab)

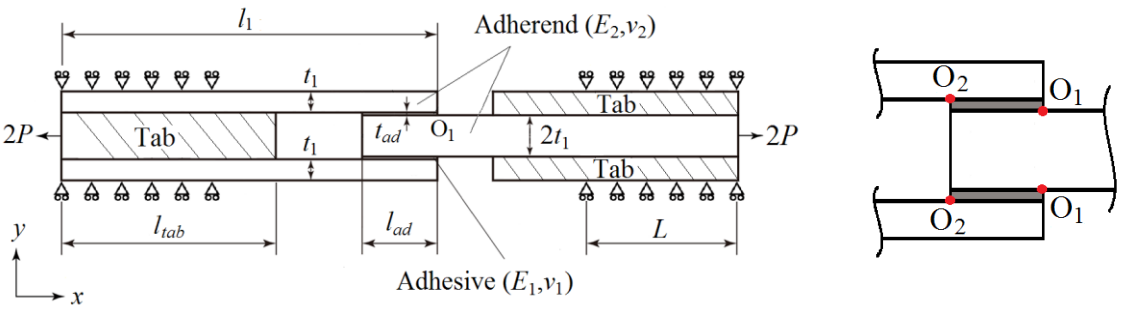

(d) Double lap joint (with tab)

Fig.6.15 Analysis models of lap joints

In this chapter, for single lap joint, all the two interface corners are marked as corner "O_1" because of its symmetry. For double lap joint, because the ISSFs at the two interface corners are different, the two corners are marked as corner "O_1" and "O_2", respectively. In addition, since end tab is often bonded at the ends of experimental specimens to reduce bend effect and reduce offset in the grips when loaded, the influence of the tab on K_{σ,λ_1} is also considered in this chapter. The same material as adherend is used for tab.

Fig. 6.16 shows the results of K_{σ,λ_1} at interface corners O_1 and O_2. It is found that the K_{σ,λ_1} at corner O_1 is larger than that at corner O_2. When adherend thickness t_1 =53mm, the K_{σ,λ_1} at corner O_2 is nearly equal to the K_{σ,λ_1} at corner O_1. The K_{σ,λ_1} for the specimen with tab is nearly equal to the K_{σ,λ_1} for the specimen without tab. Therefore, the fracture may occur at corner O_1 during testing. For this reason, the equivalent conditions of strength for single lap joint and double lap joint will be considered by using the K_{σ,λ_1} at interface corner O_1.

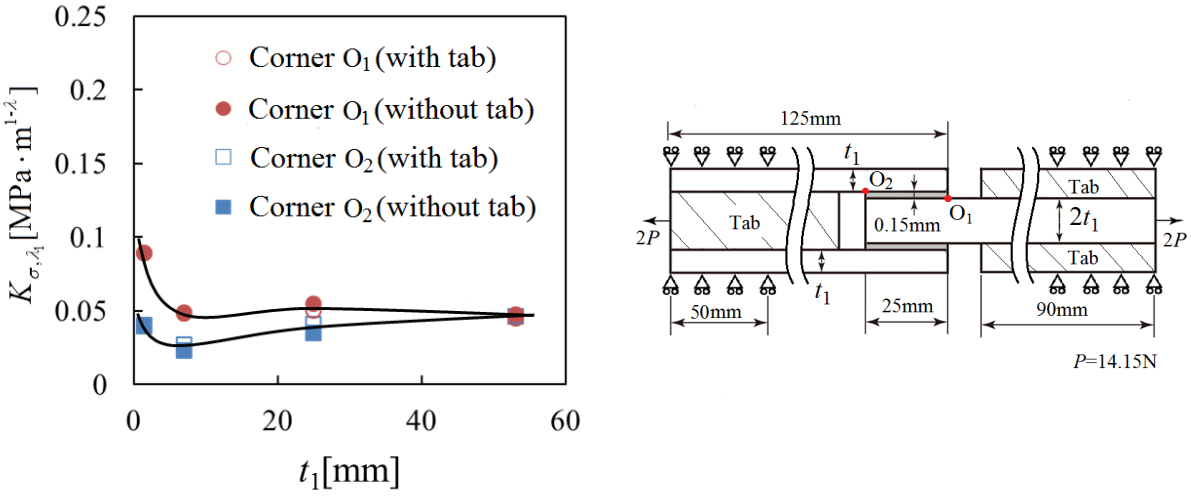

Fig.6.16 Results of K_{σ,λ_1} for double lap joint (see Fig. 6.14(c),(d))

Fig. 6.17 shows the results of K_{σ,λ_1} at interface corner O_1 with different adherend thicknesses t_1 for single lap joint and double lap joint. It is found that the K_{σ,λ_1} decreases with increasing adherend thickness t_1. When $t_1 \geq 25$mm, the K_{σ,λ_1} is almost constant independent of the t_1. In JIS, the adherend thickness t_1=1.5mm. The strength of single lap joint with t_1=7mm is nearly equal to that of double lap joint with t_1 =1.5mm (JIS) since the ISSFs of single lap joint and double lap joint are nearly the same. For the same reason, the strength of single lap joint is nearly equal to that of double lap joint when $t_1 \geq 25$mm.

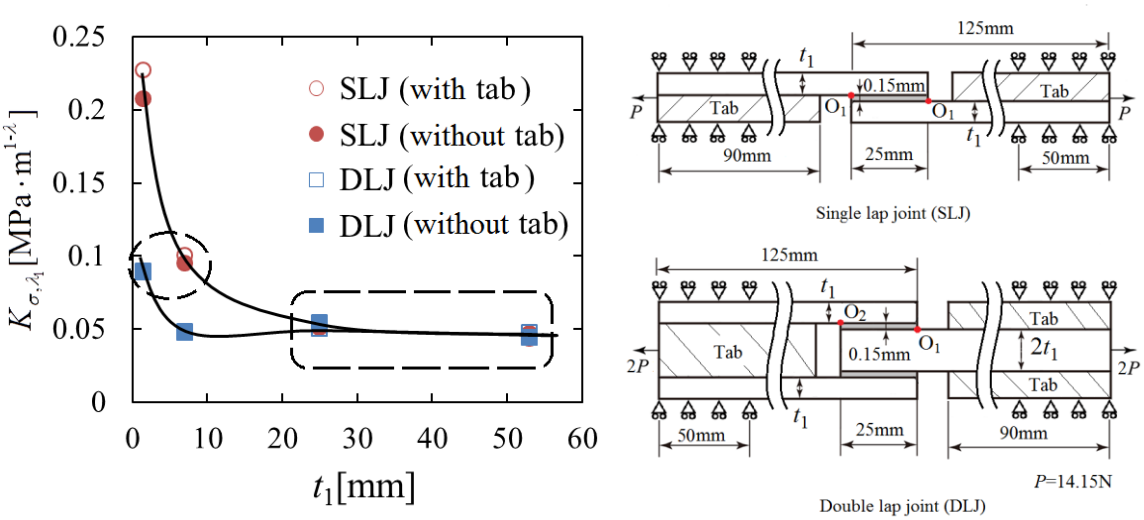

Fig.6.17 Comparison of single lap joint (SLJ) and double lap joint (DLJ)

When adherend thickness t_1≥25mm, the minimum K_{σ,λ_1} can be obtained and the minimum K_{σ,λ_1}≈0. At that time, the bend effect is minimized, the possible reason of minimum $K_{\sigma,\lambda_1} \neq 0$ is the existence of local surface deformation at the interface corner even for very large thickness. The deformations of the lap joints in Fig.6.17 (without tab) are shown in Fig. 6.18. Here, the deformation magnification is 300. As can be seen from Fig.6.18(a), when t_1=1.5, the bend deformation of single lap joint is large. When t_1 =7mm, the bend deformation of single lap joint is already small, and the deformation of single lap joint with t_1=7mm is nearly same as that of double lap joint with t_1=1.5mm (see Fig.6.18(b),(c)). When t_1≥25mm, the deformations of the lap joints are nearly the same, and there is only local surface deformation in lap joints (see Figs.6.18(e)~(h)).

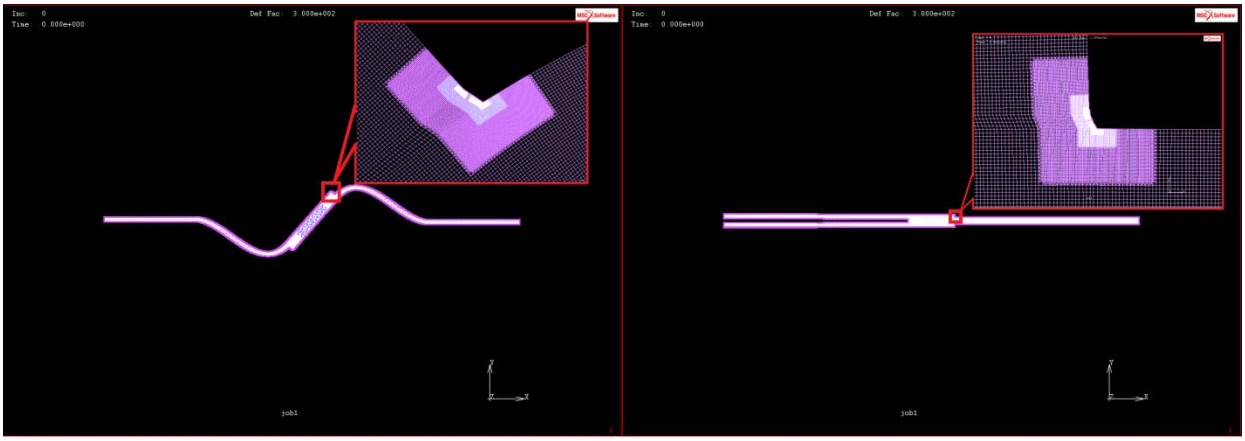

(a) SLJ with t_1=1.5mm (b) DLJ with t_1=1.5mm

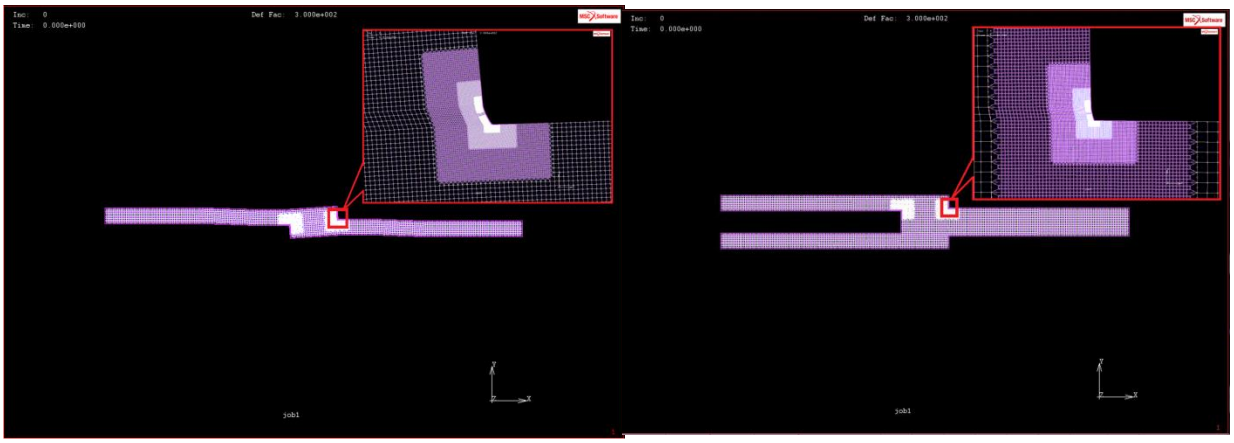

(c) SLJ with t_1=7mm (d) DLJ with t_1=7mm

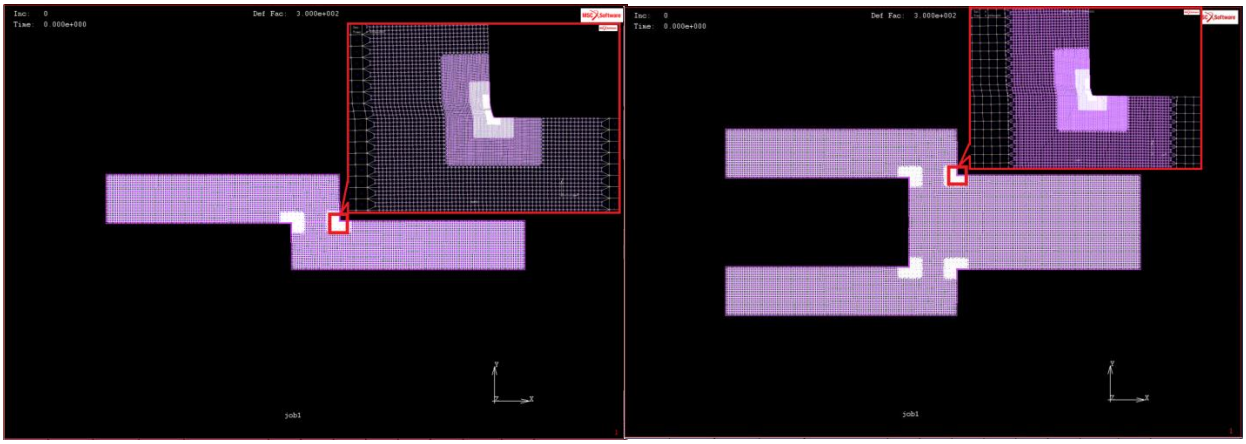

(e) SLJ with t_1=25mm (f) DLJ with t_1=25mm

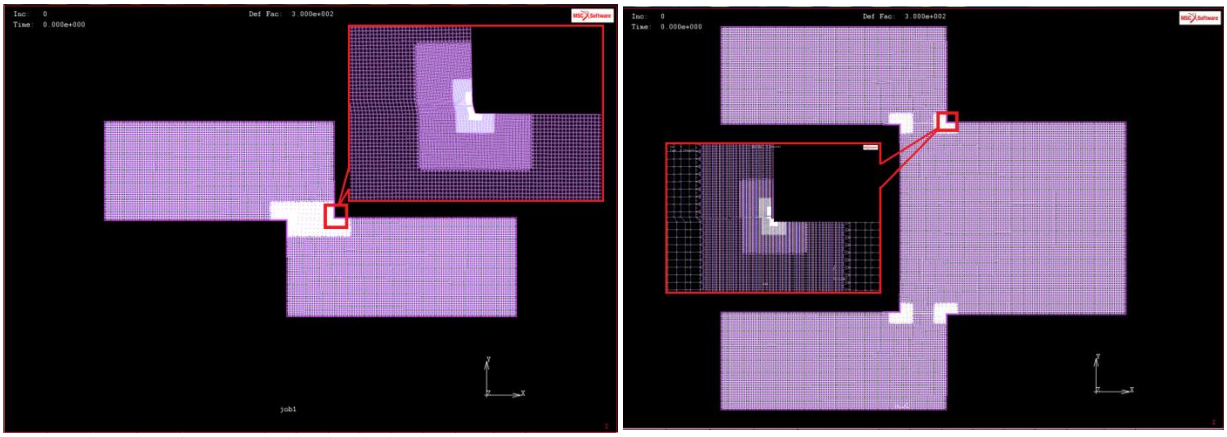

(g) SLJ with t_1=53mm (h) DLJ with t_1=53mm

Fig.6.18 Deformations of lap joints in Fig.6.17

6.5 Conclusion

In this study, the adhesive strength evaluation method to minimize bend effect for single lap joint is considered in terms of ISSF. The conclusions can be summarized in the following way.

(1) In order to minimize K_{σ,λ_1}, the effect of specimen geometry is considered under the same adhesive geometry and load P. The results show that the K_{σ,λ_1} decreases with increasing adherend thickness t_1. The minimum K_{σ,λ_1} can be obtained when the adherend thickness t_1 is large enough.

(2) The relationship between K_{σ,λ_1} and deformation angle at the interface corner is investigated under the same adhesive geometry and load P. It is found that the K_{σ,λ_1} decreases with decreasing θ_C, the minimum K_{σ,λ_1} and θ_C can be obtained when the adherend thickness t_1 is large enough. The changing of the ISSF can be explained by the deformation angle at the interface corner.

(3) The strength of single lap joint with adherend thickness t_1=7mm is nearly equal to that of double lap joint with t_1=1.5mm (JIS) since the ISSFs of singe lap joint and

double are nearly the same. When $t_1 \geq 25$mm, the strength of single lap joint is nearly equal to that of double lap joint.

6.6 References

[1] JIS K6850:1999, Adhesives-Determination of tensile lap-shear strength of rigid-to-rigid bonded assemblies [in Japanese].

[2] Ikegami K, Kyogoku H, Kawagoe H, Sugibayashi T, Nono K, Fujii T, Motoie K, Yoshida F. Benchmark tests on adhesive strengths in butt, single and double lap joints and double-cantilever beams. J Adhes Soc Jpn A 1997; 63(608):174-181 [in Japanese].

[3] Nakajima A, Saito M, Hino H, Nishi K, Suzuki Y, Kodaka A. Experimental study on fundamental strength characteristics of adhesive connection between steel members. J Adhes Soc Jpn 2011; 47(2): 53-59 [in Japanese].

[4] Park JH, Choi JH, Kweon JH. Evaluating the strengths of thick aluminum -to-aluminum joints with different adhesive lengths and thicknesses, Compos Struct 2010; 92: 2226-2235.

Chapter 7 Conclusions

Adhesively bonded joints are economical, practical and easy to make; thus they have been widely used in a variety of industries. The testing method for the adhesive strength of lap joints are standardized by Japanese Industrial Standards (JIS). However, the debonding strength is affected by the specimen dimension and difficult to be applied to other geometries. Compared with double lap joint, single lap joint can be used conveniently. However, the experimental results show that the strength of double lap joint is nearly twice larger than the one of single lap joint. Therefore, it is necessary to find a suitable evaluation method for lap joint testing. The single lap joint testing should be done under pure shear loading, but pure shear testing is difficult to be realized in the experiment. Due to the bend deformation of single lap joint during testing, the peeling force is applied to the adhesive region. Then the intensity of singular stress field (ISSF) at the interface corner is affected by the peeling force due to the deformation. This research concentrated on the adhesive strength evaluation method to minimize the ISSF for single lap joint. The following conclusions have been obtained as follows.

(1) In chapter 3, several types of adhesive joints for butt joint are considered in terms of the intensity of singular stress at the interface corner with and without fictitious crack. The conclusions can be summarized in the following way.

1. The corner stress intensity factors K_σ can be obtained conveniently by using the analysis method presented. Then the adhesive strength σ_c for various butt joints can be evaluated as $K_{\sigma c}$ =const for carbon steel/epoxy resin, aluminum/araldite, and brass/solder. As well as the results of Suzuki for carbon steel/epoxy resin, whose specimens are carefully prepared to exclude the defect

and residual strain, other experimental results can be expressed as the critical stress intensity factor $K_{\sigma c}$=const.

2. The interface intensity factors K_I and K_{II} can be obtained conveniently by using the analysis method presented. Then the adhesive strength σ_c for various butt joints can be evaluated as K_{IC}=const assuming fictitious crack modeling.
3. The usefulness of the fictitious crack modeling was highlighted by taking an example of sharp V-notch problems. Although different notch opening angle has distinct singular index, the static strength of notched acrylic resin can be expressed as K_{IC}=const. The suitable fictitious crack length is found to be a = 0.02-0.16mm on the basis of the criterion when the fracture occurs at the crack tip as $K_I\big|_{r=a} \geq K_{IC}$.
4. The relationship between the critical value of interface stress intensity factor K_{IC} and critical value of corner stress intensity factor $K_{\sigma c}$ is considered. The relation $K_{IC} \propto a^{\lambda-0.5} K_{\sigma c}$ can be derived for the fictitious crack length $a/W \leq 0.01$.
5. The suitable dimension for fictitious crack was discussed for butt joints. The applicability should be confirmed in the further studies for other types of joint geometries.

(2) In chapter 4, a convenient analysis method of adhesive strength of lap joint is presented based on the ISSF. The conclusions can be summarized in the following way.

1. A convenient analysis method of adhesive strength is presented in terms of the ISSF. In this method, the same mesh pattern is applied to the unknown

problems and the reference problems by focusing on the FEM stress at the interface corner.

2. Although the singular stress is controlled by two factors for lap joints, it is found that the debonding condition can be expressed almost in the same way even if the adhesive geometries are widely changed. Therefore, the ISSF of lap joints as well as butt joints can be obtained conveniently by using the analysis method presented in this paper.
3. The usefulness of the present solution is verified by comparing with the results of the conventional method (RWCIM). Since RWCIM requires the complex and difficult calculations such as matrix operation and numerical integration, the proposed method is found to be very convenient and practical to determine ISSF.

(3) In chapter 5, the debonding fracture criterion for the single lap joint is examined with varying the adhesive length and adhesive length. The conclusions can be summarized in the following way.

1. The adhesive strength of single lap joint is discussed in terms of critical ISSF $K_{\sigma c}$. The values of critical ISSF $K_{\sigma c}$ can be calculated by using the method presented in chapter 4.
2. Based on the obtained ISSF, the debonding criterion is examined with varying the adhesive geometries. The results show that the adhesive strength for single lap joint can be evaluated as $K_{\sigma c}$=const when the debonding fracture occurs (except for the specimen with very short adhesive length).

(4) In chapter 6, the adhesive strength evaluation method to minimize bend effect for single lap joint is presented. The conclusions can be summarized in the following

way.

1. In order to minimize K_{σ,λ_1}, the effect of specimen geometry is considered under the same adhesive geometry and load P. The results show that the K_{σ,λ_1} decreases with increasing adherend thickness t_1. The minimum K_{σ,λ_1} can be obtained when the adherend thickness t_1 is large enough.
2. The relationship between K_{σ,λ_1} and deformation angle at the interface corner is investigated under the same adhesive geometry and load P. It is found that the K_{σ,λ_1} decreases with decreasing θ_C, the minimum K_{σ,λ_1} and θ_C can be obtained when the adherend thickness t_1 is large enough. The changing of the ISSF can be explained by the deformation angle at the interface corner.
3. The strength of single lap joint with adherend thickness t_1=7mm is nearly equal to that of double lap joint with t_1=1.5mm (JIS) since the ISSFs of singe lap joint and double are nearly the same. When $t_1 \geq 25$mm, the strength of single lap joint is nearly equal to that of double lap joint.

Acknowledgements

First of all, I would like to give the ultimate thanks to my dissertation supervisor Professor Nao-Aki Noda for his guidance, encouragement, and for helping me complete my work. He has been endowing me detailed direction and dedicating academic help along the process of dissertation. Without his consistent and enthusiastic help, this thesis could not have reached its present form.

I am also deeply grateful to Prof. Tatsujiro MIYAZAKI for his detailed and valuable suggestions in my PhD study. In addition, I would like to express my gratitude to Dr. Yoshikazu SANO for his kindly help and precious suggestions through the last four years. Moreover, my gratitude should direct to Dr Yasushi TAKASE, who has been supporting and helping me throughout my doctoral program.

My sincere gratitude also goes to my doctoral committee members, Prof. Tetsuya AKIYAMA, Prof. Yasuhiro AKAHOSHI, Prof. Kenji MATSUDA, for their insightful comments and suggestions on my research. I would also like to thank all Fracture Mechanics and Elasticity lab-mates, all of Kyushu Institute of Technology's professors and administrative staff, and all those who have helped me carry out my work.

My first advisor, Prof. Bin LIANG, introduced me to the field to the engineering mechanics and introduced me to the study in Japan. I would like to express my gratitude for his constantly encouragement and help in the past few years. All of this makes me benefit a lot and contributes to my future work.

I would like to express my special gratitude to my husband and my family who have been given me continuous support and encouragement in the past few years. There are

no words to express my gratitude to my parents; they have been the source of energy for me. In addition, my gratitude also goes to all of my friends. Thanks for their accompanying and helping.

Finally, I would like to express the deepest gratitude to the financial support of MEXT scholarship of the Japanese government. It made the possible for the successful completion of my research.

Appendix A. Corner stress intensity factor for bonded strip under arbitrary material combinations

In this paper, the dimensionless corner stress intensity factor F_σ for the perfectly-bonded strip in chapter 3 was obtained from our previous study [1]. The analytical values of F_σ are listed as follows.

Table A.1 indicate the results for bonded strip in Fig. 3.2(d), which are equivalent to the case $h/W \geq 1$. Using the results $F_\sigma|_{h/W=1}$ in Table A.1 and $F_\sigma / F_\sigma|_{h/W=1}$ in Table A.2, F_σ are obtained and shown in Fig. A.1 for $h/W = 0.001$ and $h/W = 0.1$. From those results the critical values of the corner stress intensity factor $K_{\sigma c}$ can be obtained.

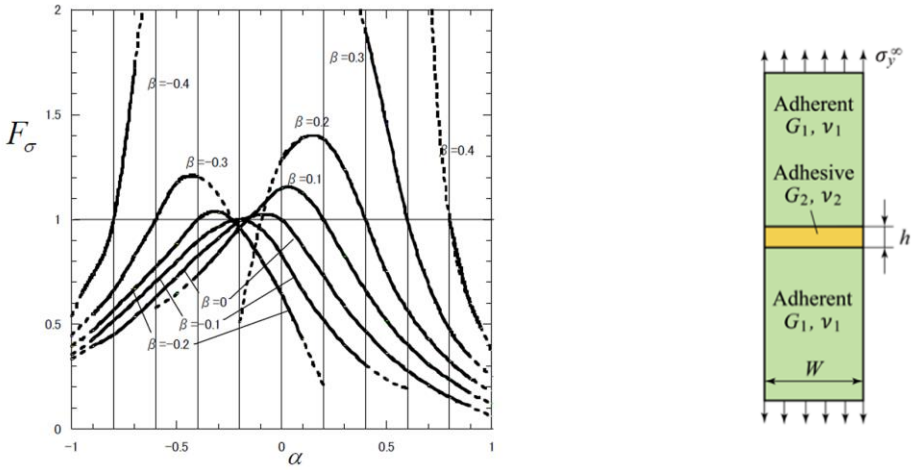

(a)

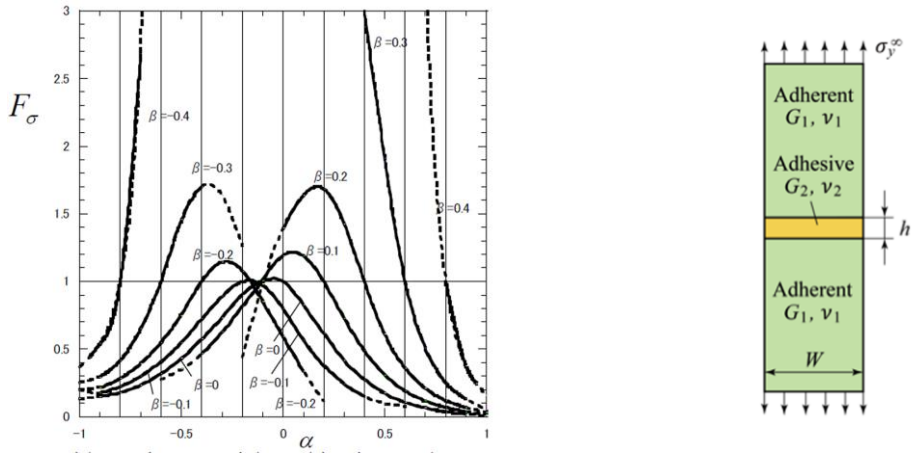

(b)

Fig.A.1 F_σ with varying material combination β when (a) $h/W = 0.001$; (b) $h/W = 0.1$

Table A.1 $F_\sigma|_{h/W=1}$ at interface edge point in bonded finite plate

[underlined figures indicate λ <1, **bold** figures indicate λ >1, standard style figures indicate λ =1]

α	$\beta=-0.4$	$\beta=-0.3$	$\beta=-0.2$	$\beta=-0.1$	$\beta=0$	$\beta=0.1$	$\beta=0.2$	$\beta=0.3$	$\beta=0.4$
1.0	0.540	0.446	0.395	0.357	0.332				
-0.95	0.643	0.491	0.422	0.381	0.349				
-0.9	0.726	0.534	0.456	0.412	0.381				
-0.8	1.000	0.636	0.538	0.487	0.45				
-0.7	**1.855**	0.800	0.626	0.558	0.486				
-0.6	**3.291**	1.000	0.724	0.638	0.559	0.505			
-0.5		**1.264**	0.842	0.722	0.635	0.551			
-0.4		**1.467**	1.000	0.822	0.718	0.615			
-0.3		**1.609**	**1.118**	0.913	0.796	0.697			
-0.2		**1.690**	**1.153**	1.000	0.889	0.797	0.404		
-0.1			**1.103**	**1.037**	0.955	0.890	0.767		
0			1.000	1.000	1.000	1.000	1.000		
0.1			0.767	0.890	0.955	**1.037**	**1.103**		
0.2			0.404	0.797	0.889	1.000	**1.153**	**1.690**	
0.3				0.697	0.796	0.913	**1.118**	**1.609**	
0.4				0.615	0.718	0.822	1.000	**1.467**	
0.5				0.551	0.635	0.722	0.842	**1.264**	
0.6				0.505	0.559	0.638	0.724	1.000	**3.291**
0.7					0.486	0.558	0.626	0.800	**1.855**
0.8					0.450	0.487	0.538	0.636	1.000
0.9					0.381	0.412	0.456	0.534	0.726
0.95					0.349	0.381	0.422	0.491	0.643
1.0					0.332	0.357	0.395	0.446	0.540

Table A.2 $F_\sigma / F_\sigma|_{h/W=1}$ with varying α and β when (a) $h/W = 0.001$; (b) $h/W = 0.1$.

(a) $h/W = 0.001$ (Note that $F_\sigma / F_\sigma|_{h/W=1} = 1$ when $\alpha = 2\beta$) [underlined figures indicate λ <1, **bold** figures indicate λ >1, standard style figures indicate λ =1]

α	$\beta=-0.4$	$\beta=-0.3$	$\beta=-0.2$	$\beta=-0.1$	$\beta=0$	$\beta=0.1$	$\beta=0.2$	$\beta=0.3$	$\beta=0.4$
-1.0	0.682	0.566	0.517	0.552	0.400				
-0.95	0.6864	0.5554	0.4957	0.4629	0.400				
-0.9	0.7420	0.5533	0.4722	0.4252	0.4004				
-0.8	1.0000	0.6535	0.5254	0.4587	0.4190				
-0.7	**1.4465**	0.8130	0.6289	0.5356	0.4812				
-0.6	**2.073**	1.0000	0.7579	0.6390	0.5690	0.550			
-0.5		**1.1509**	0.8952	0.7587	0.6769	0.6297			
-0.4		**1.1613**	1.0000	0.8794	0.7988	0.7530			
-0.3		**1.0165**	**1.0232**	0.9725	0.9205	0.8924			
-0.2		**0.750**	**0.9346**	1.0000	1.0169	1.0203	1.100		
-0.1			**0.7716**	**0.9372**	1.0526	1.1374	1.280		
0			0.5912	0.7994	1.0000	1.1925	1.3925		
0.1			0.4363	0.6331	0.8665	**1.1473**	**1.4837**		
0.2			0.300	0.4768	0.6938	1.0000	**1.4608**	**2.524**	
0.3				0.3477	0.5253	0.7974	**1.2786**	**2.443**	
0.4				0.2478	0.3834	0.5962	1.0000	**2.0311**	
0.5				0.1728	0.2729	0.4281	0.7223	**1.5100**	
0.6				0.150	0.1904	0.2996	0.4984	1.0000	**2.857**
0.7					0.1297	0.2058	0.3355	0.6323	**1.825**
0.8					0.0852	0.1388	0.2224	0.3942	1.0000
0.9					0.0511	0.0913	0.1456	0.2448	0.5173
0.95					0.0348	0.0725	0.1172	0.1930	0.3806
1.0					0.025	0.050	0.080	0.110	0.300

(b) $h/W = 0.1$ (Note that $F_\sigma / F_\sigma|_{h/W=1} = 1$ when $\alpha = 2\beta$) [underlined figures indicate λ <1, **bold** figures indicate λ >1, standard style figures indicate λ =1]

α	$\beta=-0.4$	$\beta=-0.3$	$\beta=-0.2$	$\beta=-0.1$	$\beta=0$	$\beta=0.1$	$\beta=0.2$	$\beta=0.3$	$\beta=0.4$
-1	1.000	1.000	1.000	1.000	1.000				
-0.95	1.0099	1.0143	1.0164	1.0177	1.018				
-0.9	1.0144	1.0260	1.0312	1.0342	1.0365				
-0.8	1.0000	1.0390	1.0548	1.0637	1.0698				
-0.7	**0.9275**	1.0333	1.0681	1.0870	1.0993				
-0.6	**0.764**	1.0000	1.0671	1.1018	1.1239	1.150			
-0.5		**0.9298**	1.0462	1.1048	1.1415	1.1686			
-0.4		**0.8228**	1.0000	1.0916	1.1491	1.1910			
-0.3		**0.6943**	**0.9269**	1.0575	1.1426	1.2051			
-0.2		**0.552**	**0.8345**	1.0000	1.1175	1.2051	1.260		
-0.1			**0.7361**	**0.9219**	1.0698	1.1890	1.280		
0			0.6433	0.8324	1.0000	1.1501	1.2864		
0.1			0.5579	0.7413	0.9144	**1.0856**	**1.2580**		
0.2			0.513	0.6548	0.8229	1.0000	**1.1994**	**1.453**	
0.3				0.5748	0.7332	0.9037	**1.1092**	**1.409**	
0.4				0.5007	0.6492	0.8071	1.0000	**1.2962**	
0.5				0.4307	0.5715	0.7160	0.8879	**1.1518**	
0.6				0.382	0.4994	0.6324	0.7828	1.0000	**1.498**
0.7					0.4309	0.5561	0.6882	0.8635	**1.224**
0.8					0.3625	0.4855	0.6040	0.7467	1.0000
0.9					0.2851	0.4180	0.5291	0.6479	0.8241
0.95					0.2329	0.3836	0.4947	0.6046	0.7544
1.0					0.185	0.339	0.463	0.560	0.697

References:

[1] Zhang Y, Noda NA, Wu PZ, Duan ML. A mesh-independent technique to evaluate stress singularities in adhesive joints. Int J Adhes Adhes 2015; 57:105–117; the corrigendum of authorship is published in Int J Adhes Adhes 2015; 60:130.

Appendix B. Interface stress intensity factors for shallow interface crack under arbitrary material combinations

In this study, the suitable length of the fictitious crack was discussed through interface stress intensity factor based on our previous study [1]. In that paper, the interface stress intensity factors for the shallow edge interface cracks in a bonded strip as shown in Fig.B.1 were investigated.

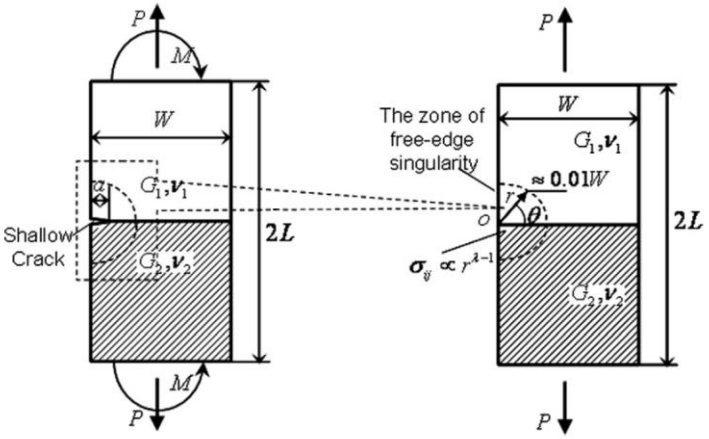

Fig.B.1 Shallow edge interface crack in a bonded strip

The dimensionless interface stress intensity factors F_I and F_{II} are often used to express the results of analysis. However, for the bonded semi-infinite plate ($a/W \to 0$), when $\alpha(\alpha-2\beta)>0$, $F_I \to \infty$ and $F_{II} \to \infty$; when $\alpha(\alpha-2\beta)<0$, $F_I \to 0$ and $F_{II} \to 0$. Therefore, F_I and F_{II} are not suitable for edge interface cracks.

However, as indicated in Fig.B.2, $C_I = F_I/(W/a)^{1-\lambda}$ and $C_{II} = F_{II}/(W/a)^{1-\lambda}$ always have finite values when $a/W \to 0$.

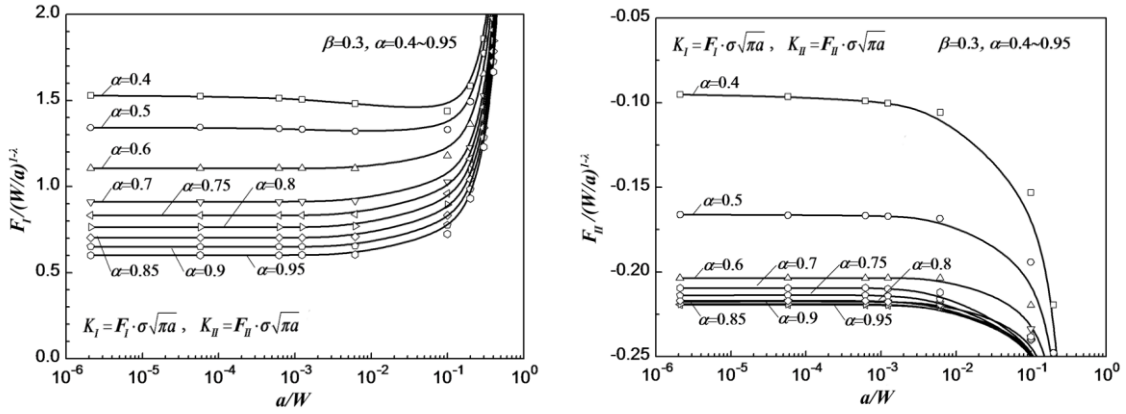

(a) (b)

Fig.B.2 The values of $F_I/(W/a)^{1-\lambda}$ and $F_{II}/(W/a)^{1-\lambda}$ for $\beta = 0.3$

Furthermore, the coefficients C_I and C_{II} are constants depending on the material combination. The results for the two coefficients are plotted and listed in Fig. B.3(a) and Table.B.1 as well as in Fig. B.3(b) and Table.B.2, respectively.

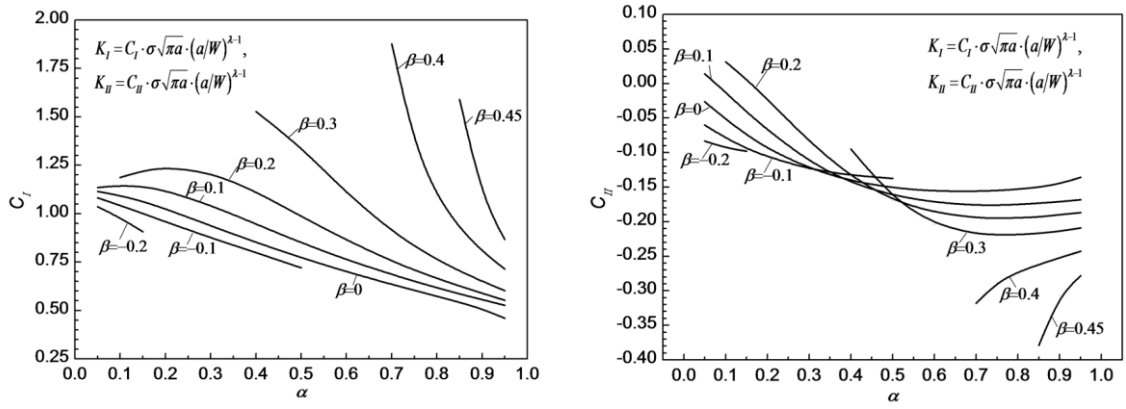

(a) (b)

Fig.B.3 The values of C_I and C_{II} for various combination of materials

Table B.1 Tabulated values of C_I

α	$\beta=-0.2$	$\beta=-0.1$	$\beta=0$	$\beta=0.1$	$\beta=0.2$	$\beta=0.3$	$\beta=0.4$	$\beta=0.45$
0.05	1.036	1.082	1.114	1.136				
0.1	0.979	1.043	1.094	1.146	1.187			
0.15	0.907	1.001	1.063	1.14	1.221			
0.2		0.958	1.025	1.12	1.24			
0.3		0.875	0.938	1.044	1.215			
0.4		0.798	0.852	0.947	1.115	1.528		
0.5		0.721	0.772	0.85	0.986	1.343		
0.6			0.7	0.763	0.863	1.106		
0.7			0.635	0.686	0.756	0.912	1.876	
0.75			0.604	0.651	0.709	0.833	1.356	
0.8			0.573	0.618	0.666	0.764	1.092	
0.85			0.542	0.586	0.626	0.704	0.925	1.589
0.9			0.508	0.556	0.588	0.65	0.806	1.083
0.95			0.46	0.527	0.553	0.602	0.715	0.867

Table B.2 Tabulated values of C_{II}

α	$\beta=-0.2$	$\beta=-0.1$	$\beta=0$	$\beta=0.1$	$\beta=0.2$	$\beta=0.3$	$\beta=0.4$	$\beta=0.45$
0.05	-0.083	-0.06	-0.026	0.014				
0.1	-0.093	-0.079	-0.052	-0.013	0.031			
0.15	-0.098	-0.094	-0.074	-0.041	0.006			
0.2		-0.106	-0.094	-0.067	-0.023			
0.3		-0.124	-0.123	-0.113	-0.084			
0.4		-0.133	-0.141	-0.144	-0.135	-0.095		
0.5		-0.137	-0.151	-0.162	-0.169	-0.166		
0.6			-0.156	-0.172	-0.187	-0.204		
0.7			-0.156	-0.176	-0.194	-0.218	-0.318	
0.75			-0.155	-0.176	-0.195	-0.219	-0.288	
0.8			-0.153	-0.175	-0.194	-0.219	-0.273	
0.85			-0.15	-0.173	-0.193	-0.217	-0.262	-0.379
0.9			-0.145	-0.171	-0.19	-0.214	-0.252	-0.307
0.95			-0.136	-0.168	-0.187	-0.209	-0.243	-0.278

The authors have indicated that the plus and minus of the slope of each value (F_I , F_{II}) is always controlled by the sign of $\alpha(\alpha-\beta)$ [1]. The results of the parameters in the $\alpha-\beta$ space for the various materials combinations shown in [2] are re-plotted in Fig. B.4 [1].

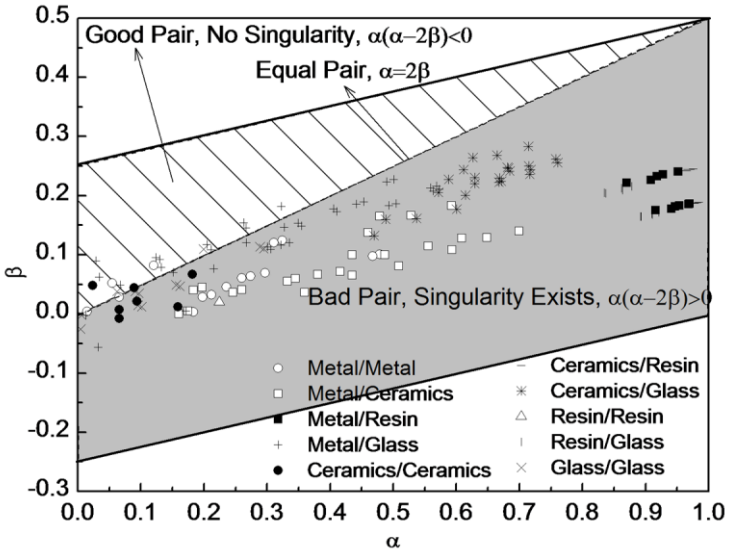

Fig.B.4 Dundurs' material composite parameters for several engineering materials

As can be seen from Fig. B.4, most material combinations are located in the "bad pair" region. However, metal/glass, metal/metal, ceramics/ceramics and glass/glass joints can be found in the "good pair" region.

References:

[1] Noda NA, Lan X. Stress intensity factors for an edge interface crack in a bonded semi-infinite plate for arbitrary material combination. Int J Solids Struct 2012;49(10):1241–51.

[2] Yuuki R. Mechanics of interface. 1st ed. Baifuukann, Tokyo; 1992 [in Japanese].

Appendix C. Singular index for lap joints

Table C.1 Singular index for lap joints λ $(0 < \mathrm{Re}(\lambda) < 1)$. [underlined figure indicate multiple root, **bold** figure indicate complex root, standard style figure indicate real root]

α	$\beta=-0.5$	$\beta=-0.4$	$\beta=-0.3$	$\beta=-0.2$	$\beta=-0.1$	$\beta=0$	$\beta=0.1$	$\beta=0.2$	$\beta=0.3$	$\beta=0.4$	$\beta=0.5$
-1	Non	0.807313	0.720529	0.664609	0.624659	0.594612					
-0.9		0.800102	0.713270	0.657967	0.618663	0.589223					
		0.997323	0.998666	0.999111	0.999333	0.999467					
-0.8		0.794890	0.706604	0.651598	0.612819	0.583934					
		0.988598	0.994363	0.996246	0.997185	0.997748					
-0.7			0.700535	0.645489	0.607116	0.578738					
			0.986584	0.991068	0.993300	0.994638					
-0.6			0.695095	0.639636	0.601547	0.573629	0.552526				
			0.974790	0.983193	0.987375	0.989886	0.991563				
-0.5			0.690364	0.634041	0.596104	0.568599	0.548004				
			0.958485	0.972217	0.979070	0.983201	0.985967				
-0.4			0.686483	0.628716	0.590782	0.563645	0.543552				
			0.937298	0.957761	0.968020	0.974246	0.978436				
-0.3			0.683711	0.623685	0.585580	0.558760	0.539167				
			0.911000	0.939524	0.953867	0.962655	0.968617				
-0.2			0.682542	0.618989	0.580497	0.553941	0.534851	0.521047			
			0.879395	0.917337	0.936302	0.948055	0.956113	0.961997			
-0.1				0.614698	0.575537	0.549184	0.530605	0.517475			
				0.891188	0.915116	0.930101	0.940505	0.948184			
0				0.610930	0.570707	0.544484	0.526433	0.514038			
				0.861179	0.890238	0.908529	0.921385	0.930994			
0.1				0.607894	0.566022	0.539838	0.526433	0.514038			
				0.827429	0.861739	0.883194	0.921385	0.930994			
0.2				0.606003	0.561511	0.535243	0.518343	0.507703	0.501847		
				0.789888	0.829796	0.854095	0.871335	0.884461	0.894894		
0.3					0.557223	0.530697	0.514455	0.504921	0.500526		
					0.794628	0.821357	0.840068	0.854257	0.865522		
0.4					0.553253	0.526195	0.510710	0.502536	0.500000		
					0.756400	0.785186	0.804636	0.819026	0.830167		
0.5					0.549802	0.521736	0.507168	0.500757	0.500737		
					0.715108	0.745794	0.765131	0.778569	0.788128		
0.6					0.547386	0.517317	0.503944	0.500000	0.503736		
					0.670322	0.703330	0.721601	0.732578	0.738354		
0.7						0.512937	0.501301	0.501267	0.511773		
						0.657821	0.673870	0.680168	0.678146		
0.8						0.508591	0.500000	0.508067	0.544319	**0.570579**	
						0.609106	0.621093	0.617814	0.588069	**±0.0645534*i***	
0.9						0.504280	0.504147	**0.532822**	**0.534652**	**0.537138**	
						0.556769	0.558811	**±0.0339893*i***	**±0.072084*i***	**±0.108448*i***	
1						0.500000	**0.500000**	**0.500000**	**0.500000**	**0.500000**	**0.500000**
							±0.0319377*i*	**±0.0645318*i***	**±0.0985231*i***	**±0.134852*i***	**±0.174850*i***

Table C.1 shows singular index for lap joints λ within a range of $0 < \mathrm{Re}(\lambda) < 1$, where the underlined figure indicate the multiple root, the bold figure indicate the complex root, the standard style figure indicate the real root. The eigenequation (C.1) has real root, multiple real root or complex root depending on (α, β) except for no root at (α, β) = (-1, -0.5). Two real roots appear in most of the material combinations.

$$\begin{aligned} &4\sin^2(\pi\lambda)\left\{\sin^2\left(\frac{\pi\lambda}{2}\right)-\lambda^2\right\}\beta^2+4\lambda^2\sin^2(\pi\lambda)\alpha\beta+\left\{\sin^2\left(\frac{\pi\lambda}{2}\right)-\lambda^2\right\}\alpha^2-4\lambda^2\sin^2(\pi\lambda)\beta \\ &-2\left\{\lambda^2\cos(2\pi\lambda)+\sin^2\left(\frac{\pi\lambda}{2}\right)\cos(\pi\lambda)+\frac{1}{2}\sin^2(\pi\lambda)\right\}\alpha+\sin^2\left(\frac{3\pi}{2}\lambda\right)-\lambda^2=0 \end{aligned} \quad . \text{(C.1)}$$

Appendix D. Reference solutions obtained by using RWCIM

The reciprocal work contour integral method (RWCIM) is based on the Betti's reciprocal theorem. Fig. D.1 shows the integral path for RWCIM. The linear elastic analyses are performed under the plane strain condition by using the software MSC Marc. The contour integral path *C* in Fig. D.1 and the mesh pattern in Fig. D.2 are used in order to calculate the ISSF. By employing Williams' eigenfunction expansion method, the stress and the displacement in the vicinity of the interface corner edge are expressed as follows [1, 2].

$$\sigma_{ij} = \sum_{k=1}^{\infty} K_k \, f_{ij}(\theta, \lambda_k) \, r^{\lambda_k - 1} \tag{D.1}$$

$$u_i = \sum_{k=1}^{\infty} K_k \, g_i(\theta, \lambda_k) \, r^{\lambda_k} \tag{D.2}$$

Here, K_k is the coefficient obtained by RWCIM, f_{ij} and g_i are the eigenfunction related to the λ_k which depends on the angle θ. From Betti's reciprocal theorem, the following equation can be obtained [1, 2].

$$\oint_C \left(\sigma_{ij} u_i^* - \sigma_{ij}^* u_i\right) n_j \, ds = 0 \tag{D.3}$$

Here, n_j is normal vector of the boundary C, σ_{ij}^* and u_i^* are the complementary stress and displacement that satisfy the same equilibrium and constitutive relations as σ_{ij} and u_i, respectively. The stress σ_{ij}^* and displacement u_i^* can be expressed as follows [1, 2].

$$\sigma_{ij}^* = \sum_{k=1}^{\infty} K_k^* \, f_{ij}(\theta, \lambda_k^*) \, r^{\lambda_k^* - 1} = \sum_{k=1}^{\infty} K_k \, f_{ij}(\theta, -\lambda_k) \, r^{-\lambda_k - 1} \tag{D.4}$$

$$u_i^* = \sum_{k=1}^{\infty} K_k^* \, g_i(\theta, \lambda_k^*) \, r^{\lambda_k^*} = \sum_{k=1}^{\infty} K_k \, g_i(\theta, -\lambda_k) \, r^{-\lambda_k} \tag{D.5}$$

The integral path C $(= C_1 + C_2 + C_3 + C_4 + C_5 + C_6 + C_\varepsilon)$ is set as shown in Fig. 7. Because the lines C_1 and C_6 lie along the stress free surface, the integrals along these lines are zero. Therefore, Eq. (D.3) can be written as follows.

$$\int_{-\pi/2}^{\pi} \left(\sigma_{ij} u_i^* - \sigma_{ij}^* u_i\right) \varepsilon \, n_j \, d\theta = \int_{C'} \left(\sigma_{ij} u_i^* - \sigma_{ij}^* u_i\right) n_j \, ds \tag{D.6}$$

Here, $C' = C_2 + C_3 + C_4 + C_5$. The terms of σ_{ij} and u_i in the left hand side can be expressed as Eqs. (D.1) and (D.2). The complementary stress and displacement calculated by FEM, $\sigma_{ij,FEM}$ and $u_{i,FEM}$ are substituted into the terms of σ_{ij} and u_i in the right hand side. Then, σ_{ij}^* and u_i^* are given by Eqs. (D.4) and (D.5), respectively. When $\varepsilon \to 0$, the integral in the left hand side becomes constant. The following equation is used as K_k^* [1, 2].

$$1/K_k^* = \int_{-\pi/2}^{\pi} \left[f_{ij}(\theta, \lambda_k) \, g_i^*(\theta, \lambda_k^*) - f_{ij}^*(\theta, \lambda_k^*) \, g_i(\theta, \lambda_k)\right] n_j \, d\theta \tag{D.7}$$

The ISSF K_k can be obtained from the following equation.

$$K_k = \int_{C'} \left(\sigma_{ij,FEM} u_{ik}^* - \sigma_{ijk}^* u_{i,FEM}\right) n_j \, ds \tag{D.8}$$

Here, $\sigma_{ijk}^* = K_k^* \, f_{ij}(\theta, \lambda_k) \, r^{\lambda_k^* - 1}$, $u_{ik}^* = K_k^* \, g_i(\theta, \lambda_k) \, r^{\lambda_k^*}$. RWCIM is useful for determining the ISSF.

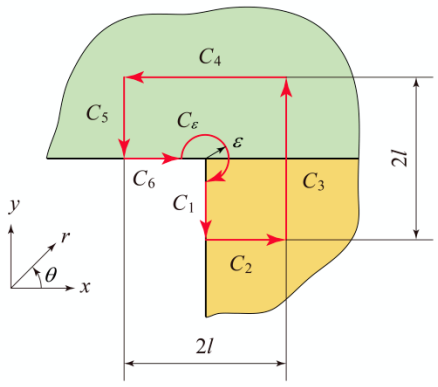

Fig.D.1 Integral path C for RWCIM ($C = C_1 + C_2 + C_3 + C_4 + C_5 + C_6 + C_\varepsilon$).

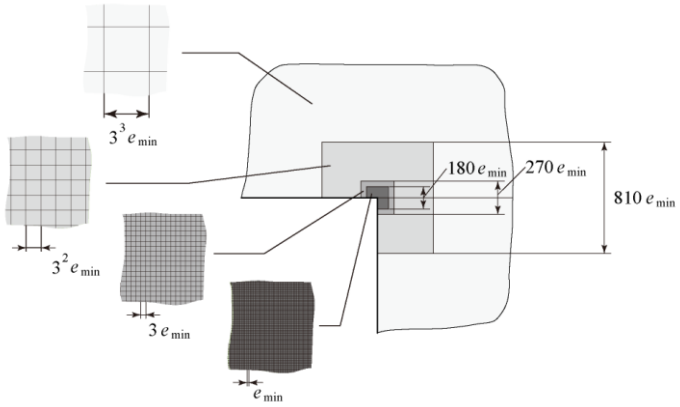

Fig.D.2 Mesh pattern near the interface edge corner

References:

[1] Mintzas A, Nowell D. Validation of an H_{cr}-based fracture initiation criterion for adhesively bonded joints. Eng Fract Mech 2012; 80: 13-27.

[2] Carpenter, W. C. Byers C. A path independent integral for computing stress intensities for V-notched cracks in a bi-material, In J Fract 1987; 35: 245-268.

Appendix E. Analysis method for the deformation angle at interface corner

In Appendix E, the analysis method for the deformation angle at interface corner is presented. The total length of the specimen is 225mm, adhesive length l_{ad} =25mm, adhesive thickness t_{ad} =0.15mm, fixed boundary length L =50mm, adherend length l_2 =90mm, P =14.15N.

Fig. E.1(a) shows the displacements u_y along x direction for t_1 =7mm. It is found that the displacements of adherends are symmetrical. Fig. E.1(b) shows the details of corner edge O in Fig.E.1(a). As can be seen from Fig. E.1(b), an inflexion appears at the corner edge point O ($x_1 = 0$), the distance between the upper interface corner point O and lower interface corner point C' is 0.000078mm. The adhesive thickness t_{ad} =0.15mm, the ratio of the distance and adhesive thickness is 0.000078/0.15=0.052%. Since the values of distance is affected by the peeling force due to the deformation, the distance decreases with decreasing deformation at the interface corner. Therefore, it is feasible to investigate the deformation at the interface corner based on the displacement.

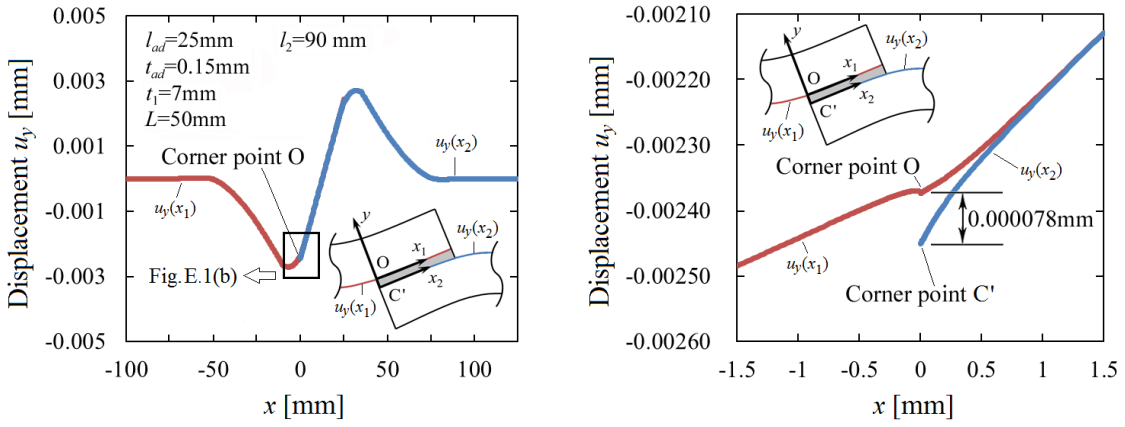

(a) Full figure (b) Details of corner edge O in Fig.E.1(a)

Fig.E.1 Displacement u_y along x direction

Fig. E.2 shows the deformation near the interface corner. In order to obtain the deformation angle, two target points are considered. Here, l_θ means the distance between the two target points. For the deformation angle θ_{ol} at the interface corner O, the two target points are points O and A. For the deformation angle θ_{or} at the interface corner O, the two target points are points O and B. For the deformation angle θ_C at the interface corner C, two target points are points C and D. The equations of deformation angles θ_{ol}, θ_{or} and θ_C are expressed as follows.

$$\theta_{or} = \arctan(\frac{y_B - y_O}{x_B - x_O}),\ \theta_{ol} = \arctan(\frac{y_O - y_A}{x_O - x_A}),\ \theta_C = \arctan(\frac{y_C - y_D}{x_C - x_D}) \quad \text{(E.1)}$$

Here, x_n and $y_n (n = \text{O,A,B,C,D})$ are the coordinates of points O, A, B, C and D.

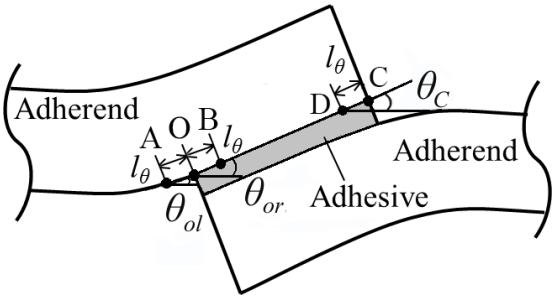

Fig. E.2 Deformation near the interface corner.

Fig. E.3(a) shows the results of deformation angles at corner O with different distances l_θ for t_1=7mm. It is found that the values of θ_{ol} and θ_{or} both increase with increasing l_θ, and the difference between θ_{ol} and θ_{or} increases with decreasing l_θ. Therefore, it is difficult to obtain the maximum deformation angle at interface corner O. Fig.E.3(b) shows the results of deformation angle θ_C with different distances l_θ for t_1=7mm. It is seen that the value of θ_C initially increases and then decreases with increasing l_θ. The maximum θ_C can be obtained when $l_\theta = 1/3^3$mm and the value of maximum θ_C is almost constant independent of element sizes (see Table 6.1).

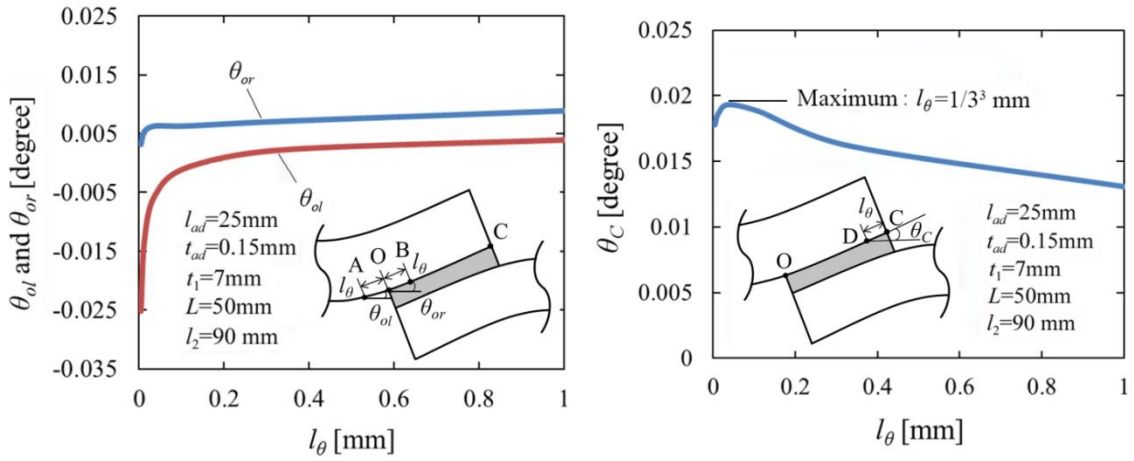

(a) corner O (b) corner C

Fig. E.3 Deformation angle at interface corner edge.

Fig.E.4 shows the relationship between deformation angles θ_{ol}, θ_{or} and θ_C. It is found that the θ_C-θ_{ol} relation and θ_C-θ_{or} relation are almost linear, and the slope of the lines are nearly the same. Therefore, in this study, the deformation angle is considered by using the maximum θ_C at corner C.

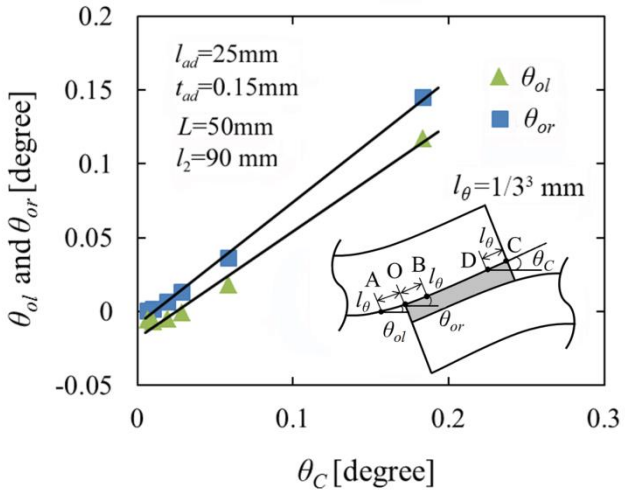

Fig. E.4 Relationship between θ_{ol}, θ_{or} and θ_C